

UNIVERSIDADE DE SANTIAGO DE  
COMPOSTELA

**Tuning the electronic  
properties of transition-metal  
compounds: an *ab initio*  
study**

by

Antía Sánchez Botana

A thesis submitted in partial fulfillment for the  
degree of Doctor of Philosophy

in the

Facultade de Física

Departamento de Física Aplicada

30<sup>th</sup> May, 2013





# Declaration of the Advisors

We, DANIEL BALDOMIR FERNÁNDEZ, professor of the Applied Physics Department at the University of Santiago de Compostela, and VICTOR PARDO CASTRO, doctor of Philosophy in Physics by the University of Santiago de Compostela

DECLARE THAT:

- This thesis entitled '*Tuning the electronic properties of transition-metal compounds: an ab initio study*' and the work presented in it was carried out by ANTÍA SÁNCHEZ BOTANA under our advising.
- The thesis is submitted in partial fulfillment for the degree of Doctor of Philosophy in the Applied Physics Department at the University of Santiago de Compostela.

Signed Prof. Daniel Baldomir Fernández

---

Signed Dr. Victor Pardo Castro

---

Santiago de Compostela, 30<sup>th</sup> May, 2013.



# Declaration of Authorship

I, ANTÍA SÁNCHEZ BOTANA, declare that this Thesis entitled, ‘*Tuning the electronic properties of transition-metal compounds: an ab initio study*’ and the work presented in it are my own. I confirm that:

- This work was done wholly or mainly while in candidature for a research degree at this University.
- Where any part of this Thesis has previously been submitted for a degree or any other qualification at this University or any other institution, this has been clearly stated.
- Where I have consulted the published work of others, this is always clearly attributed.
- Where I have quoted from the work of others, the source is always given. With the exception of such quotations, this Thesis is entirely my own work.
- I have acknowledged all main sources of help.
- Where the Thesis is based on work done by myself jointly with others, I have made clear exactly what was done by others and what I have contributed myself.

Signed:

---

Date: 30<sup>th</sup> May, 2013

---





Salvador Dalí - *Galatea of the spheres*. Oil on canvas, 65 x 54 cm, 1952. Dalí Theater and Museum, Figueres, Spain



UNIVERSIDADE DE SANTIAGO DE COMPOSTELA

# *Abstract*

Facultade de Física  
Departamento de Física Aplicada

Doctor of Philosophy

by Antía Sánchez Botana

This PhD Thesis deals with the analysis using first-principles calculations of transition-metal compounds whose electronic properties reside in the vicinity of a metal-to-insulator transition, the ultimate goal being the computational design of materials with new functionalities based on our calculations and the full understanding of these systems in order to make new predictions.

A large portion of the technological progress over the past decades has been related to Materials Science and Condensed Matter Physics. Particularly, the latter half of the 20th century witnessed an explosion of new materials and new ways to tune their properties. A powerful driving force behind the technology revolution is the ability to control the electronic properties of a material on demand, giving rise to new functionalities. An important class of these novel materials is represented by transition-metal compounds where outstanding properties such as ferroelectricity, colossal magnetoresistance, high temperature superconductivity and metal-insulator transitions can be observed. In addition to this huge heterogeneity of physical phenomena, there is potential for exciting new discoveries in these materials: the enhancement of thermoelectric properties through nanostructuring or the new phenomena on surfaces and interfaces between complex oxides are clear examples of that and have been explored by a lively scientific community in the last years.

Because of the agreement between experimental and computational data, Density Functional Theory (DFT) proves to be a reliable tool to acquire new knowledge in Materials Science, even in the complicated case of strongly correlated electron systems such as transition-metal compounds. For this reason, the methodology to perform the *ab initio* calculations throughout this Thesis will be DFT as it is implemented in the WIEN2k code. The transport properties calculations will be performed using the BoltzTraP code, a semiclassical approach based on the Boltzmann transport theory within the constant scattering time approximation.

First, we will study the changes in electronic structure between the low and high temperature phases of  $V_4O_7$  across its temperature-induced metal-insulator transition. We will analyze charge and magnetic order, the nature of the observed structural distortions, the degree of charge disproportionation in both phases and the nature and strength of the magnetic couplings. We will also analyze the electronic structure, special magnetic properties and thermopower of a quasi-one-dimensional oxide,  $Sr_6Co_5O_{15}$ . The study of this material serves as a confirmation of our ability to make predictions of the thermoelectric properties of a system. After that we will describe the electronic structure and transport properties of bulk CrN using a diverse set of exchange-correlation potentials. The electronic properties of this material, close to a metal-insulator transition, have been a matter of discussion due to the controversial results found experimentally and we propose how to reconcile the different pictures.

After understanding the properties of these bulk materials, we will deepen into several mechanisms of tuning their electronic properties. To elucidate the origin of the experimentally found metallic behavior of the low-temperature phase of CrN, and to analyze what the effects of a material so close to a metal-insulator transition are when it is nanostructured, we have studied free-standing thin films of CrN. This will allow us to predict an unexpected electronic reconstruction at the surface that leads to emergent conducting states confined to a thickness of less than 1 nm. We will also analyze the effects of quantum confining CrN, studying the electronic structure of CrN/MgO multilayers. This will be the best scenario to study the effect of a drastic dimensionality reduction without surface states appearing, that otherwise complicate the study.



The enhancement of the thermoelectric response of  $\text{La}_2\text{NiO}_{4+\delta}$  through hole-doping and strain will be the focus of part of the Thesis. This material, due to its layered structure, would be a suitable candidate for an improvement of its thermoelectric properties by nanostructurization in thin films. Our study provides evidences on how to tune computationally a layered oxide to achieve an enhanced thermoelectric performance, and how this nickelate would be, if optimized, comparable to the best available thermoelectric oxides.

All in all, we will analyze the structural, magnetic, electronic and thermoelectric properties of several transition-metal compounds. We will conclude that *ab initio* techniques not only describe correctly the physical properties of these systems but also allow to manipulate them in order to give rise to new functionalities.





## Acknowledgements

One of the joys of completion is to look over the journey past and remember all the co-workers, friends and family who have helped and supported me along this long but fulfilling road.

My first debt of gratitude must go to my advisor, Prof. Daniel Baldomir. Thanks for convincing me to start walking this road I now take so much pleasure in. I must specially thank Dr. Victor Pardo. You patiently provided the vision, encouragement and advise necessary for me to complete this process. Without your help and invaluable suggestions this work would not have been possible.

To my group mates: Dr. Manuel Pereiro, Dr. Jorge Botana, Dr. David Serantes, Dr. Alberto Piñeiro and Msc. Iván Conde. Thanks for your friendship and for providing a stimulating work environment. You have been my second family during this time, without your support and advice, in science and life, I would have lost the strength to continue the road (many times!).

During this journey I visited scientific groups in the Vienna University of Technology and the U.S Naval Research Laboratory. I should also thank my advisors during these periods, Prof. Peter Blaha and Dr. Michelle Johannes. Thanks for your patience, for being so available

and showing me that scientific and human quality must go together. I cannot forget the people I have collaborated with during this time: Francisco Rivadulla and his group members, Daniel Khomskii, Fabien Tran, Cristina de la Calle, Pablo Botta and Carlos Boubeta. Thanks for your work and for helping me broaden my scientific vision through all the discussions we had during this time.

To my parents and brother, thank you. You always showed me “there was a road I must find, a road that was mine” and that I could not construct it without effort and humility. Definitely, I would not have finished this journey if it was not for you. Laia, thanks for always being the voice of sanity and making me see things in perspective. Lucía and Lorena, who started walking the Physics’ road with me, and have shown to be two of the most special people I have ever met. Thanks for always being there to listen and help me keep walking after the stones I found along the road and, of course, for all the laughs! To all my friends who have shown to be the best: Ana, María, Fany, Sara, Alejandra, Alberto, Patri, Cris... Thanks for always being there willing to sit down and listen to me (even if I had the same problems and complains time after time). My friends in Vienna and DC were sources of laughter and support and made the road easier to follow while I was away from home. Paz, Ramón, Pilar and specially, Alba and Lauren, I could never thank you enough. And finally to those who were there when I started walking this road and are not here now. I hope they somehow feel proud wherever they are...





## Contents

<b>Declaration of the Advisors</b>	<b>iii</b>
<b>Declaration of Authorship</b>	<b>v</b>
<b>Abstract</b>	<b>ix</b>
<b>Acknowledgements</b>	<b>xiii</b>
<b>1 Introduction</b>	<b>1</b>
1.1 Motivation . . . . .	1
1.2 Importance of transition-metal compounds . . . . .	3
1.2.1 New electronic phenomena in transition-metal compounds . . . . .	6
1.3 Thermoelectric materials . . . . .	9
1.3.1 Transition-metal compounds as thermoelectric materials . . . . .	10
1.3.2 General mechanisms to increase the thermoelectric efficiency. Research in Low-Dimensional Systems.	11
1.4 Density Functional Theory (DFT) . . . . .	13
1.4.1 Quantum mechanical description of a solid . . . . .	13
1.4.2 The Born-Oppenheimer approximation . . . . .	14

1.4.3	The Hohenberg-Kohn formulation of density functional theory . . . . .	16
1.4.4	The Kohn-Sham equations . . . . .	17
1.4.5	The exchange-correlation functional . . . . .	20
1.4.5.1	LDA+ $U$ . . . . .	23
1.4.5.2	Modified Becke-Johnson potential . . . . .	25
1.4.6	APW+lo method . . . . .	26
1.4.7	WIEN2k code: computational details . . . . .	28
1.4.8	Definition of the transport coefficients . . . . .	29
1.4.9	Calculation of the transport distribution and coefficients: BoltzTraP code . . . . .	30
1.5	Overview of the Thesis . . . . .	33
<b>2</b>	<b>Electronic structure of <math>V_4O_7</math>: Charge ordering, metal-insulator transition, and magnetism</b>	<b>35</b>
2.1	Introduction . . . . .	35
2.2	Computational details . . . . .	39
2.3	Results . . . . .	40
2.3.1	Structure . . . . .	40
2.3.2	Electronic structure . . . . .	41
2.3.3	Conclusions . . . . .	52
2.4	Summary . . . . .	53
<b>3</b>	<b>Electronic structure of bulk CrN: A comparison between different exchange correlation potentials</b>	<b>55</b>
3.1	Introduction . . . . .	55
3.2	Computational details . . . . .	60
3.2.1	Structure . . . . .	62
3.3	Results . . . . .	62
3.3.1	LDA+ $U$ electronic structure analysis . . . . .	67
3.3.2	TB-mBJLDA electronic structure analysis . . . . .	71
3.3.3	Hybrid functionals electronic structure analysis . . . . .	72
3.4	Discussion . . . . .	74
3.5	Summary and conclusions . . . . .	77
<b>4</b>	<b><math>Sr_6Co_5O_{15}</math>: non-one-dimensional behavior of a charge ordered structurally quasi-one-dimensional oxide</b>	<b>79</b>
4.1	Background . . . . .	79
4.2	Computational details . . . . .	82
4.3	Results . . . . .	83



4.3.1	Structure . . . . .	83
4.3.2	An ionic model . . . . .	83
4.3.3	Electronic structure calculations . . . . .	85
4.3.4	Magnetic properties . . . . .	90
4.3.5	A peculiar quasi-one-dimensional oxide . . . . .	93
4.3.6	Transport properties. . . . .	94
4.4	Summary . . . . .	95
<b>5</b>	<b>Enhanced thermoelectric response of hole-doped <math>\text{La}_2\text{NiO}_{4+\delta}</math> by <i>ab initio</i> calculations</b>	<b>97</b>
5.1	Background . . . . .	97
5.2	Computational Procedures . . . . .	101
5.3	Results . . . . .	102
5.3.1	Basic description of the electronic structure . . . . .	102
5.3.2	Tuning the electronic structure via hole-doping . . . . .	104
5.3.3	VCA calculations . . . . .	108
5.3.4	More realistic estimates . . . . .	113
5.4	Summary . . . . .	114
<b>6</b>	<b>Strain effects to optimize thermoelectric properties of hole-doped <math>\text{La}_2\text{NiO}_{4+\delta}</math> via <i>ab initio</i> calculations</b>	<b>117</b>
6.1	Introduction . . . . .	117
6.2	Computational Procedures . . . . .	118
6.3	Results . . . . .	119
6.3.1	Revisiting the electronic structure and magnetic properties of unstrained $\text{La}_2\text{NiO}_4$ . . . . .	119
6.3.2	Changes in the electronic structure caused by strain	121
6.3.3	Influence of strain on the thermoelectric properties	124
6.4	Summary . . . . .	130
<b>7</b>	<b>Surface electric dipole formation in CrN(001) very thin films</b>	<b>131</b>
7.1	Background . . . . .	131
7.2	Computational details . . . . .	133
7.3	Results . . . . .	133
7.3.1	Unit cell details. . . . .	133
7.3.2	Ionic model. . . . .	134
7.3.3	Evolution with thickness. . . . .	136
7.3.4	10-layer case in detail. . . . .	140

7.3.5	Influence of lattice relaxations: surface dipole formation. . . . .	143
7.4	Summary . . . . .	147
<b>8</b>	<b>Electronic structure of CrN/MgO multilayers</b>	<b>149</b>
8.1	Background . . . . .	149
8.2	Computational procedures . . . . .	150
8.3	Results . . . . .	150
8.4	Summary . . . . .	160
<b>A</b>	<b>List of Publications</b>	<b>161</b>
<b>B</b>	<b>Resumo da presente Tese Doutoral</b>	<b>163</b>
B.1	Estrutura electrónica do $V_4O_7$ : orde de carga, transición metal-illante e magnetismo . . . . .	165
B.2	Estrutura electrónica de CrN masivo: unha comparación entre distintos potenciais de intercambio correlación . . . . .	167
B.3	Formación dun dipolo eléctrico na superficie de películas delgadas de CrN (001) . . . . .	169
B.4	Estrutura electrónica de multicapas de CrN/MgO . . . . .	170
B.5	$Sr_6Co_5O_{15}$ : comportamento nonunidimensional nun óxido cuasiunidimensional con orde de carga . . . . .	171
B.6	Mellora na resposta termoeléctrica de $La_2NiO_{4+\delta}$ mediante dopado con ocos e tensión empregando métodos <i>ab initio</i> . . . . .	172
B.7	Resumo xeral . . . . .	173
<b>C</b>	<b>Summary and conclusions</b>	<b>175</b>
C.1	Electronic structure of $V_4O_7$ : Charge ordering, metal-insulator transition, and magnetism . . . . .	177
C.2	Electronic structure of bulk CrN: A comparison between different exchange correlation potentials . . . . .	179
C.3	Surface electric dipole formation in CrN (001) very thin films . . . . .	181
C.4	Electronic structure of CrN/MgO multilayers . . . . .	182
C.5	$Sr_6Co_5O_{15}$ : non-one-dimensional behavior of a charge ordered structurally quasi-one-dimensional oxide . . . . .	183
C.6	Enhanced thermoelectric response of $La_2NiO_{4+\delta}$ through hole doping and strain by <i>ab initio</i> calculations . . . . .	184

---

C.7 Conclusions . . . . .	185
<b>Bibliography</b>	<b>187</b>





“

*The modern age has a false sense of security because of the great mass of data at its disposal. But the valid issue is the extent to which man knows how to form and master the material at his command.*

*[Johann Wolfgang von Goethe]*

”

## 1.1 Motivation

A large portion of the technological progress over the past decades has been related to Materials Science and Condensed Matter Physics. Particularly, the latter half of the 20th century witnessed an explosion of new materials and of new ways to tune their properties but the importance of Materials Science is nothing new. The choice of a material of a given era often defines it: the Stone Age, Bronze Age, and Steel Age are evident examples. A powerful driving force behind the technology revolution we have seen in the last decades is the ability to control on demand the electronic properties of a material. The best example are

semiconducting field-effect transistors whose ability to conduct an electrical current can be controlled by applying an electric field. Several hundred millions of these devices are needed to run tools that are indispensable in our daily live including cars, computers, and cell phones [1].

All the electronic properties in solids arise from the equation Schrödinger proposed in his groundbreaking paper in 1926 that marked the birth of Quantum Mechanics [2]. It describes the behavior of an electron under the influence of an electromagnetic potential. After its successful application to small simple systems, such as the He atom and the H<sub>2</sub> molecule, Dirac declared that chemistry had come to an end since all systems could be described by this powerful equation. However, it soon turned out that, although Schrödinger's equation correctly described also many-electron systems, it could not be solved exactly in realistic problems.

In the following more than six decades, huge efforts have been made in order to find approximate solutions of Schrödinger's equation for systems with several electrons, aided by modern computers. So-called *ab initio* methods calculate, applying certain approximations, the physical properties of many-electron systems starting from the Schrödinger equation without any adjustable parameters. Such a method is Density Functional Theory (DFT) that was reported in the 1960s in two publications [3, 4]. It addresses the many-electron problem using the electron density (a scalar quantity in the real, 3-dimensional coordinate space) instead of the wave-function (a vector of an N-dimensional Hilbert space) as central quantity. Since it is much less computationally demanding than wave function methods and due to its accuracy it rapidly became a standard method in computational Solid State Physics. The Nobel Prize in Chemistry awarded to Walter Kohn and John Pople in 1998 acknowledges the importance of the method [5].

Because of the agreement between experimental and computational data, DFT proves to be a reliable tool to acquire new knowledge in Materials Science, even in the complicated case of strongly correlated

electron systems such as transition-metal compounds. These represent an important class of novel materials where outstanding electronic properties such as ferroelectricity [6], superconductivity [7], and colossal magnetoresistance [8] are observed. Some of them have also recently shown good prospects as thermoelectric materials [9]. This richness of phenomena and the possibility to further tune their properties thanks to recent advances in Materials Science, specially in nanotechnologies, has been motivating many researchers to study transition-metal compounds in great detail.

The goal of this Thesis is to study the structural, electronic, magnetic and thermoelectric properties of transition-metal compounds using DFT-based calculations. The ultimate goal will be the computational design of materials with new functionalities based on our calculations and our understanding of these systems. We will try to explore new paths to further optimize the electronic properties of some of them through nanostructuring and dimensionality reduction. All the materials studied throughout this Thesis are chemically and structurally different but show some similar properties being close to a transition from a localized to itinerant behavior. As we will see in the next Section, these are features typical of  $3d$  electron systems, which are the main ones we have studied here. The flexibility of  $3d$  electrons to behave both as localized or itinerant depending on the system they are in makes them more difficult to study but also more interesting in terms of new phenomenology.

## 1.2 Importance of transition-metal compounds

The study of transition-metal compounds has attracted the interest of the scientific community during the last 50 years. Since the beginning of the fifties, scientists tried to understand the properties of these materials that have been shown to be far from trivial due to the

interplay between structural, magnetic and electronic degrees of freedom. This gives rise to a broad range of interesting phenomena, such as high- $T_C$  superconductivity, colossal magnetoresistance, large Seebeck coefficient, charge-orbital order, Mott insulators, metal-insulator transitions (MIT), heavy fermions, etc. All these different properties make them probably the most interesting class of materials in nature, providing new opportunities for basic science and innovative device applications. The heterogeneity of physical phenomena in strongly correlated materials such as transition-metal compounds is mainly caused by the existence of partially filled  $d$  or  $f$  electron shells. The versatility of  $d$  or  $f$  electrons, that can behave either as localized or as itinerant particles, is certainly at the origin of all these interesting properties.

Though a crossover region exists, one can say that metallic phases in transition-metal compounds are generally on the itinerant-electron limit, while insulating ones are on the localized one. The transition from an insulator to a metal, driven by tunable parameters, is called metal-to-insulator transition or localized-to-itinerant in Goodenough terms [10]. The first successful theoretical description of metals, insulators and transitions between them is based on non interacting or weakly interacting electron systems. The general distinction between metals and insulators at zero temperature is based on the filling of the electronic bands: an insulator is a material in which all bands are either full or empty while in a metal one or more bands are only partially full. In other words, the Fermi level lies in a band gap in insulators and inside a band for metals. This was stated in the early years of Quantum Mechanics (1928-1929) by Bethe, Bloch and Sommerfeld. In the non-interacting electron theory, the formation of a band structure is totally due to the periodic lattice structure of atoms in crystals. By the early 1930s, it was recognized that insulators with a small energy gap would be semiconductors due to thermal excitation of the electrons.

Although this band picture was successful in many aspects, experimental reports observed that different transition-metal compounds



with a partially filled  $d$ -electron band were nonetheless poor conductors and indeed often insulators. It was Peierls who pointed out the importance of the electron-electron correlation indicating that strong Coulomb repulsion between electrons could be the origin of this insulating behavior. His observations launched the long and continuing history of the field of strongly correlated electrons, where a particular effort is made to understand how partially filled bands can result in insulators. Among the theoretical approaches, Mott (1949) took the first important step towards understanding how electron-electron correlations could explain the insulating state, later called a Mott insulator.

In a general way, we can say that the  $d$  electrons in transition-metal ions experience two competing forces: Coulombic repulsion that tends to localize individual electrons at atomic lattice sites, while hybridization with the anion- $p$  electron states tends to delocalize the electrons. The subtle balance is the one that makes many of the transition-metal compounds excellent resources for studying the MIT that can accompany dramatic changes in the electronic properties of a system [11].

The transition from a localized to an itinerant electron picture has been thoroughly studied in the last decades and observed in transition-metal compounds induced by pressure [12], chemical pressure [13, 14], structural changes [15], temperature [16], spatial confinement [17], or a simple change in electron count [18]. Charge ordering plays an important role in the insulating side of these MIT in various transition-metal compounds, happening both in bulk compounds such as perovskite manganites [19], and in nanostructures [20]. When materials approach a MIT, the lattice can become softer due to bond-length fluctuations [21], and this could lead to structural distortions or phase transitions of peculiar character [22, 23]. We will study along this Thesis several systems that show a MIT or are close to one:  $V_4O_7$ , CrN, and  $La_2NiO_4$ .

To discuss localization effects in a general way, it is helpful to mimic the physics of the Hubbard model [24–26] and define two terms, with a picture of periodic ions containing atomic-like orbitals in mind. The first term, called  $t$ , which describes the tendency of an electron to

hop from one atom site to another. This tendency is governed by the overlap of orbitals located on the two sites in question. One can often say that the bandwidth ( $W$ ) is related directly to  $t$ , in the form of the simplest band in one dimension:  $\epsilon_k = t\cos(k_a)$ , hence  $W = 2t$  (the smaller the hopping, the smaller  $W$  and the more localized the electrons are). The second term, named  $U$ , is the repulsion energy (Coulomb energy) between two electrons which occupy orbitals on the same ion. If  $t$  is large compared to  $U$ , there is little price to be paid for double occupancy of a single site and electrons hop from site to site continuously and cannot be said to be localized. In systems where  $t$  is large, bands will disperse strongly and the density of states will be broad. In the opposite limit, when  $U$  is much larger than  $t$  the price of double occupancy is large. Electrons prefer to stay on a single ion, rather than hop to the neighboring one which already contains an electron. Hence, a model of non-interacting electrons no longer makes sense. The extent to which a system is localized can be gauged by the ratio  $U/t$ . These so-called correlation effects go beyond the one-electron band picture that we use in DFT calculations. However, we will see in Section 1.4.5 the methods that should be used in DFT to treat strongly correlated systems in the localized-electron limit. These methods will allow us to predict the correct insulating ground-state of the transition-metal compounds we have studied, not underestimating the electron correlation/localization effects.

### 1.2.1 New electronic phenomena in transition-metal compounds

Recent advances in Materials Science allowed the exciting opportunity of designing materials with nanometer-scale features. Some materials that even in their bulk exhibit functional properties (such as those mentioned above for transition-metal compounds) can be further optimized by studying them in the nanoscale. This type of research has opened broad perspectives for both basic science and technology.

The manipulation of the electronic structure of a material via quantum confinement and dimensionality reduction has been shown to lead to many other electronic-structure-related properties different from the ones of their three dimensional (3D) precursors. An exciting opportunity that has focused much attention is to study interfaces and surfaces of transition-metal compounds. At the surface of a crystalline solid the symmetry of the ordered bulk phase is broken. This reduced symmetry allows for new phenomena to be observed, with the effects of shapes and boundaries becoming crucial. In addition, a lot of materials exhibiting a huge diversity of electronic properties, possess a similar crystalline structure. This creates the opportunity to combine them in heterostructures that have been shown to lead to new electronic properties unanticipated by the ones of the bulk constituents. The oxide heterostructure formed by  $\text{LaAlO}_3/\text{SrTiO}_3$  is the prime example, since the interface between these two non-magnetic insulating oxides is observed to be conducting [27], ferromagnetic (FM) [28], and even superconducting [29]. All these properties are believed to occur in a very thin layer around the interface where peculiar two dimensional (2D) electronic states reside. In addition, surface effects such as those caused by vacancies produced mechanically have been shown to yield a 2D electron gas confined to a nanometric surface layer in  $\text{SrTiO}_3$  [30]. The unexpected metallic behavior in  $\text{LaAlO}_3/\text{SrTiO}_3$  is mainly attributed to the electronic reconstruction at the interface [31]. In the heterostructure formed by  $\text{LaTiO}_3/\text{SrTiO}_3$  (both materials are also insulating in the bulk) the interface shows metallic behavior. In this case, metallicity is attributed largely to epitaxial strain-induced electronic structure modifications and secondarily to electronic reconstruction at the interface [32]. Another interface that exhibits metallic behavior with its bulk counterparts being insulating is the one formed by  $\text{LaVO}_3/\text{SrTiO}_3$  with the observed metallic behavior primarily attributed to interface effects [32]. It has also been shown that geometrically confined  $\text{LaVO}_3/\text{SrVO}_3$  favors a ferromagnetic order at room temperature due to the 2D character of the doping planes that leads

to a reduction in the width of the bands crossing the Fermi level, even though none of the constituents are ferromagnetic in the bulk, nor are their solid solutions [33, 34]. A similar example of this, more related to the epitaxial strain, occurs in  $\text{LaCoO}_3$ , where thin films grown on  $\text{SrTiO}_3$  turn out FM as opposed to the diamagnetism shown by the bulk material [35–37].

Also heterostructures with nonpolar interfaces can give rise to unanticipated behavior of their bulk constituents. One clear example is the  $d^0/d^1$  interface in multilayer  $\text{VO}_2/\text{TiO}_2$  nanostructures that show a semi-Dirac point Fermi surface [38]. The behavior is an electron confinement phenomenon assisted by orbital ordering and these nanostructures exhibit a metal-insulator transition as the thickness of the  $d^1$  oxide is decreased [39]. Another example of  $d^0/d^1$  nanostructure displaying interesting properties are multilayers of  $\text{SrVO}_3$  and  $\text{SrTiO}_3$ . They have been shown to display a transition from the typical insulating behavior of  $\text{SrTiO}_3$  to the metallic behavior of bulk  $\text{SrVO}_3$  as the number of layers of each constituent is increased [17, 40, 41].

In all cases, surface/interface reconstructions lead to new electronic phenomena where all the electronic, spin and orbital degrees of freedom become active and interact differently than in the case of the bulk. This is not completely new, similar surface reconstructions occur in polar surfaces of standard  $sp$  semiconductors like GaAs. However,  $d$  electrons allow for new types of ordering phenomena to occur, where correlation effects can play a major role. The interest in exploring the properties of these artificial materials and the importance of the novel electronic properties found at their interfaces and surfaces is increasing rapidly. These studies are fueling the growth of the semiconductors industry, as demonstrated by the recent integration of high-permittivity oxides in commercial transistors. For this reason we have applied some of these strategies to materials we also studied as bulk. In this context, we will investigate CrN free-standing thin films to analyze the effects of nanostructuring a material so close to a metal-insulator transition. We will also analyze the effects of quantum confining CrN, studying the

electronic structure of CrN/MgO multilayers as well as the effects of strain on the thermoelectric properties of  $\text{La}_2\text{NiO}_{4+\delta}$  and the interface between two band insulators: MgO and  $\text{Al}_2\text{O}_3$ .

### 1.3 Thermoelectric materials

The world's demand for energy and the alarm due to the environmental impact of global climate change due to the combustion of fossil fuels, has led to the need of looking for alternative energy technologies. Thermoelectric materials became good candidates due to their ability to generate usable electricity from wasted heat. However, thermoelectrics have long been too inefficient to be cost-effective in most applications. A resurgence of interest in these materials began in the mid 1990s when theoretical predictions suggested that thermoelectric efficiency could be greatly enhanced through nanostructural engineering, which led to experimental and theoretical efforts to look for highly efficient thermoelectric materials [9].

The efficiency of a thermoelectric device is quantified by the so-called dimensionless thermoelectric figure of merit  $zT = (S^2\sigma/\kappa)T$ , where  $T$  is the absolute temperature,  $S$  is the Seebeck coefficient also called thermopower or thermoelectric power,  $\sigma$  is the electrical conductivity, and  $\kappa$  is the total thermal conductivity of the material which is the sum of the electronic and phononic (lattice) contributions  $\kappa = \kappa_{el} + \kappa_{ph}$ . Good thermoelectric materials should present a  $zT > 1$ . Hence, in order to look for a good thermoelectric performance, it is necessary to design materials that are good electrical conductors, with low thermal conductivity and high Seebeck coefficient (so-called electron crystal - phonon glass behavior). Simultaneous optimization of the three parameters involved in the figure of merit is conflicting because all of them are interrelated through the carrier concentration: the high carrier concentration and large electrical conductivity characteristic of metals enhances  $zT$ , but their low thermoelectric power and high thermal conductivity reduce  $zT$  considerably. On the other

hand, insulators have a large Seebeck coefficient as well as low thermal conductivity but their electrical conductivity is also low, reducing the overall  $zT$ . The best values for the thermoelectric figure of merit are found in doped semiconductors where the carrier concentration can be easily tuned and the phononic part of the thermal conductivity can be reduced without significantly affecting the electrical conductivity simultaneously. Several materials with high values of  $zT$  have been found but they are not suitable for industrial applications since they are generally toxic and can easily decompose at high temperatures. Therefore, obtaining highly efficient, inexpensive, non-toxic and chemically and thermally robust materials for thermoelectric applications still remains a challenge that relies on the extent of achieving the electron crystal - phonon glass characteristics.

### 1.3.1 Transition-metal compounds as thermoelectric materials

In recent years, increasing attention has been given to transition-metal compounds as thermoelectric materials. This interest was mainly motivated by the observation of unexpected high electrical conductivity and large thermoelectric power in the misfit layered cobaltate  $\text{Na}_x\text{Co}_2\text{O}_4$  ( $125 \mu\text{V}/\text{K}$  at 300 K) [42]. Since this discovery, a number of cobaltates with similar layered structure, such as  $\text{Ca}_3\text{Co}_4\text{O}_9$  or  $\text{Bi}_2\text{Sr}_2\text{Co}_2\text{O}_9$ , have been studied due to their potential use as thermoelectric materials. Their characteristic complex-layered structure is believed to be a key piece of the good thermoelectric properties of these materials: the  $\text{CoO}_2$  sheets form conductive layers that could provide the electron-crystal behavior while the blocks in the off-plane direction act like insulating layers which would provide the phonon-glass behavior.

Using first principles calculations, Singh *et al.* [43] pointed out that the large  $S$  in these materials could be explained by standard band theory, observing that the Fermi energy is situated near the top of a

narrow manifold of Co- $t_{2g}$  bands. According to the Mahan-Sofa theory [44], such situation may yield a large Seebeck coefficient even for high carrier densities, which is in agreement with experimental observations in misfit layered cobaltates. The Mahan and Sofa theory has been a guide in the look for materials with an enhanced thermoelectric response although it has recently been shown by Zhou *et al.* [45] that the optimal  $zT$  cannot be found in an extremely narrow conduction band. The existence of an optimal bandwidth for a maximal  $zT$  depends strongly on the scattering models and the dimensionality of the material.

In any case, the mechanisms that govern the unconventional thermoelectric behavior of the different families of strongly correlated electron systems may involve a number of different sources such as spin and orbital degrees of freedom, spin and charge frustrations, charge density waves, or sharp peaks in the density of states. This variety of unusual and remarkable types of behavior and, again, the possibility of tuning their properties by means of several mechanisms, provides strong motivation for further research on the thermoelectric properties of this interesting class of materials.

### 1.3.2 General mechanisms to increase the thermoelectric efficiency. Research in Low-Dimensional Systems.

A common strategy to increase the thermoelectric efficiency is to reduce the thermal conductivity. A reduced thermal conductivity directly improves the thermoelectric efficiency, measured by the dimensionless figure of merit,  $zT$  (let us recall  $zT = (S^2\sigma/\kappa)T$ ) also allowing an additional enhancement of the figure of merit. Three are the main strategies to do so. i) The first is to alloy or create point defects such as interstitials or vacancies in order to scatter phonons within the unit cell. ii) The second strategy is to use complex crystal structures to separate the electron-crystal from the phonon-glass achieving the phonon glass

without harming the electronic properties. iii) A third strategy is to scatter phonons at interfaces by nanostructuring. This restricts the phonon dynamics without hindering the electron motion reducing  $\kappa_{ph}$  without decreasing  $\sigma$  significantly. We will focus on this last strategy.

As we saw in the previous Section, recent progress in nanotechnologies has allowed the design of materials with nanometer-scale features that offer broad perspectives for basic science and technology. The application of these advances in the field of thermoelectric research has led to the development of low-dimensional systems with an enhanced thermoelectric response [46]. The mechanisms that increase  $zT$  through a reduction of dimensionality involve several sources: Firstly, a reduction of the lattice thermal conductivity without a substantial loss in the electronic properties can be achieved by using phonon-inhibiting structures such as thin films. We will propose this mechanism as a possible way to enhance the thermoelectric properties of  $\text{La}_2\text{NiO}_4$  in Chapters 5 and 6. In materials whose thermal conductivity is dominated by heat conduction through phonons, it is possible to lower the thermal conductivity without too high loss in the electronic mobility just by reducing the dimensionality of the system. This happens because the characteristic phonon mean free path (which has a typical value of about hundreds of nanometers) is limited by the dimensionality of the system (on the order of the thickness of a thin film or the size of a nanoparticle in a nanocomposite) while the electron mean free path (about 10 nm) is less so. This means that it is possible to restrict the movement of phonons without hindering the electron motion, reducing  $\kappa_{ph}$  significantly without decreasing too much the Seebeck coefficient and the electronic conductivity, allowing to scatter phonons more effectively than electrons. The second approach is based on the quantum-confinement phenomena that occur in low-dimensional structures. We will try to address the effects on the thermoelectric properties of CrN through this type of mechanism in Chapter 8, studying CrN/MgO multilayers. When the dimensionality of the system decreases from 3D to



nanometer length scales, there is a great variation in the energy dependence of the density of states. Since the density of states becomes sharper for low-dimensional structures, it makes possible to enhance the Seebeck coefficient by increasing the electron density of states at the Fermi level. This approach, which is based on the already mentioned Mahan-Sofa theory, was theoretically predicted in 1993 by Hick and Dresselhaus for quantum wells and quantum wires [47].

## 1.4 Density Functional Theory (DFT)

### 1.4.1 Quantum mechanical description of a solid

As explained in the beginning of this Chapter, at the heart of the *ab initio* techniques lies the intention of solving Schrödinger's equation. One single equation suffices to describe accurately arbitrary systems. As simple as it seems, when applied to the many-body problem, the analytical solution is too unpractical to be searched for. Hence, the need for looking for approximations arises.

Just shortly after Schrödinger's equation was published, the first rudimentary predecessor of DFT was developed by Thomas and Fermi [48]. The model tries to study a multielectronic system based on the Fermi-Dirac statistics, assuming it behaves as a homogeneous electron gas. The model considers interacting electrons moving in an external potential and provides a highly over-simplified one-to-one relation between this potential and the electron density. The theory was quite useful for describing some qualitative trends (total energy of atoms) but it showed major drawbacks for questions of Materials Science (it did not predict the chemical bond).

One of the most successful attempts for dealing with many-electron systems was the Hartree-Fock hypothesis, developed in 1930 by Hartree, Fock and Slater [49, 50]. Within this approximation, a multielectron wave function  $\Psi_{HF}$  can be calculated as an antisymmetric combination

(the so-called Slater determinant) of the wavefunctions  $\psi_i$  of the  $N$  electrons, called spin-orbitals, composing it, including the Pauli exclusion principle.

$$\Psi_{HF} = \frac{1}{\sqrt{N!}} \det[\psi_1 \psi_2 \cdots \psi_N] \quad (1.1)$$

The Hartree-Fock theory is only approximate by definition, since a particular shape of the all-electron wave function is assumed and, hence, in cases where a big accuracy is needed or when the electron-electron interactions are strong, it is inferior to other methods. It is, however, still widely used at present, even for periodic systems.

Over the past few decades, DFT [51] has been the most successful, widely used method in Computational Condensed Matter Physics. The main idea of DFT is to describe a many-body interacting system via its particle density and not via its many-body wavefunction. It reduces the  $3N$  degrees of freedom of the  $N$ -body system to only three spatial coordinates through its particle density. It is based on the Hohenberg-Kohn theorems [52]. These basically state that the properties of the ground-state of a many-electron system are determined uniquely by the electron density (first theorem) and that this quantity can be calculated by a variational principle (second theorem). The ground-state energy is, hence, a functional of the density and, together with the energy, all the physical properties of the system are also a functional of the density. This simplifies enormously the problem of a many-electron system. The idea of Hohenberg and Kohn became operative with the so-called Kohn-Sham equations that describe a method to actually calculate the electron density in multi-electronic systems [4].

### 1.4.2 The Born-Oppenheimer approximation

A material consists of atomic nuclei and electrons. Its (non relativistic) quantum mechanical description is given by a Hamiltonian that

includes the energy terms of all of them. Both, the nuclei and electrons, move, having a kinetic energy. Furthermore, due to their positive charge, there is a repulsive Coulomb interaction between the nuclei. There is also a repulsive Coulomb interaction between the electrons due to their negative charge and between the nuclei and the electrons there is an attractive Coulomb interaction. The exact many-particle Hamiltonian for this system is:

$$\begin{aligned} \hat{H} = & -\frac{\hbar^2}{2} \sum_I \frac{\nabla_{\vec{R}_I}^2}{M_I} - \frac{\hbar^2}{2} \sum_i \frac{\nabla_{\vec{r}_i}^2}{m_e} - \frac{1}{4\pi\epsilon_0} \sum_{I,i} \frac{e^2 Z_i}{|\vec{R}_I - \vec{r}_i|} \\ & + \frac{1}{8\pi\epsilon_0} \sum_{i \neq j} \frac{e^2}{|\vec{r}_i - \vec{r}_j|} + \frac{1}{8\pi\epsilon_0} \sum_{I \neq J} \frac{e^2 Z_I Z_J}{|\vec{R}_I - \vec{R}_J|} \end{aligned} \quad (1.2)$$

where the indices I, J run on nuclei, i and j on electrons, the mass of the nucleus at  $\vec{R}_I$  is  $M_I$ , the electrons have mass  $m_e$  and are located at  $\vec{r}_i$ . The first term is the kinetic energy operator for the nuclei, the second for the electrons. The last three terms describe the Coulomb interaction between electrons and nuclei, between electrons and other electrons, and between nuclei and other nuclei, respectively. Solving this problem exactly is out of the question. For a solid, the number of nuclei has the order of magnitude of  $10^{23}$ . As a consequence, the solution of Schrödinger's equation in real systems encounters an exponential wall. Not only CPU power limits the capacity to perform such a calculation but also just storing the wave function is an impossible task (it can neither be calculated nor stored with sufficient accuracy).

Because of the atomic nuclei being much larger and with much lower velocities than the electrons, we can consider their dynamics to be decoupled, approximating the nuclei to be static. This is the so-called Born-Oppenheimer approximation (1927) that has consequences in the Hamiltonian of a many-particle system. The nuclei do not move anymore, so their kinetic energy is zero and the first term in Eq. 1.2 vanishes, the last one being reduced to a constant. We are left with the

kinetic energy of the electrons, the potential energy due to electron-electron interactions, and the potential energy of the electrons in the (now external) potential of the nuclei. Hence, we can rewrite equation 1.2 as:

$$\hat{H} = \hat{T} + \hat{V} + \hat{V}_{ext} \quad (1.3)$$

With the motion of electrons and nuclei decoupled, we only need to solve Schrödinger's equation for a system of  $N$  electrons under a potential  $V_{ext}$  that contains system-specific information. DFT methods start from the Born-Oppenheimer approximation.

### 1.4.3 The Hohenberg-Kohn formulation of density functional theory

The quantum many-body problem obtained using the Born-Oppenheimer approximation is much simpler than the original, but still far too difficult to solve. Several methods exist to reduce this equation to an approximate but tractable form. As we have mentioned above, a historically very important one is the Hartree-Fock method. It performs very well for atoms and molecules, and is therefore used a lot in Quantum Chemistry. However, for solids it is less accurate. Let us remember here the Thomas-Fermi model that considered interacting electrons moving in an external potential and provided an over-simplified one-to-one implicit relation between this potential and the electron density. However, it is still a model, that could not even predict the existence of the chemical bond.

But, would it be possible to adopt this approach and use it to solve Schrödinger's equation? Is a complete, exact description of the ground-state electronic structure in terms of the electron density possible?

The hypothesis that a knowledge of the ground-state electron density for any electronic system uniquely determines the properties of the system became the starting point of DFT as was formally established in 1964 with two theorems due to Hohenberg and Kohn (HK) [3].

**First theorem: The density as the basic variable:** *The ground-state electron density  $\rho(\vec{r})$  of a bound system of interacting electrons in an external potential  $V_{ext}$  determines this potential uniquely.*

**Second theorem: The Hohenberg-Kohn variational principle:** *For a trial electronic density  $\tilde{\rho}(\mathbf{r})$  such that  $\tilde{\rho}(\mathbf{r}) \geq 0$  and  $\int \tilde{\rho}(\mathbf{r}) d\mathbf{r} = N$*

$$E_0 = \min_{\tilde{\rho}} E_v[\tilde{\rho}] \quad (1.4)$$

where  $E_v[\tilde{\rho}]$  is

$$E_v[\tilde{\rho}] = T[\rho] + V_{ne}[\rho] + V_{ee}[\rho] = \int \rho(\mathbf{r}) v(\mathbf{r}) d\mathbf{r} + F_{HK}[\rho] \quad (1.5)$$

where

$$F_{HK}[\rho] = T[\rho] + V_{ee}[\rho] \quad (1.6)$$

being  $V_{ee}$  = classical repulsion between electrons + nonclassical term.

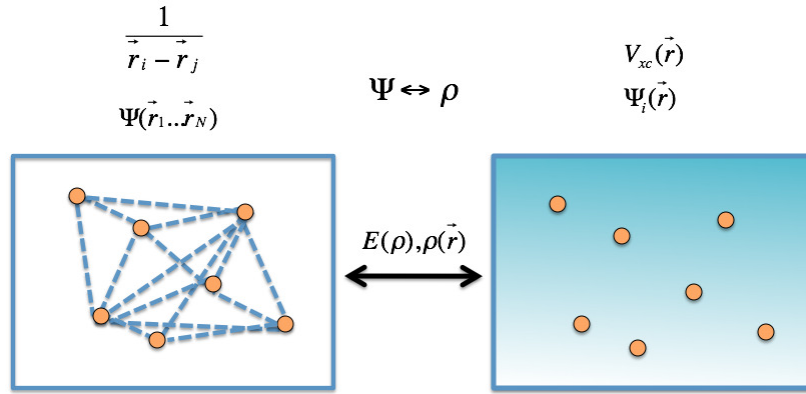
$E_v[\rho]$  reaches its minimal value (equal to the ground-state total energy) for the ground-state density corresponding to  $v$ .

With these two theorems, we can move on from the initial interacting many-body problem into a fictitious non-interacting system, where each electron is subjected only to an effective potential and considered separately but restricted to share the electronic density with the many-body problem as can be seen in Fig. 1.1. We are solving the problem by using a functional that depends solely on the electron density which is where the name Density Functional Theory (DFT) comes from.

The implications of these theorems are that the ground-state properties are dependent only on the electron density and also that a variational principle would give the electron density of the problem, and hence all the ground-state properties.

#### 1.4.4 The Kohn-Sham equations

The starting point for the Kohn-Sham (KS) equations are the Hartree equations: a set of self-consistent single particle equations that allow the approximate description of the electronic structure of atoms where

**Figure 1.1:**

Schematic representation of how, within DFT, the initial interacting many-body problem changes into a non-interacting system, where each electron is subjected to an effective potential but restricted to share the electronic density with the many-body problem

every electron is regarded as moving in an effective single particle potential. The Hartree differential equation had the form of Schrödinger's equation for non interacting electrons moving under a external potential. Could it be possible to extract a Hartree-like formulation from the HK variational principle for the energy? In 1965, Kohn and Sham [4] set themselves to this task.

With the Kohn-Sham equations the original many-body system is replaced by an auxiliary independent-particle system, such that the two systems have exactly the same ground-state density. It maps the original interacting system with the real potential into a fictitious non-interacting system whereby the electrons move within an effective Kohn-Sham single-particle potential  $V_{KS}(\vec{r})$ . For the auxiliary independent-particle system, the auxiliary Hamiltonian is:

$$\hat{H}_{KS} = -\frac{1}{2}\nabla^2 + V_{KS}(\vec{r}) \quad (1.7)$$

For a system with N independent electrons, the ground-state is obtained by solving N one-electron Schrödinger's equations of the form,

$$\left(-\frac{1}{2}\nabla^2 + V_{KS}(\vec{r})\right)\psi_i(\vec{r}) = \epsilon_i\psi_i(\vec{r}) \quad (1.8)$$

where there is one electron in each of the  $N$  orbitals  $\psi_i(\vec{r})$  with the lowest eigenvalues  $\epsilon_i$ . These are called Kohn-Sham equations. The density of the auxiliary system is constructed from:

$$\rho(\vec{r}) = \sum_{i=1}^N |\psi_i(\vec{r})|^2 \quad (1.9)$$

which is subject to the conservation condition:  $\int \rho(\vec{r})d\vec{r} = N$ . The non-interacting independent-particle kinetic energy  $T_S[\rho(\vec{r})]$  is given by,

$$T_S[\rho(\vec{r})] = -\frac{1}{2} \sum_{i=1}^N \int \psi_i^*(\vec{r})\nabla^2\psi_i(\vec{r})d\vec{r} \quad (1.10)$$

which is actually expressed in terms of the one-electron orbitals and not directly as a function of the density.

The ground-state energy of the system with the external potential  $v(\vec{r})$  can be expressed by the following energy functional:

$$E[\rho] = T[\rho] + \int \rho(\vec{r})v(\vec{r})d\vec{r} + V_{ee}[\rho] \quad (1.11)$$

$T[\rho]$  is the kinetic energy and  $V_{ee}$  represents all the electron-electron interaction energy. For a non-interacting system,  $V_{ee} = 0$ .

In DFT, the Kohn-Sham equation is the Schrödinger equation of a fictitious system (the ‘‘Kohn-Sham system’’) of non-interacting particles that generates the same density as any given system of interacting particles. The Kohn-Sham equation is defined by a local effective (fictitious) external potential  $V_{KS}(\vec{r})$ , in which the non-interacting particles move. In order to find a more explicit representation of the Kohn-Sham potential, the energy functional is rewritten as:

$$E[\rho] = T_{KS}[\rho] + \int \rho(\vec{r})v(\rho)d\vec{r} + J[\rho] + E_{xc}[\rho] \quad (1.12)$$

where  $J[\rho]$  is the electronic Coulomb energy,

$$J(\rho) = \frac{1}{2} \int \int \frac{\rho(\vec{r}_1)\rho(\vec{r}_2)}{|\vec{r}_1 - \vec{r}_2|} d\vec{r}_1 d\vec{r}_2 \quad (1.13)$$

and the new introduced exchange-correlation energy functional ( $E_{xc}[\rho]$ ) in equation 1.12 is defined as:

$$E_{xc}[\rho] \equiv T(\rho) - T_{KS}(\rho) + V_{ee} - J(\rho) \quad (1.14)$$

This quantity collects all the non-classical interactions between the electrons and the difference of the kinetic energies of the interacting and non-interacting N electron system. Thus, the accuracy of DFT is mainly determined by the quality of the approximation used for the calculation of  $E_{xc}[\rho]$ . This is the major problem within DFT because the exact functionals for the exchange and correlation are not known except for the homogeneous free electron gas. However, good approximations have been implemented during the last 30 years, and new ones continue to appear as we will see and test throughout this Thesis.

#### 1.4.5 The exchange-correlation functional

So far, DFT has been presented as a formal mathematical framework for viewing the electronic structure from the perspective of the electron density. However, its implementation requires approximations for the energy functional in the HK formulation and for the so-called exchange-correlation functional, that accounts for the “quantum” effects of the electron-electron interactions within the system, in the KS formulation. These approximations reflect the physics of the electronic structure and come from outside DFT. Focusing on the exchange-correlation functional, several approximations exist for calculating these effects. One of the first developed approximations and the simplest one was the local-density approximation (LDA) [4], where the functional depends solely upon the value of the electron density at each point in space

$$E_{xc}^{LDA}[\rho] = \int \epsilon_{xc}(\rho)\rho(\vec{r})d\vec{r} \quad (1.15)$$



where  $\epsilon_{xc}(\rho)$  is the exchange-correlation energy density. The LDA, obviously exact for a uniform electron gas, has been found to give extremely useful results for most applications, being particularly accurate for solids. Experience has shown that the LDA gives ionization energies of atoms, dissociation energies of molecules and cohesive energies with a fair accuracy of typically 10-20 % error. However, it gives bond-lengths and thus geometries of molecules and solids with an accuracy close to a 1 % error. In the LDA the exchange-correlation energy due to a particular density  $\rho(\vec{r})$  can be found by dividing the material in infinitesimally small volumes filled with a homogeneous electron gas, that has the same overall density as the original material has in this volume.

A next logical step to improve on the LDA, is to make the exchange-correlation contribution of every infinitesimal volume not only dependent on the local density in that volume, but also on the density in the neighboring volumes. It means that the gradient of the density will play a role. This new approximation is the generalized gradient approximation (GGA) [53].

$$E_{xc}^{GGA}[\rho] = \int \epsilon_{xc}^{GGA}(\rho, \nabla\rho)\rho(\vec{r})d\vec{r} \quad (1.16)$$

which introduces the density gradients  $\nabla\rho(\vec{r})$  as additional local arguments of the exchange-correlation energy density.

Although GGA performs in general slightly better than LDA, there are a few drawbacks. There is only one LDA exchange-correlation functional, because there is a unique definition for  $\epsilon_{xc}$ . But some freedom exists in how to incorporate the density gradient, and therefore many versions of GGA exist (and also the so-called meta-GGA functionals). Common GGA functionals are Perdew-Wang [54], Perdew-Burke-Ernzerhof [53] and Wu-Cohen [55].

Being more specific, GGA generally works better than LDA in predicting bond length and binding energy of molecules, crystal lattice constants, and so on, especially in systems where the charge density

is rapidly varying. However GGA sometimes overcorrects LDA results in ionic crystals where the lattice constants from LDA calculations fit well with experimental data but GGA will overestimate them. Nevertheless, both LDA and GGA perform badly in materials where the electrons tend to be localized and strongly correlated such as transition-metal and rare-earth compounds. It is well known that very often the band gap obtained within LDA or GGA is strongly underestimated sometimes even predicting correlated insulators as metallic, due to an underestimation of electron-correlation effects. There are several reasons for this. One problem is that the LDA and GGA functionals contain the self-interaction error and do not show a derivative discontinuity, which is important when one wants to compare the KS band gap (the difference in the eigenvalues of the conduction band minimum and the valence band maximum) with the experimental band gap (the difference between the ionization potential and the electron affinity).

There are alternative ways to obtain an estimate of the experimental band gap. One can use a method that lies outside the KS framework by using a non-multiplicative potential. Hybrid functionals, in which a fraction of exact exchange replaces a fraction of the LDA or GGA exchange, improve the band gap but they are much more expensive and also not satisfactory in all cases. To test their applicability we studied bulk CrN by means of them. Another possibility is the LDA+ $U$  method, applicable to correlated and localized electrons, e.g.  $3d$  and  $4f$  in transition-metal and rare-earth compounds. If one wants to stay inside the KS framework and still use a computationally cheap semilocal method that leads to KS band gaps close to the experimental ones, the newly developed semilocal potentials (such as the one developed by Tran and Blaha based on a modification of the Becke-Johnson potential) can give good results [56–58]. We will analyze the LDA+ $U$  method and the modified Becke-Johnson potential below in further detail since they are the main exchange-correlation potentials used throughout this Thesis.

### 1.4.5.1 LDA+U

For dealing with strong electron correlations, one of the possible alternatives to treat the exchange-correlation functional is the so-called LDA+U approximation [59]. It is based on the LDA but includes a correlation term,  $U$ , imported from the Hubbard model.

The method assumes two different electron subsystems:

- localized electrons, with an on-site Coulomb interaction within the same orbital with the form:  $\frac{1}{2}U \sum_{i \neq j} n_i n_j$ , where  $n_i, n_j$  are the orbital occupancies.
- delocalized electrons, that are described by an orbital-independent potential (LDA).

The LDA+U approximation takes into account the orbital dependence of the electron-electron interactions. Let us consider an ion with  $d$  electrons as a system with a variable number of electrons and we will use the LDA to approximate the exchange-correlation energy as a function of  $N = \sum_i n_i$ , but not for the orbital energies (the eigenvalues). Hence, the total energy is, subtracting a term to take double counting into account:

$$E = E_{LDA} - U \frac{N(N-1)}{2} + \frac{1}{2}U \sum_{i \neq j} n_i n_j \quad (1.17)$$

The orbital energies are, then:

$$\epsilon_i = \frac{\delta E}{\delta n_i} = \epsilon_{LDA} + U \left( \frac{1}{2} - n_i \right) \quad (1.18)$$

So, if

$$\left\{ \begin{array}{l} n_i = 1 \Rightarrow \epsilon_i^{occ} = \epsilon_{LDA} - \frac{U}{2} \\ n_i = 0 \Rightarrow \epsilon_i^{unocc} = \epsilon_{LDA} + \frac{U}{2} \end{array} \right\} \quad (1.19)$$

This produces a separation in energy between an occupied and an unoccupied level of value  $U$ , that gives rise to two energy bands (typically called lower and upper Hubbard bands). This reproduces the

physics of the Mott-Hubbard insulators, that are insulating due to this type of electron-electron interaction as we saw above.

The LDA+ $U$  approximation improves qualitatively with respect to LDA in properties of excited states such as energy gaps, ground-state properties such as magnetic moments or exchange coupling constants, and it gives more precise results for: orbital polarization, Jahn-Teller distortions or polaron formation.

The energy  $U$  which allows to localize electrons is also a gauge of correlation. The exchange-correlation potential of the LDA is based on a homogeneous gas of electrons bearing little resemblance to electrons localized near specific ions. Correlation between these localized electrons will be strongly underestimated through application of the LDA. The degree to which the LDA fails in localized magnetic systems depends largely on the extent of the localization as we mentioned above. At least, the LDA underestimates the gap in insulators, sometimes very badly. The worst results are obtained in  $d$ - and  $f$ -electron systems with partially filled shells (in transition-metal compounds).

The appearance of partly filled bands at the Fermi level needs to be corrected by, e.g., adding a  $U$ -term that produces a lower-lying fully occupied band and a higher-lying fully unoccupied band that mimics the physics of the lower and upper Hubbard bands typical of the Hubbard model. This is what the LDA+ $U$  method that we described above tries to do.

Model Hamiltonians, such as the Hubbard model, have had great success with the same systems which are badly described by the LDA. The different flavors of the Hubbard model provide a good description of systems in the large  $U/t$  limit. There are many models derived from or based on the Hubbard model, the vast majority of which are unsolvable except in very specific instances. However, the appearance of newer and better computational tools gives an approximate solution to this and other model Hamiltonians.

One of the biggest achievements of the LDA+ $U$  method was the prediction of the correct antiferromagnetic insulating state of some

transition-metal compounds, that is not attainable within LDA or GGA alone. This has made the LDA+ $U$  widely used nowadays for calculations on this type of systems: strongly correlated systems in the localized-electron limit. For all these reasons, we will mainly use this method to deal with the strongly correlated electrons of the compounds we have studied.

#### 1.4.5.2 Modified Becke-Johnson potential

The method described above belongs to the so-called generalized KS framework [60] mixing DFT and Hartree-Fock (HF) theories. Nevertheless, if one wants to stay inside the true Kohn Sham framework and use a method that can lead to KS gaps close to the experimental band gaps, the potential proposed by Becke and Johnson (BJ) [61], which was designed to reproduce the exact exchange potential in atoms, can be a good starting point. The multiplicative BJ potential which does not contain any empirical parameters reads:

$$v_x^{BJ}(\vec{r}) = v_x^{BR}(\vec{r}) + \frac{1}{\Pi} \sqrt{\frac{5}{6}} \sqrt{\frac{t(\vec{r})}{\rho(\vec{r})}} \quad (1.20)$$

where

$$t(\vec{r}) = \frac{1}{2} \sum_{i=1}^N \nabla \Psi_i^*(\vec{r}) \cdot \nabla \Psi_i(\vec{r}) \quad (1.21)$$

is the KS kinetic-energy density and

$$v_x^{BR}(\vec{r}) = -\frac{1}{b(\vec{r})} \left( 1 - e^{-x(\vec{r})} - \frac{1}{2} x(\vec{r}) e^{-x(\vec{r})} \right) \quad (1.22)$$

is the Becke Roussel (BR) exchange potential, which was proposed to model the Coulomb potential created by the exchange hole. In equation 1.22,  $x$  is determined from a nonlinear equation involving  $\rho$ ,  $\nabla \rho(\vec{r})$ ,  $\nabla^2 \rho(\vec{r})$  and  $t$ , and  $b$  is calculated with

$$b = \left[ x^3 e^{-x(\vec{r})} / (8\Pi\rho) \right]^{1/3} \quad (1.23)$$

It has been shown that the BJ potential can be further improved for the description of band gaps by using a modified version developed by Tran and Blaha (TB-mBJ) which introduces a parameter to change the relative weights of the two terms in the BJ potential:

$$v_x^{TB-mBJ}(\vec{r}) = cv_x^{BR}(\vec{r}) + (3c - 2) \frac{1}{\Pi} \sqrt{\frac{5}{6}} \sqrt{\frac{t(\vec{r})}{\rho(\vec{r})}} \quad (1.24)$$

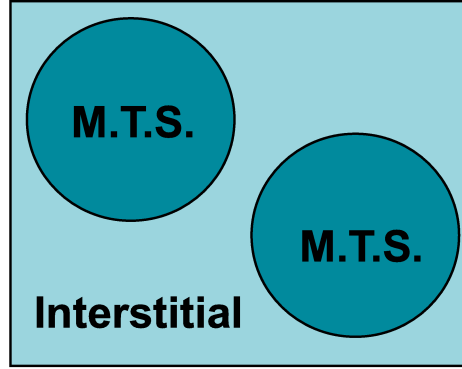
with

$$c = \alpha + \beta \left( \frac{1}{V_{cell}} \int_{cell} \frac{\nabla \rho(\vec{r}')}{\rho(\vec{r}')} d^3r' \right)^{1/2} \quad (1.25)$$

where  $V_{cell}$  is the unit cell volume and  $\alpha$  and  $\beta$  are two free parameters whose values are  $\alpha = -0.012$  and  $\beta = 1.023 \text{ bohr}^{(1/2)}$  according to a fit to experimental results. The way in which this linear combination is written makes sure that for any value of  $c$  the LDA exchange potential is recovered for a constant electron density. For  $c = 1$  the original BJ potential is recovered. This potential has yielded satisfying results for many different systems, including transition-metal compounds [56–58]. This is why we will also apply it to several of the compounds studied throughout this Thesis.

#### 1.4.6 APW+lo method

The APW+lo (augmented plane wave plus local orbitals) is one of the most efficient methods to solve the Kohn-Sham equations. It is a full-potential (no approximation is made to the shape of the potential or the electron density) and all-electron (all the electrons are included in the calculations: core, semicore and valence electrons are calculated and no pseudopotential is used). It is based on the APW method developed by Slater in 1937 [62]. This uses the so-called muffin-tin approximation, that divides the unit cell in two regions: the interstitial part and the muffin-tin spheres centered on the atoms, as can be seen in Fig. 1.2. Muffin-tin radii need to be chosen according to atomic sizes and, unlike other methods, must not overlap.

**Figure 1.2:**

Schematic representation of how the unit cell is divided in the muffin-tin approximation for a case with two atoms. Two different regions appear: the muffin-tin spheres (M.T.S.) around the atoms and the interstitial (I) part between them.

In the interstitial part, the electron density is decomposed in an expansion of plane waves and within the muffin-tin spheres, a combination of solutions of the radial Schrödinger equation is used:

$$\phi(\vec{r}) = \left\{ \begin{array}{ll} \frac{1}{\Omega^{\frac{1}{2}}} \sum_{\vec{G}} c_{\vec{G}} e^{i(\vec{G}+\vec{k})\vec{r}} & \vec{r} \in I \\ \sum_{lm} A_{lm} u_l(r) Y_{lm}(\vec{r}) & \vec{r} \in MTS \end{array} \right\} \quad (1.26)$$

where  $\phi(\vec{r})$  is a wave function,  $\Omega$  is the volume of the cell,  $c_{\vec{G}}$  and  $A_{lm}$  are the coefficients of the expansion and  $u_l(\vec{r})$  is a regular solution of the radial Schrödinger equation. The quality of our description in the interstitial is given by the maximum  $\vec{K}$  vector we use for the plane wave expansion.

The main problem with the APW method is that the basis set is energy-dependent (within the muffin-tin spheres). The basis must be evaluated at the eigenenergies for being efficient, and hence, it must be recalculated at every iteration. A first attempt to create an energy-independent basis set was developed in the 70's by Ole Andersen among others [63, 64], the so-called LAPW method. In LAPW language, the

quantity that controls basis set size is  $R_{mt}K_{max}$  (where  $R_{mt}$  is the minimum muffin-tin radius in this case). The value of  $R_{mt}K_{max}$  needs to be tested for convergence, and it is usually 6 – 7 for the type of systems we will discuss in this Thesis.

A different way to “linearize” the APW method is the Augmented Plane Wave + local orbitals (APW+lo) method [65]. This has been proven to be much faster and efficient than other linearizations of the APW method [66]. It adds so-called local orbitals (local meaning that they vanish at the interstice) to the basis set. These look like:

$$\phi(\vec{r}, \vec{k}) = \left\{ \begin{array}{ll} 0 & \vec{r} \in I \\ (a_L^{lo} u_l(r, E_l) + b_L^{lo} \dot{u}_l(r, E_l)) Y_L(\vec{r}) & \vec{r} \in MTS \end{array} \right\} \quad (1.27)$$

where  $a_L^{lo}$  and  $b_L^{lo}$  are coefficients of the expansion and  $E_l$  are the linearization energies where the solutions of the radial Schrödinger equation are evaluated. The APW’s are, hence, evaluated at a fixed energy (basis set does not need to be updated at every iteration) and the flexibility is added by including these local orbitals in the basis set.

#### 1.4.7 WIEN2k code: computational details

All the electronic-structure calculations in this Thesis were carried out within DFT, using the all-electron, full potential code WIEN2k [67, 68] based on the APW+lo basis set [65]. The WIEN2k package is a computer program written in Fortran which performs quantum mechanical calculations on periodic solids.

This package allows to study most of the electronic structure properties of a crystalline solid: electron density, density of states (DOS), various types of spectra, magnetism (ferromagnetic, antiferromagnetic and non-magnetic configurations), non-collinear magnetism, band structure, Fermi surface, different exchange-correlation potentials including the local density approximation (LDA), various generalized gradient approximation (GGA) (Perdew-Wang [54] or Perdew-Burke-Ernzerhof



[53], Wu-Cohen [55]), meta-GGA [69, 70] and the LDA+ $U$  method [59] in various flavors for the double counting terms, as well as the so-called Tran-Blaha modified Becke-Johnson potential [56], and hybrid functionals. [71]

As we saw above, the modified Becke-Johnson exchange potential (a local approximation to an atomic exact-exchange potential and a screening term) + LDA-correlation allows the calculation of band gaps with an accuracy similar to the much more expensive  $GW$  or hybrid methods. This is the reason why we will apply it to several of the systems studied in this Thesis (bulk CrN and  $\text{La}_2\text{NiO}_4$ ).

For modeling the behavior of the  $d$  electrons of systems in this Thesis, we have also included the strong correlation effects by means of the Local Density Approximation plus Hubbard  $U$  (LDA+ $U$ ) scheme [72], where the correlation effects were controlled by an effective  $U$  ( $U_{eff} = U - J$ ), being  $U$  the on-site Coulomb repulsion and  $J$  the on-site exchange constant [73]. The value of  $U$  is chosen for each particular case based on the correct reproduction of experimental measurements.

The parameter  $R_{mt}K_{max}$  controls the size of the plane-wave basis, and is defined as the product of the plane-wave cut-off and the smallest atomic-sphere radii (muffin-tin radii). We have used an appropriate sampling of the full Brillouin zone for electronic structure calculations and geometry optimization in all the cases. The parameters of our calculations depend on the type of calculation but for any of them we converged with respect to the  $k$ -mesh and to  $R_{mt}K_{max}$ . The parameters of our calculations are always fully converged for every particular case to the required precision.

#### 1.4.8 Definition of the transport coefficients

Along this Thesis we will analyze all sorts of properties extracted from the electronic structure of the materials under study, e.g. different orderings, magnetic properties, structural distortions, and we will pay particular attention to the transport properties. On the one hand,

we will study how different transition-metal compounds change their band structure from metallic to insulating. On the other, we will also explore how the different transport coefficients change and also how to tune them using the mechanisms described above.

As we saw in Section 1.3 , the efficiency of a thermoelectric device is measured by the dimensionless figure of merit  $zT = (S^2\sigma/\kappa)T$ . A modeling of the transport coefficients involved in this equation (let us recall  $S$  is the Seebeck coefficient,  $\sigma$  is the electrical conductivity, and  $\kappa$  is the total thermal conductivity of the material) is needed in the search for improved thermoelectric materials. We will see how to do that from the results of our electronic structure calculations in this Section.

The perturbation of an electric field or a temperature gradient induces electrical or thermal currents in a material. The local relations between the electric field ( $\vec{E}$ ) and the temperature gradient ( $\nabla T$ ) with the corresponding electrical and heat currents ( $\vec{J}$  and  $\vec{J}_Q$ ) for an isotropic solid can be expressed as [74]:

$$\vec{J} = \sigma\vec{E} - S\sigma\nabla T \quad (1.28)$$

$$\vec{J}_Q = S\sigma T\vec{E} - \kappa\nabla T \quad (1.29)$$

where  $\sigma$  is immediately recognized as the electrical conductivity,  $S$  the Seebeck coefficient defined as the voltage gradient produced in a sample by a given temperature gradient when the electrical current is zero and  $\kappa$  is the thermal conductivity whose electronic contribution is defined as the heat current produced per unit of temperature gradient when the electrical current is zero.

#### 1.4.9 Calculation of the transport distribution and coefficients: BoltzTraP code

To evaluate the transport coefficients defined above, we need a microscopic model of the transport process. We will use the semiclassical

approach given by the solution of Boltzmann transport equation in the relaxation time approximation.

In general, the electric current of carriers is defined as:

$$\vec{J} = e \sum_{\vec{k}} f_{\vec{k}} \vec{v}_{\vec{k}} \quad (1.30)$$

where  $e$  is the charge of the carriers. The sum runs over all quantum numbers of the system that, in the case of a crystalline solid, are the three components of the momentum  $\mathbf{k}$ .  $f_{\mathbf{k}}$  is the population of the quantum state labeled with  $\mathbf{k}$  and  $\mathbf{v}_{\mathbf{k}}$  the group velocity associated to that state defined as the gradient in the reciprocal space of the dispersion relation (band structure) of the electrons in the crystal:

$$\vec{v}_{\vec{k}} = \frac{1}{\hbar} \frac{\partial \epsilon_{\vec{k}}}{\partial \vec{k}} \quad (1.31)$$

$f_{\vec{k}}$  is the distribution function which measures the number of carriers in the  $k$ th state in the neighborhood of  $\vec{r}$ . The distribution function can change through the following mechanisms: diffusion, external fields (such as electric and magnetic fields or a temperature gradient) and scattering of the carriers by phonons or localized scattering centers, such as impurities or crystal defects. The population of the state  $\vec{k}$  is the solution of Boltzmann's equation that contains the interplay between all the mechanisms described above:

$$\frac{\partial f_{\vec{k}}}{\partial t} + \vec{v}_{\vec{k}} \cdot \nabla_{\vec{r}} f_{\vec{k}} + \frac{e}{\hbar} \left( \vec{E} + \frac{1}{c} \vec{v}_{\vec{k}} \times \vec{H} \right) \cdot \nabla_{\vec{k}} f_{\vec{k}} = \left( \frac{df_{\vec{k}}}{dt} \right)_{scatt.} \quad (1.32)$$

In the absence of fields, the stationary solution of the Boltzmann's transport equation for fermions is the Fermi distribution function  $f_0(\epsilon_{\vec{k}})$ . Linearizing the above equation, using the relaxation time approximation for the scattering term, and in the absence of magnetic fields and temperature gradients, the population is

$$f_{\vec{k}} = f_0(\epsilon_{\vec{k}}) + e \left( -\frac{\partial f_0}{\partial \epsilon} \right) \tau_{\vec{k}} \vec{v}_{\vec{k}} \vec{E} \quad (1.33)$$

being  $\tau$  the relaxation time. The relaxation time,  $\tau$ , is dependent on both the band index and the  $\vec{k}$  vector direction. It has been shown, however, that to a good approximation, is almost isotropic. In the BoltzTraP code  $\tau$  will be kept constant in the so-called constant scattering time approximation [75]. The code relies on a Fourier expansion of the band energies (obtained from the WIEN2k calculation) and this allows for the calculation of the velocities as Fourier sums that can be efficiently evaluated using fast Fourier transforms.

Using equation 1.33 to calculate the current, the conductivity tensor can be expressed as:

$$\sigma = e^2 \sum_{\vec{k}} \left( -\frac{\partial f_0}{\partial \epsilon} \right) \vec{v}_{\vec{k}} \vec{v}_{\vec{k}} \tau_{\vec{k}} \quad (1.34)$$

Similar expressions can be derived for the Seebeck coefficient and electronic thermal conductivity. For simplicity the transport distribution can be defined,

$$\Xi = \sum_{\vec{k}} \vec{v}_{\vec{k}} \vec{v}_{\vec{k}} \tau_{\vec{k}} \quad (1.35)$$

The transport coefficients involved in  $zT$  can directly be calculated once we have the transport distribution. Using scalar coefficients,

$$\sigma = e^2 \int \Xi(\epsilon) \left( -\frac{\partial f_0}{\partial \epsilon} \right) d\epsilon \quad (1.36)$$

$$S = \frac{e}{T\sigma} \int \Xi(\epsilon) \left( -\frac{\partial f_0}{\partial \epsilon} \right) (\epsilon - \mu) d\epsilon \quad (1.37)$$

$$\kappa = \frac{1}{T} \int \Xi(\epsilon) \left( -\frac{\partial f_0}{\partial \epsilon} \right) (\epsilon - \mu)^2 d\epsilon \quad (1.38)$$

Where  $\mu$  is the chemical potential. Under the assumption that the relaxation time is direction independent, the Seebeck coefficient is

independent of it (as well as the dimensionless thermoelectric figure of merit) and that is the reason why these quantities will be our main focus when analyzing the transport properties during this Thesis. For this type of calculations, a very fine sampling of the Brillouin zone is required, well beyond what is needed for a self-consistent calculation.

## 1.5 Overview of the Thesis

In this PhD Thesis we will study transition-metal compounds, whose electronic properties reside in the vicinity of a metal-to-insulator transition, e.g. small changes in those systems could make them behave as localized or itinerant. They all are different though (from the structural point of view, from rutile-corundum to rocksalt, quasi-one dimensional to layered systems will be studied) and the transition happens for several reasons: structural distortions, magnetic transitions, changes in the chemical bond, etc.

First, in Chapter 2 we will study the changes in electronic and magnetic structure between the low and high temperature phases of  $V_4O_7$  across the metal-insulator transition. We will analyze charge and magnetic order, the nature of the observed structural distortions, the degree of charge disproportionation in both phases and the nature and strength of the magnetic couplings. After that we will describe the electronic structure and transport properties of bulk CrN using a diverse set of exchange-correlation potentials. The electronic properties of this material, close to a metal-insulator transition, have been a matter of discussion due to the controversial results found experimentally. In Chapter 4 we will analyze the electronic structure, special magnetic properties and thermopower of a quasi-one-dimensional oxide,  $Sr_6Co_5O_{15}$ . After understanding how, under what circumstances and to what degree of accuracy we can describe the properties of these bulk materials and predict new ones, we will deepen into several mechanisms of tuning their electronic properties. The enhancement of the thermoelectric response

of  $\text{La}_2\text{NiO}_4$  through hole-doping and strain will be the focus of Chapters 5 and 6, respectively. After that, we will move back to CrN. To elucidate the origin of the experimentally found metallic behavior of the low-temperature phase of this transition-metal nitride, and to analyze what the effects of a material so close to a metal-insulator transition are when it is nanostructured, in Chapter 7 we will study free-standing thin films of CrN. This will allow us to analyze the changes in electronic structure with respect to the material as a bulk and the appearance of new electronic states as a consequence of the nanostructuring process. In Chapter 8 we will also analyze the effects of quantum confining CrN, studying the electronic structure of CrN/MgO multilayers. This will be the best scenario to study the effect of a drastic dimensionality reduction without surface states appearing, that complicate the picture and prevent the study of quantum confinement effects alone.

All this will give us a broad picture of how *ab initio* techniques can be applied to correlated electron systems, how one can design new ways to tune them computationally and what new properties can be predicted for this interesting class of materials.



## Electronic structure of $V_4O_7$ : Charge ordering, metal-insulator transition, and magnetism

“

*The first principle is that you must not fool yourself and you are the easiest person to fool.*

*[Richard P. Feynman]*

”

### 2.1 Introduction

We will focus in this Chapter on describing the electronic structure and magnetic features on both sides of the metal-insulator transition (MIT) of a vanadate:  $V_4O_7$ .

$V_4O_7$  is a member of the homologous series  $V_nO_{2n-1} = V_2O_3 + (n-2)VO_2$  ( $3 \leq n \leq 9$ ), known as Magnéli phase compounds. The structure of the members of this series is based on the rutile unit cell.  $VO_2$ , like several other transition metal dioxides, crystallizes (above room temperature) in the rutile structure [76], characterized by an octahedral

coordination of the V cations by O atoms and a strong metal-metal bonding along the *c*-direction. The crystal structure of V<sub>4</sub>O<sub>7</sub> [77] consists of rutile-like blocks that are infinite in two-dimensions and four VO<sub>6</sub> octahedra wide in the third (see Fig. 2.1). The shear planes between the rutile blocks have the typical local structure for V<sub>2</sub>O<sub>3</sub> [78]. The resulting structure is triclinic, belonging to a  $P\bar{1}$  space group, with four and seven independent V and O sites, respectively. The V sites are split into two groups: V3 and V4, which are at the shear plane, and V1 and V2, at the center of the rutile blocks. Since V3 and V4 octahedra are connected by face sharing, their environment is sesquioxide-like whereas that of V1 and V2 is rutile-like. The cations form two independent chains V3-V1-V1-V3 and V4-V2-V2-V4 running parallel to the pseudorutile *c*-axis (see Fig. 2.1).

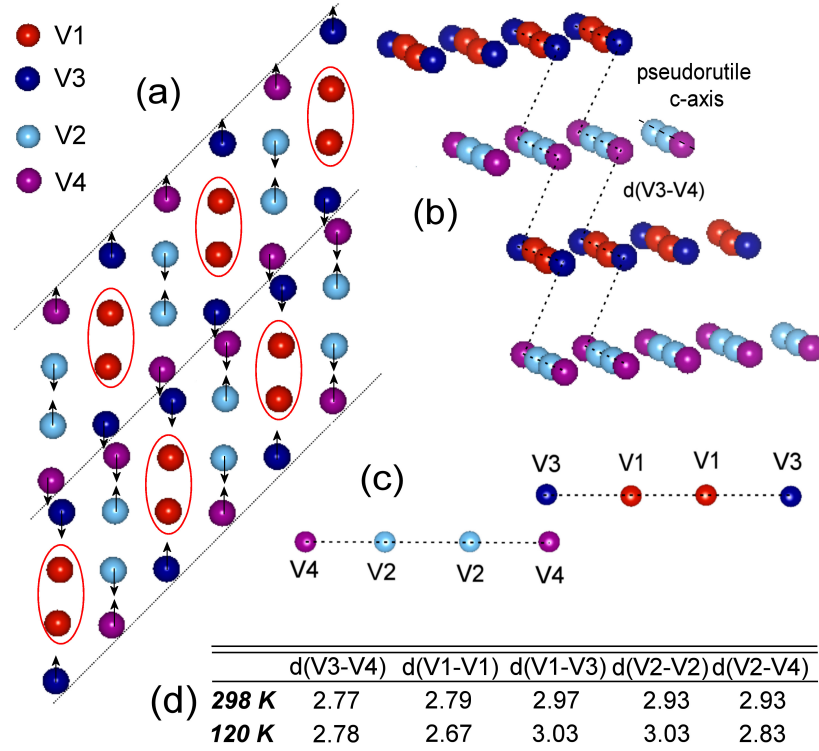
Various members of the series are characterized by a MIT [15]. The physics of the transition in VO<sub>2</sub> has been strongly debated. This is a correlated compound, but the occurrence of a dimerization along the *c*-direction, leading to a formation of spin-singlets due to the Peierls distortion, shows that both correlations and Peierls physics play a role in causing the transition [79–82]. V<sub>4</sub>O<sub>7</sub> shows a weakly first order MIT at 250 K ( $T_c$ ) [83–85]. In this case, the lattice symmetry is unchanged during the phase transition unlike the cases of V<sub>2</sub>O<sub>3</sub> and VO<sub>2</sub> (it is already a low-symmetry structure, bond lengths do change across the transition). The compound also exhibits a paramagnetic to anti-ferromagnetic (AFM) transition at  $T_N \sim 40$  K [86]. The fact that the MIT occurs at a different temperature than the magnetic one allows to think that magnetic order is not a driving force of the phase transition. A simple electron count in V<sub>4</sub>O<sub>7</sub> gives an average valence V<sup>3.5+</sup> for the metal cations. Hence, 2V<sup>3+</sup>(d<sup>2</sup>) and 2V<sup>4+</sup>(d<sup>1</sup>) per formula unit could be expected if CO would occur. Different previous works showed that the metallic state was characterized by an almost complete disorder of the V<sup>3+</sup> and V<sup>4+</sup> cations whereas the insulating state showed a high degree of ordering [84–86]: with the V3-V1-V1-V3 chain being formed by V<sup>4+</sup> ions and the V4-V2-V2-V4 by V<sup>3+</sup> ones. To summarize, CO in the



cation sites occurs below the transition, and this CO state eventually orders magnetically at lower temperatures. Other works point out that the magnetic moments are localized not only in the insulating phase but to some degree also in the metallic one [77]. Most studies show that, in addition to electron localization, half of the V<sup>4+</sup> and all V<sup>3+</sup> cations are paired, forming short V-V bonds along their corresponding chains in the insulating state [77, 84–87]. Another feature of the structural changes occurring at the MIT is the ferro- or antiferroelectric-like shift of unpaired V<sup>4+</sup> ions at the shear planes, from the center of O<sub>6</sub> octahedra towards one of the surrounding oxygens. Such distortion (“twisting”) also occurs in VO<sub>2</sub> [79, 88–90].

Several questions arise when looking at these results. The first is, what is the nature of V pairing in the insulating phase? Similar pairing in VO<sub>2</sub> is largely connected with the orbital repopulation [91]: *d*-electrons, which in the metallic phase above T<sub>c</sub> were more or less equally distributed over all the t<sub>2g</sub>-orbitals, below T<sub>c</sub> occupy predominantly one orbital (d<sub>xy</sub> in the local coordinate system), with the lobes in the *c*-direction, strongly overlapping with neighboring V’s along the chains in the *c*-axis. The resulting one-dimensional electron system is unstable with respect to Peierls, or spin-Peierls dimerization, leading to the formation of singlet V<sup>4+</sup>-V<sup>4+</sup> dimers. There exist many other compounds with transition metal ions with configuration d<sup>1</sup> (containing V<sup>4+</sup>, Ti<sup>3+</sup>, or Nb<sup>4+</sup>) which also form singlet dimers at low temperatures. Thus, we could think that a similar phenomenon could exist also in V<sub>4</sub>O<sub>7</sub>, at least for the V<sup>4+</sup> chains V3-V1-V1-V3. But, in fact, in these segments only the two middle V’s (V1-V1) form singlet dimers, with V3 ions remaining unpaired and apparently magnetic. The question is why is this so.

On the other hand, all the V<sup>3+</sup> in V<sub>4</sub>O<sub>7</sub> form dimers, which is not very typical for V<sup>3+</sup> cations (d<sup>2</sup>, S=1): only very few compounds with V<sup>3+</sup> form dimers. This happens for example in ZnV<sub>2</sub>O<sub>4</sub> [92, 93], but in this case the short V-V dimers are not in a singlet state, but are “ferromagnetic” (FM), i.e. have parallel spins on two V’s. What is the

**Figure 2.1:**

(a) Pseudorutile blocks in  $V_4O_7$ . The lines represent the shear planes. We also show the magnetic structure of the low-temperature phase obtained for  $U=4.1$  eV (the coupling across the shear planes becomes AFM for  $U \geq 5.4$  eV). The ovals around V1 pairs indicate spin-singlet states. (b) View of the chains where the zig-zag of the structure can be seen. (c) Unit cell of  $V_4O_7$ . (d) Table with the different V-V distances (in Å) of the high-temperature (metallic) and low-temperature (insulating) structures at 298 K and 120 K, respectively as obtained in [77].

character of V<sup>3+</sup> dimers in V<sub>4</sub>O<sub>7</sub>, and why these dimers are formed, is an open question.

Another problem is the character and the mechanism of magnetic ordering in V<sub>4</sub>O<sub>7</sub> below T<sub>N</sub> = 40 K. Despite long history of study of V<sub>4</sub>O<sub>7</sub>, its magnetic structure is actually not known. It is also not clear which V ions participate in the magnetic ordering. Apparently, the paired V<sup>4+</sup> ions (V1-V1) are in a singlet state. If V<sup>3+</sup> pairs would also be in a singlet state, then only 1/4 of all the V's, the unpaired V<sup>4+</sup> in V3 position, would be magnetic. But then it would be difficult to understand why such a “dilute” magnetic system, with magnetic ions with small spin S= 1/2 and located far from each other, would give a reasonably high value of the Néel temperature of ~ 40 K. Alternatively, it is possible that the spins of the V<sup>3+</sup> ions are not completely quenched, and that these ions also contribute to magnetic ordering.

In order to shed light on the issues of charge and magnetic order and on the nature of the observed structural distortions, to analyze what degree of charge disproportionation exists in both phases and also what is the nature and strength of each of the magnetic couplings, we will study in this Chapter the electronic structure of both metallic and insulating phases of V<sub>4</sub>O<sub>7</sub> by means of *ab initio* calculations. Besides CO, we have obtained the specific orbital ordering (OO) in the insulating phase, which allows to explain the distortion pattern observed in it. We have also analyzed the plausible magnetic configurations and have discussed the magnetic properties of both low and high-temperature phases [94].

## 2.2 Computational details

For this system, we have used the LDA+*U* approach with the on-site Coulomb repulsion  $U= 4.1$  eV and the on-site Hund's rule coupling  $J= 0.7$  eV. Results presented here are consistent for values of  $U$  in the interval from about 3 to 5 eV, a reasonable range according to previous similar calculations of V<sup>4+</sup> compounds [38, 39] and also of V<sup>3+</sup>

compounds [92]. The calculations were fully converged with respect to the k-mesh and  $R_{mt}K_{max}$ . Values used for the k-mesh were  $5 \times 4 \times 4$  sampling of the full Brillouin zone.  $R_{mt}K_{max} = 6.0$  was chosen for all the calculations. Selected muffin tin radii were the following: 1.72 a.u. for V, and 1.53 a.u. for O in the low-T structure and in the high-T phase, 1.77 a.u. for V, and 1.57 a.u. for O.

## 2.3 Results

### 2.3.1 Structure

We have taken the structural data for both the metallic phase (at 298 K) and the insulating one (at 120 K) from the work of Hodeau and Marezio [77]. The main structural features are depicted in Fig. 2.1. The two phases comprise different V-V and V-O distances (the V-V distances are shown in Fig. 2.1(d), the V-O distances are presented in Table 2.1). As can be seen, in the V4-V2-V2-V4 chain of the metallic phase, the cations are equidistant. In the insulating state, the V2-V4 distance becomes shorter than the V2-V2 one, favoring a possible V2-V4 pairing. An even larger change occurs in the V3-V1-V1-V3 chain distances from the high to the low-temperature structure, with the V1-V1 distance becoming much shorter at lower temperatures. The distance between chains remains almost unchanged across the MIT.

According to the analysis performed in [77] by doing bond-length summations with the experimental structural data, the high temperature metallic state is not comprised of completely disordered  $V^{3+}$ ,  $V^{4+}$  cations. The 4224 chains contain around a 58% of the  $V^{3+}$  cations whereas the 3113 chains contain the same amount of the  $V^{4+}$  ones. Hence, in each chain, even in the metallic state, there remains some charge segregation, but a rather weak one. In the insulating phase, the 4224 chains become richer in 3+ cations (about 83%), V2 having a valence of 3.24+, and V4 a valence of 3.09+. Meanwhile, the 3113 chain has 83% of the  $V^{4+}$  cations, each of them having a valence of

**Table 2.1:**

Interatomic distances between V and O atoms (in Å) in V<sub>4</sub>O<sub>7</sub> for both the low-temperature (120 K) and high-temperature (298 K) phases. Structural data are taken from [77].

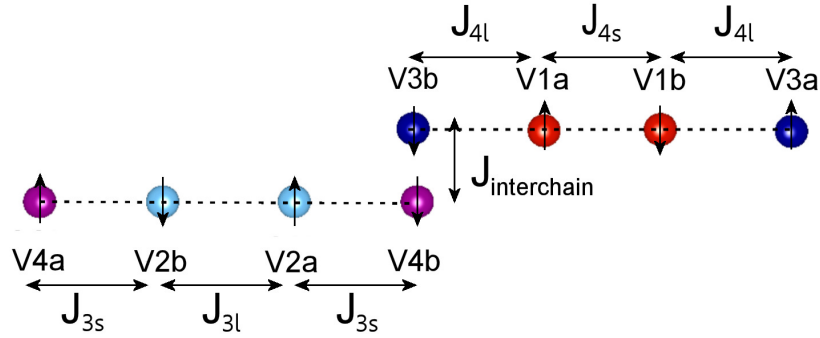
	120 K	298 K		120 K	298 K
d(V1-O2)	1.81	1.88	d(V3-O3)	1.73	1.78
d(V1-O1)	1.88	1.89	d(V3-O6)	1.92	1.94
d(V1-O1)	1.92	1.93	d(V3-O5)	1.95	1.96
d(V1-O6)	1.94	2.05	d(V3-O7)	1.99	1.98
d(V1-O4)	2.05	2.02	d(V3-O4)	2.01	2.03
d(V1-O5)	2.06	2.03	d(V3-O5)	2.15	2.12
d(V2-O1)	1.91	1.90	d(V4-O6)	1.90	1.81
d(V2-O2)	1.94	1.95	d(V4-O5)	1.96	1.97
d(V2-O4)	2.00	2.03	d(V4-O7)	1.98	1.97
d(V2-O7)	2.00	2.02	d(V4-O2)	2.00	1.94
d(V2-O3)	2.03	1.97	d(V4-O7)	2.08	2.12
d(V2-O3)	2.05	2.01	d(V4-O4)	2.13	2.10

3.83+. Thus, the low-temperature insulating state is characterized by the ordering of the V<sup>3+</sup> and V<sup>4+</sup> cations over the four cation sites and by the pairing of half of the V<sup>4+</sup> (those in V1 positions), and of all the V<sup>3+</sup> in the short V-V bonds along the corresponding chains. The remaining unpaired V<sup>4+</sup> ions (V3), on the other hand, shift from the centers of the corresponding O<sub>6</sub> octahedra, forming one very short V-O bond (V3-O3) of less than 1.8 Å, as can be seen in Table 2.1.

### 2.3.2 Electronic structure

#### B1. Low temperature phase

The electronic structure of the low-temperature phase of V<sub>4</sub>O<sub>7</sub> can be roughly understood by analyzing the short-long V-V bonds alternating in the structure. These, in particular, modify the magnetic couplings, and also the distinct charge and orbital states for the V cations that such a structure might lead to. In order to analyze the electronic structure of the low temperature phase of the compound, we have performed

**Figure 2.2:**

Magnetic couplings in the unit cell for the low-temperature structure. The AFM in-chain couplings and the inter-chain FM one (stable at lower values of  $U$  but very small in value) can be seen.

LDA+ $U$  calculations for several values of  $U$  (3.4 - 5.4 eV). For all the  $U$  values, the most stable solutions have in-chain antiferromagnetic (AFM) couplings. By increasing the  $U$  value, the inter-chain coupling, even though always almost negligible in value, switches from FM for lower  $U$  values to AFM for  $U \geq 5.4$  eV. The magnetic ground state (consistent with the in-chain couplings for  $U$  ranging from 3.4 to 5.4 eV) can be seen in Figs. 2.1(a) and 2.2. Table 2.2 shows the magnetic moments of each V cation in the low-temperature structure obtained for  $U = 4.1$  eV. From the charge/moment analysis, CO looks substantial. In the  $V^{4+}$ (3113) chains, the V magnetic moments inside the muffin-tin spheres are about  $0.8 \mu_B$ , whereas for the  $V^{3+}$ (4224) chains the moments are of about  $1.4 \mu_B$ , slightly smaller than twice the value of  $V^{4+}$ , that would be the case in a fully CO state. No noticeable difference in moment is observed between V2 and V4, in contrast to the result of bond length summations that predict a slight difference in valence. The point charge model works very well, but hybridization also plays a role in determining the charge states and magnetic moments.

Further indications of the large degree of CO, very close to a  $d^1/d^2$  state in the corresponding chains, come from the study of the band

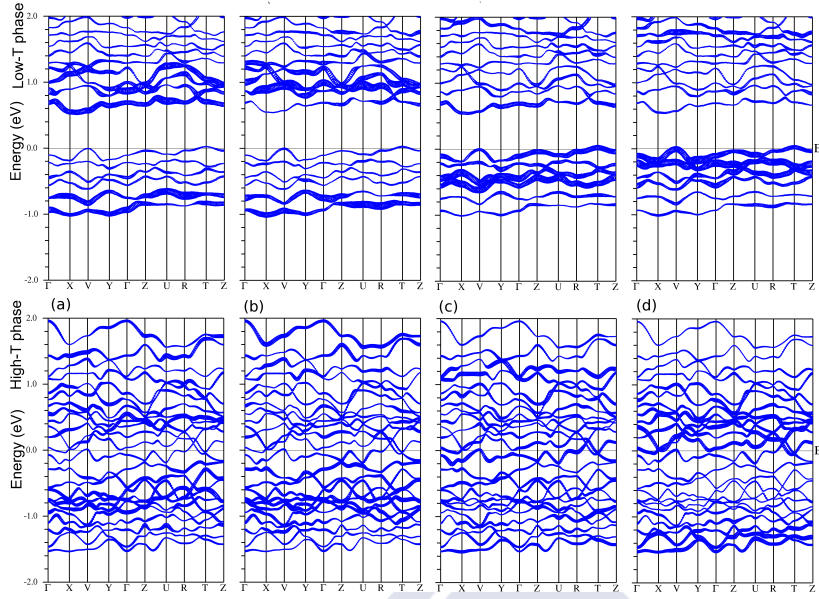
**Table 2.2:**

Projection of the spin magnetic moments of V atoms inside the muffin-tin spheres in the V<sub>4</sub>O<sub>7</sub> magnetic ground state for the low temperature AFM insulating phase and for the high temperature FM metallic one.

Low-T phase		High-T phase	
Atom	Magnetic Moment	Atom	Magnetic Moment
V1a(b)	0.8(-0.8) $\mu_B$	V1	1.3 $\mu_B$
V2a(b)	1.4(-1.4) $\mu_B$	V2	1.4 $\mu_B$
V3a(b)	0.8(-0.8) $\mu_B$	V3	1.2 $\mu_B$
V4a(b)	1.4(-1.4) $\mu_B$	V4	1.2 $\mu_B$

structure plots with band-character (the so called “fat-bands” plots) shown in the upper panels of Fig. 2.3. A band structure plot is often a more reliable tool to analyze charge states in localized electron systems than a simple electron count inside the muffin-tin spheres. The total charge in both cases would be very similar, causing the very small difference in total energy observed experimentally, but the electronic structure and magnetic moments can be very different. This phase is an insulating one with a  $d-d$  gap of about 0.6 eV, for this particular value of  $U$  (4.1 eV). About 1 eV below the Fermi level, only d-bands are observed, with the O states much lower (starting at about -2.5 eV), as occurs in other vanadates like VO<sub>2</sub> [39], SrVO<sub>3</sub> [40], simplifying the picture. We observe, on the upper left two panels of Fig. 2.3, two cations with a  $d^1$  configuration (these are the cations in the V<sup>4+</sup>-chain) and, on the right two panels, other two cations with a distinct  $d^2$  electronic configuration (those at the V<sup>3+</sup> chains). The “fat-bands” plots clearly show one band occupied for the V<sup>4+</sup> cations, and two for the V<sup>3+</sup> ones. Close above the Fermi level, for each spin channel, six unoccupied bands can be observed, four of them from the V<sup>4+</sup>:  $d^1$  cations and, split, two from the V<sup>3+</sup>:  $d^2$  cations.

We can also describe the electronic structure of the material based on the partial density of states (DOS) plots of the various V cations in the low-T structure (see left panels of Fig. 2.4). The different DOS

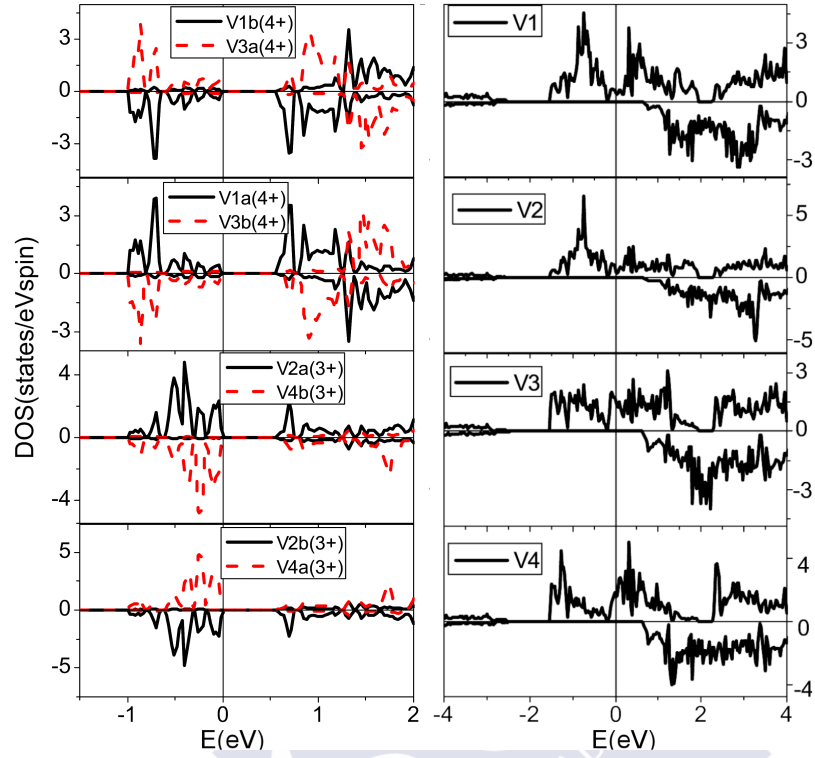
**Figure 2.3:**

The upper panels show the band structure plots with band-character of the majority states for the V cations in the low-temperature insulating phase. (a) Represents the bandstructure plot of the spin-up(down) channel of V1a(V1b), (b) of the spin-up(down) channel of V3a(V3b), (c) of the spin-up(down) channel of V2a(V2b) and (d) of the spin-up(down) channel of V4a(V4b). The differences in the band structure plots for the  $V^{3+}$  (V2 and V4) and the  $V^{4+}$  (V1 and V3) cations can be observed. The lower panels show the same plots for the majority (up) states for the V cations in the high-temperature metallic phase (a) for V1, (b) for V2, (c) for V3, and (d) for V4.

plots for  $V^{4+}$  and  $V^{3+}$  cations can also be observed, with a different position of the occupied bands with respect to the Fermi level: the relatively narrow  $V^{4+}$  bands lie lower in energy, and the broader and more occupied bands corresponding to the  $V^{3+}$  cations are closer to the Fermi level. The DOS integrations inside the muffin-tin spheres give a less distinct picture of the CO phenomenon than the band structures, which are much clearer.

In order to give further evidence of the large CO character of the low-temperature phase, we can consider a three-dimensional representation of the spin density; this also shows which orbitals are occupied at



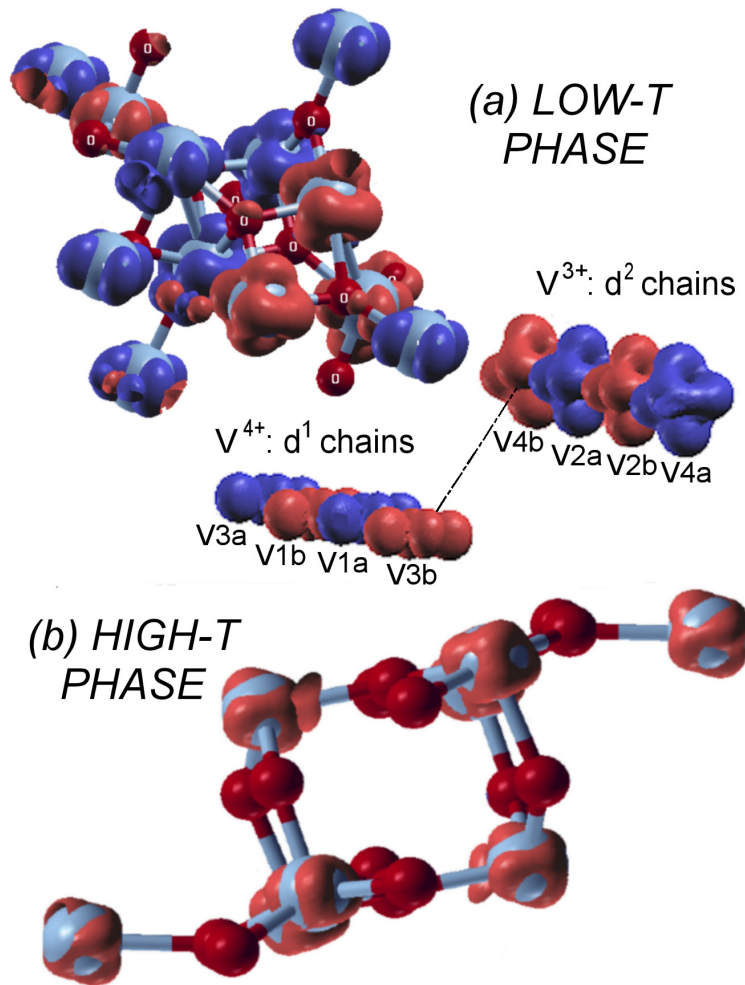


**Figure 2.4:**

Left panels represent the partial DOS for each V cation in the low-temperature phase, where a charge disproportionation effect is clear. Right panels represent that of the V cations in the high-T structure; the different environment leads to a different DOS in each site, but the electron count is similar for all of them. Positive (negative) values indicate up-spin (down-spin) DOS.

each site, i.e. it allows to find the OO. In Fig. 2.5(a) such representation is shown for  $U = 4.1$  eV.

Quite different spin densities (those of  $V^{3+}/V^{4+}$  cations) along the corresponding chains can be seen. The spin density of the  $V^{3+}(d^2)$  cations corresponds to that of a mixture of  $d_{xz}$  and  $d_{yz}$  orbitals, whereas for the  $V^{4+}(d^1)$  it can be interpreted as a  $d_{xy}$  orbital, using a local

**Figure 2.5:**

Three-dimensional plot of the spin density of the magnetic ground states for both high-T and low-T phases of  $V_4O_7$ , isosurface at  $0.1 e/\text{\AA}^3$  obtained using XCrysDen [95]. (a) Represents the plot for the low-temperature phase. Different colors (grayscale) represent spin-up(down) density. The upper panel in (a) shows the density plot for V and O atoms in the unit cell. The lower panel shows the CO character ( $d^1/d^2$ ) along each chain in the structure (neither V nor O atoms have been depicted for simplicity). (b) Represents the spin-density plot for the high-temperature metallic phase. All V atoms exhibit a very similar spin density.

coordinate system with the z-axis directed from V towards its apical oxygen.

In principle, one would expect the local octahedral environments of the V<sup>4+</sup> and V<sup>3+</sup> cations to be distorted accordingly, to accommodate one electron in the  $d_{xy}$  singlet or two in the  $d_{xz}$ ,  $d_{yz}$  doublet. However, the distances we have summarized in Table 2.1 suggest complicated distortions of the VO<sub>6</sub> octahedra, which make it difficult to predict on the basis of only local distortions which orbitals would be occupied [96], without analyzing the results of the calculations. Also, in rutile-based structures, an important part of the crystal field comes from neighboring V cations.

On the basis of these results, one can suggest a possible explanation of the origin of the structural distortions found in V<sub>4</sub>O<sub>7</sub> below T<sub>c</sub>. V<sup>4+</sup> ions occupy two types of positions: V1 in the middle of rutile-like chains, and V3 at the shear plane. When one electron occupies the  $d_{xy}$  orbital in V<sup>4+</sup> atoms, which occurs below T<sub>c</sub>, there exists strong direct overlap of these orbitals along the chain, which can give rise to a metal-metal bonding of V1 ions, like that in the singlet dimers in the insulating phase of VO<sub>2</sub> [97]. However, the V<sup>4+</sup> ions in V3 positions are in a different situation: they have a common face with V4 across the shear plane. In this situation, as argued by Goodenough [79], the main instability of these ions would be the shift of such V<sup>4+</sup> from the center of its O<sub>6</sub> octahedron (ferro- or antiferroelectric distortion). Indeed, as one sees from Table 2.1, just for this V there exists one very short V-O distance, V3-O3, of 1.73 Å; all the other V-O distances are larger and more or less equal. Thus, in the structure of V<sub>4</sub>O<sub>7</sub>, with shear planes every four sites and with the obtained charge and OO, we would have an (anti)ferroelectric-type displacement of the “edge” V3 ions, but the “inner” V<sup>4+</sup> ions V1 would form short, presumably singlet (see below) dimers. The situation here resembles somewhat the M2 phase of VO<sub>2</sub> [88–90], in which also half of V<sup>4+</sup> ions form singlet dimers, but the other half has no dimerization, but has instead an antiferroelectric-type distortion (“twisting”) with the formation of one short V-O bond.

The OO in V<sup>3+</sup> ions, obtained in our calculations, is, however, quite different from that in V<sup>4+</sup> cations: in V<sup>3+</sup> not d<sub>xy</sub>, but rather two other orbitals, d<sub>xz</sub> and d<sub>yz</sub>, are occupied by two electrons in the low-temperature phase. These electrons do not have strong direct d-d overlap, but they can instead hop via bridging oxygens. By that process, the d<sub>xz</sub> electron from one site hops to a d<sub>yz</sub> orbital of the neighboring V, as sketched in Fig. 2.6, where we show the V<sup>3+</sup> chain running along the c-direction in a more convenient projection. One sees indeed that e.g. the xz-electron from the site V4a can hop to a yz-state of the site V2b via a p<sub>z</sub> orbital of the oxygen *a*, and then again to the xz-orbital of the site V2a via the p<sub>z</sub> orbital of oxygen *d*. Similarly, there will exist hopping (yz)<sub>V4a</sub> - (p<sub>z</sub>)<sub>b</sub> - (xz)<sub>V2b</sub> - (p<sub>z</sub>)<sub>c</sub> - (yz)<sub>V2a</sub> . . . . As a result, we would have two degenerate half-filled one-dimensional (1D) bands (containing two electrons per V<sup>3+</sup>). Such 1D bands would naturally give rise to a Peierls dimerization, which would open the gap in the spectrum and would decrease the energy [22]. This is a possible explanation of the formation of dimers (V4-V2) and (V2-V4) in V<sub>4</sub>O<sub>7</sub>. Similar dimerization was recently found in the rutile-like V<sup>3+</sup> chains in vanadium hollandite K<sub>2</sub>V<sub>8</sub>O<sub>16</sub> [98], apparently due to the same mechanism.

## B2. Magnetic order

To analyze the possibility and the consequences of pairing of V atoms along each chain and to understand the magnetic properties of the compound, we have calculated the strength of the magnetic couplings in the unit cell. Two kinds of couplings can be considered in each chain (one short (s) and one long (l)) plus the inter-chain coupling (see Fig. 2.2). We have used our total energy calculations for different collinear magnetic configurations to quantify and describe these couplings. To that end, we have fit the total energies to a Heisenberg model, in the form  $H = \frac{1}{2} \sum_{i,j} J_{ij} S_i S_j$ , with S=1 for the V<sup>3+</sup> sites and S=1/2 for the V<sup>4+</sup> ones. The V<sup>4+</sup>(d<sup>1</sup>) sites would be expected to undergo singlet

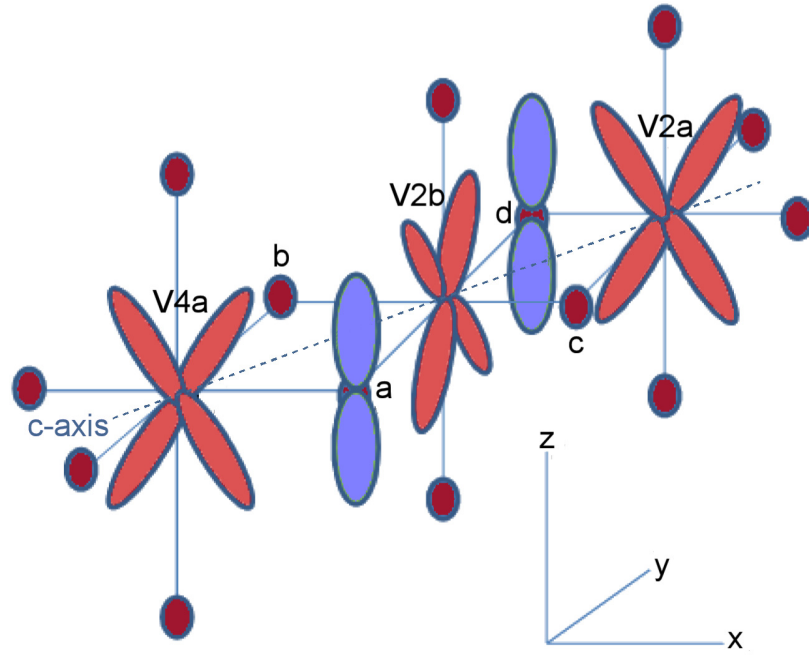


**Figure 2.6:**

Schematic representation of the possible hopping processes along the  $V^{3+}$  chains in the  $c$ -direction. Due to the  $d^2$  electronic structure of these cations, the magnetic interactions are mediated by bridging O  $p$ -orbitals, contrary to the direct V-V bond (not shown) that occurs in the  $V^{4+}$ - $V^{4+}$  chains.

spin pairing whereas the  $V^{3+}(d^2)$  ones could pair in singlet, triplet or quintuplet spin states. The values of the in-chain coupling constants, obtained in our calculations, are:  $J_{3l} \approx 40$  K,  $J_{3s} \approx 100$  K,  $J_{4l} \approx 10$  K and  $J_{4s} \approx 1000$  K (3 and 4 stand for  $V^{3+}$  and  $V^{4+}$  chains, respectively, and “l/s” stand for the long and short bonds).

The short-bond magnetic coupling between paired  $V^{4+}$  cations ( $J_{4s}$ ) is very large,  $\approx 1000$  K, indicating that most probably these ions form spin singlet states, reminiscent of the ordering along the  $c$ -axis that happens in  $VO_2$  [82]. The situation is different in  $V^{3+}$  chains, where also the short-bond magnetic coupling ( $J_{3s}$ ) is larger than that in the

long bond ( $J_{3l}$ ), but the difference is not as drastic as in the  $V^{4+}$  chains. This suggests that spin singlets would not be formed in the  $V^{3+}$  chains. The magnetic coupling strength between chains is quite small, but apparently sufficient to form long-range magnetic ordering below  $T_N = 40$  K. We can thus propose that the magnetic structure of this state may be the AFM ordering in  $V^{3+}$  segments, coupled to  $V^{4+}$  ions V3 with unpaired spins (see Figs. 2.2 and 2.1(a)). Due to the very small inter-chain magnetic coupling, two  $V^{4+}$  cations per chain (V3) could be left partially disordered, even at low temperatures.

Previous works [85, 87] give further support to the importance of the pairing interactions as one of the driving forces for the MIT. In the work by Gossard *et al.* [85], the pairing in the  $V^{4+}$  chain (corresponding to our  $J_{4s}$ ) becomes complete only below 150 K (100 K below the MIT transition). The magnetic coupling  $J_{4s}$  estimated using their nuclear-resonance frequency shifts is also large ( $J \sim 500$  K at 100 K). The nuclear magnetic resonance (NMR) spectrum of spin-echo amplitudes observed at 4.2 K implies a continuous singlet spin pairing in the AFM state, with the singlet  $V^{4+}$  spin-pairs unbroken by the AFM ordering. This is in agreement with our picture.

In addition, the possible formation of singlet spin pairs along the  $V^{3+}$  chains has been discussed previously [85]. Due to the two echo lines appearing in the NMR spectrum one possibility is that i) one line arises from unpaired  $V^{4+}$  with a moment of  $1 \mu_B$ , while the other comes from paired  $V^{3+}$  atoms which have reduced moments of  $1 \mu_B$ , due to covalent singlet bonding of one of their two 3d electrons. The other option is: ii) both lines arise from unpaired  $4+$  atoms that may have become crystallographically inequivalent in the AFM state. Structural results [77] at 120 K, above the magnetic order temperature ( $T_N$ ), indicate the unpaired  $V^{4+}$  at the shear planes are not inequivalent. Heidemann *et al.* [87] gave further confirmation of the option i) and hence of the partial singlet spin pairing in the  $V^{3+}$  chains, possibly with some magnetism thereof remaining.

From our calculations, we can argue that although  $J_{3s}$  is larger than the coupling of  $V^{3+}$  spins in the long bond, we do not expect real spin singlets to be formed in the  $V^{3+}$  chains, but a more complicated spin structure is expected to develop. From our calculations, we can see that the magnetic moments obtained for the  $V^{3+}(d^2)$  atoms are reduced by hybridizations from the purely ionic picture. Also, the magnetic moment of these cations barely changes across the transition, as we saw in Table 2.2. Thus we propose that both  $V^{3+}$  and half of  $V^{4+}$  ions (those in V3 positions) participate in long-range magnetic ordering (see Fig. 2.1(a)).

### **B3. High temperature phase**

The electronic structure of the high temperature/metallic phase does not present the large charge-ordering character, as the bond-length summations correctly suggest [77]. We have performed LDA+U calculations for the same magnetic configurations used for the low-temperature structure with the same  $U$  values. The magnetic ground state is now FM and all the sites are almost equivalent: the electronic structure is close to  $V^{3.5+}$  for all the atoms in the structure. The magnetic moments of the ground state solution that can be seen in Table 2.2 are consistent with this picture. Some difference is seen in the magnetic moments due to the different bandwidths of the respective d-bands, caused by the different environments the V cations are in, but no trace of CO remains at high temperature, leading to a metallic solution. Also, by looking at the band structures with “fat-bands” (lower panels of Fig. 2.3), we do not see the clear  $d^1/d^2$  ionic picture we observe in the insulating low-temperature phase. The FM high-temperature band structure is consistent with the absence of charge-ordering we are describing, since it shows more evenly distributed occupations in different bands. The spin-density plot for the high-temperature phase (see Fig. 2.5(b)) gives further evidence of this absence, confirming a non-integer charge occupation (roughly  $V^{3.5+}$ ) at all the V sites. Even though a different DOS is seen for each of the V sites in the high-temperature structure (right

panels of Fig. 2.4), the electron count is very similar for each of them, as the “fat bands” and magnetic moments also show. The FM ordering (or paramagnetic state experimentally found at high temperatures) also increases the bandwidths when compared to the low-temperature CO AFM phase. The absence of CO is supported by experimental works [77, 85, 87]. The high-temperature susceptibility data for V<sub>4</sub>O<sub>7</sub> [85, 87] are not conclusive about the sign of the Curie-Weiss temperature due to the high transition temperature. Our calculations suggest a change to a FM nature of the in-chain couplings in the high-temperature phase.

### 2.3.3 Conclusions

Thus we see that, in analogy with VO<sub>2</sub>, in the V<sup>4+</sup> chains there occurs an OO facilitating singlet pair formation. Also, the analysis of the electronic structure helps to understand why only the inner (V1-V1) V<sup>4+</sup> ions form such pairs, whereas (V4-V2) and (V2-V4) pairs are formed in V<sup>3+</sup> chains. This has to do with the orbital occupation in the V<sup>3+</sup> chains, different from that in the V<sup>4+</sup> chains: two orbitals,  $d_{xz}$  and  $d_{yz}$ , are occupied by two electrons at these sites, in contrast to  $d_{xy}$  orbital occupation in V<sup>4+</sup> chains. Apparently, this is responsible for a somewhat weaker dimerization (the changes in the V-V distance across the CO transition are,  $\Delta(V4-V2)_{high-T,low-T} = 0.1 \text{ \AA}$ , as compared with  $\Delta(V1-V1)_{high-T,low-T} = 0.12 \text{ \AA}$ , see Fig. 1d). This also leads to smaller modulation of the exchange constants within the V<sup>3+</sup> chains ( $J_{short} = 100 \text{ K}$  vs  $J_{long} = 40 \text{ K}$ ), whereas this difference is much larger in V<sup>4+</sup> segments ( $J_{short} = 1000 \text{ K}$  vs  $J_{long} = 10 \text{ K}$ ). As a result, apparently V<sup>3+</sup> ions do not form singlets, despite dimerization, but participate in magnetic ordering, together with unpaired V<sup>4+</sup> (V3) ions. This can explain the appearance of magnetic ordering at a relatively high temperature  $T_N = 40 \text{ K}$ .



## 2.4 Summary

We have studied the electronic structure of V<sub>4</sub>O<sub>7</sub> analyzing the differences between the low-temperature (charge ordered, antiferromagnetic ordered and insulating) and the high-temperature (charge disordered, paramagnetic and metallic) phases.

Calculations show the strong CO in the low-temperature phase that, together with structural distortions, lead to a gap opening. The high-temperature structure is charge disordered, with all V atoms in a similar  $\sim d^{1.5}$  electronic configuration. All the in-chain magnetic couplings in the low-temperature phase are AFM, and the inter-chain couplings are very weak (and of different signs depending on the  $U$ -value). Magnetic coupling changes to FM in the high-temperature phase as a result of the change in electron distribution caused by charge disorder. The AFM couplings in the low-temperature phase are obtained, being very strong in the V<sup>4+</sup>-V<sup>4+</sup> short bonds, one order of magnitude stronger than the short V<sup>3+</sup>-V<sup>3+</sup> magnetic couplings (and two orders of magnitude stronger than in the V<sup>4+</sup>-V<sup>4+</sup> long bonds). This suggests the formation of a spin-singlet between the “middle” V’s within the V<sup>4+</sup> chains, leaving V<sup>3+</sup> atoms with unpaired spins. The couplings in the V<sup>3+</sup> chains are more complicated, showing signs of slight moment reduction due to hybridizations.

The OO obtained in our electronic structure calculations (V<sup>4+</sup>:  $d_{xy}$  vs. V<sup>3+</sup>:  $d_{xz}, d_{yz}$ ) also helps to understand the different bond distance alternations that occur in the two different types of V chains: in the V<sup>4+</sup> chains there is a strong metal-metal bond between the “middle” V<sup>4+</sup> ions forming spin singlets, and an (anti)ferroelectric-type displacement of the “edge” V<sup>4+</sup> ions at the shear planes. On the other hand, the V<sup>3+</sup> chains, due to different orbital occupation, form two one-dimensional-like bands due to bridging with oxygens, that affects the type of coupling along these chains and leads, in particular, to a dimerization of V<sup>3+</sup> chains, which, however, is not strong enough to make the short V<sup>3+</sup>-V<sup>3+</sup> dimers spin singlets.

As a result, most probably both the unpaired “edge”  $V^{4+}$  and all  $V^{3+}$  ions contribute to magnetic ordering below  $T_N$ , the detailed type of which is yet unknown.



## Electronic structure of bulk CrN: A comparison between different exchange correlation potentials

“

*The scientist does not study nature because it is useful to do so. He studies it because he takes pleasure in it, and he takes pleasure in it because it is beautiful.*

*[Henri Poincaré]*

”

### 3.1 Introduction

We will now focus on describing the electronic structure of a transition metal nitride (TMN) that has been shown to be very close to a transition from a localized to an itinerant electronic behavior driven in this particular case by a magnetostructural phase transition. The electronic properties of this material, due to this closeness to a metal-insulator transition, have been a matter of discussion and controversial results have been found experimentally.

TMN have drawn considerable attention due to their interesting physical properties: mechanical strength, ultrahardness, corrosion resistance, high melting points, good electrical and thermal conductivities, etc [99]. In addition, some TMN exhibit other properties such as superconductivity (arising in VN [100] and NbN [101, 102], a transition from a superconductor to a Cooper pair insulator in TiN [103].

CrN has attracted much attention due to its interesting physical properties. It shows a magnetostructural phase transition (MPT) as a function of temperature from an orthorhombic antiferromagnetic (AFM) phase to a cubic paramagnetic (PM) one at a Néel temperature  $T_N \sim 273\text{-}286$  K [104]. The low- $T$  AFM configuration is quite unique consisting of double ferromagnetic (FM) layers stacked antiferromagnetically along the [110] direction (see AFM2 in the right panel of Fig. 3.1). This peculiar magnetic structure has been shown to be linked to the structural distortion across  $T_N$  [105, 106]. However, some experimental works show the suppression of the phase transition due to epitaxial constraints when grown in films with the system remaining in the cubic phase at all temperatures [107–109]. CrN also exhibits high thermal stability, corrosion resistance, and excellent mechanical properties that have recently been shown to be susceptible to improvements if somehow one can force the system to remain in the harder AFM configuration [23]. All this combined with the ease of film deposition and promising thermoelectric properties make this compound a good source of different physical properties [110, 111]. In spite of its simple structure and the amount of work accumulated over the years, it is still a ground for contention among different pictures, both of its conduction and electronic properties.

The main focus of controversy has been the understanding of CrN electrical behavior. On the one hand, the values of the resistivity at room temperature vary over several orders of magnitude (from  $\text{m}\Omega\text{cm}$  to  $\text{k}\Omega\text{cm}$ ) in different works [107, 109–117]. On the other, the nature of the transition in terms of the electrical conduction behavior has had a wide range of interpretations in the literature. At least three different

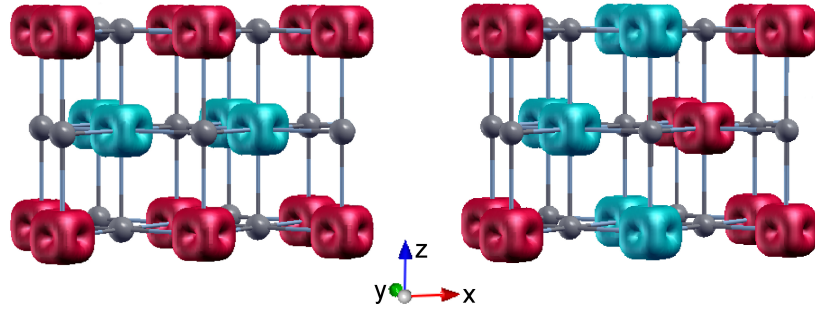


**Figure 3.1:**

Three dimensional plot showing the difference between the spin-up and spin-down (different color) electron densities in the AFM1 (left panel) and AFM2 (right panel) phases. The typical  $d^3(t_{2g}^3)$  electronic configuration of each  $\text{Cr}^{3+}$  cation and no magnetic polarization in neighboring ligands can be observed.

points of view can be found to describe the nature of the MPT, which we summarize as follows:

*Metal to metal.* In the work of Tsuchiya *et al.* [117], polycrystalline  $\text{CrN}_{1+x}$  films with  $0 \leq x \leq 0.2$  have been grown by reactive sputtering. Nearly stoichiometric films show an AFM first order phase transition at  $T_N \sim 260$  K. Resistivity measurements for these samples indicated metallic behavior across  $T_N$  with a steep decrease of the resistivity below the transition. The same behavior was found by Browne *et al.* [118] in CrN powder. In the study of Inumaru *et al.* [108], CrN films were epitaxially grown on  $\alpha\text{-Al}_2\text{O}_3$  (0001) and MgO (001) substrates by pulsed laser deposition. The films grown on  $\alpha\text{-Al}_2\text{O}_3$  (0001) with their (111) planes parallel to the substrate show no structural transition whereas CrN(001) films grown on MgO (001) show a transition to an AFM state at about 260 K. Both types of films exhibit metallic  $T$ -dependence of the resistivity, but a drop in its values below the Néel temperature is observed for the samples showing a MPT.

*Metal to semiconductor.* Constantin *et al.* [114] grew CrN(001) thin films on MgO(001) using molecular beam epitaxy. The films show a

MPT at 285 K, with activated semiconducting behavior above  $T_N$  and a band gap of 0.07 eV. Below the transition temperature, the films are metallic. The polycrystalline samples of CrN prepared by Bhohe *et al.*[113] show a MPT at 286 K. Above  $T_N$ , CrN exhibits activated semiconducting behavior (with a gap of 0.07 eV) becoming a disordered metal below  $T_N$ . Evidences of strong electron-electron correlations were found, determining an on-site Coulomb energy ( $U$ ) of 4.5 eV by interpreting resonant photoemission spectroscopy (PES) data. In [109] both single and polycrystalline CrN layers have been grown by reactive sputtering deposition on both MgO and quartz substrates. Polycrystalline CrN did show a disorder induced metal-insulator transition to an orthorhombic phase across  $T_N \sim 280$  K.

*Semiconductor to semiconductor.* In the above mentioned work of Tsuchiya *et al.* [117], the non-stoichiometric films did not show a MPT. The resistivity decreases monotonically with temperature suggesting a semiconducting (hopping-like) behavior of the samples. CrN powder samples synthesized by Herle *et al.*[119] show a transition from a PM to an AFM phase at 280 K. Activated semiconducting behavior with a band gap of 0.09 eV was obtained from resistivity vs.  $T$  curves. Quintela *et al.* [111] studied polycrystalline samples of  $\text{Cr}_{1-x}\text{V}_x\text{N}$ . Stoichiometric CrN shows a MPT at  $T_N \sim 286$  K and semiconducting behavior in the whole  $T$ -range. Above  $T_N$ , the resistivity vs.  $T$  curve shows activated semiconducting behavior with a band gap of 150 meV. Below the transition, the changes in the chemical bond linked to the AFM order, give as a result a non-activated semiconducting behavior. The thermoelectric power of stoichiometric CrN shows a linear  $T$ -dependence as expected for metals or highly degenerate semiconductors. This supports the idea of an electronic state neither thermally activated nor fully itinerant in the AFM phase. Further evidence of this idea is given by the drastic reduction of the bulk modulus due to the bond softening and charge delocalization into the shorter and less strong Cr-Cr bonds in the AFM phase [23]. By ultrahigh vacuum magnetron sputtering, Gall *et al.* [107, 109, 115, 116, 120] grew single crystalline CrN (001)

films on a MgO(001) substrate. The absence of any discontinuity in the resistivity vs.  $T$  curves suggests that epitaxial constraints suppress the transition to an AFM phase with the film being cubic and PM at all  $T$ . The resistivity decreases with increasing temperature indicating semiconducting behavior over the whole  $T$ -range. From optical absorption measurements, an optical band gap of 0.7 eV was obtained [107, 112]. An indirect band gap of about 0.19 eV was also estimated [120] from optical measurements suggesting CrN is a Mott-Hubbard-type insulator. In addition, the samples show semiconducting behavior in a variable range hopping regime below 120 K [109, 116].

The importance of the N vacancy-concentration as well as the substrate and associated grain boundaries has been recently shown in an experimental work by Duan *et al.* [121]. Polycrystalline  $\text{CrN}_x$  films on Si(100) and glass substrates as well as epitaxial  $\text{CrN}_x$  films on MgO(100) have been grown by reactive sputtering with different N gas flow rates ( $f_{N_2}$ ). Both in epitaxial and polycrystalline films there is a transformation of conductance from metallic to semiconducting as  $f_{N_2}$  is increased. Only the polycrystalline films prepared at  $f_{N_2} = 30$  and 50 sccm show a discontinuity in  $\rho(T)$  curves at 260-280 K. While for  $f_{N_2} = 30$  sccm the film shows a metal-insulator-like transition, for  $f_{N_2} = 50$  sccm the resistivity shows a steep decrease with decreasing temperature in the range 260-280 K and increases with decreasing temperature below 145 K. The transition is absent in all the  $\text{CrN}_x$  epitaxial films.

As can be seen, there is a big discussion and disagreement between different experimental works. There are also some theoretical studies on CrN. Calculations within the local density approximation (LDA) have been performed on CrN by Filippetti *et al.* [105, 106]. For the distorted orthorhombic structure, they found as ground state the experimentally observed AFM2 configuration. For the cubic structure, the ground state is the so-called AFM1, similar to the AFM2, but with the spins antialigned every layer instead of every two layers (left panel of Fig. 3.1). This can be understood in terms of the magnetic stress: the AFM2 phase is under more stress with respect to the AFM1. This

is due to the spin ordering asymmetry of the AFM2 phase on the (001) plane where each Cr has two spin-antiparallel and two spin-parallel nearest neighbors. Considering that bonds between the antiferromagnetically coupled neighbors are under tensile stress, while bonds between ferromagnetically coupled atoms are under compressive stress, in the AFM2 magnetic configuration, stress can be relieved by an orthorhombic distortion. In the AFM1 structure, it cannot be relieved because all the four nearest neighbors are FM coupled. Hence, in order to relieve stress and reduce the total energy, the system undergoes a shear distortion from cubic to orthorhombic. LDA calculations show a metallic behavior for both AFM phases (weak metal since the density of states (DOS) at the Fermi level is small). From studies of TM oxides and other correlated compounds it is known that LDA underestimates the Coulomb effects on the narrow  $d$  bands, predicting an unrealistic metallic state in systems that actually have a band gap, as we saw in Chapter 1. Hence, further electronic structure calculations in CrN within the LDA+ $U$  method were performed by Herwadkar *et al.* [122]. If the on-site Coulomb repulsion ( $U$ ) is considered, a band gap already opens for a value of  $U = 3$  eV in the magnetic ground state, suggesting that CrN may be close to being a charge-transfer insulator.

To shed light on the existing controversies about CrN, we will analyze in this Chapter the results of *ab initio* calculations performed using different computational schemes to treat the moderately correlated  $d$  electrons of CrN and describe properly its electronic structure and transport properties [123].

## 3.2 Computational details

As mentioned in the Introduction, most of the DFT-based calculations in solids have been done using two (semi)local approaches for the exchange-correlation energy and potential: local density approximation (LDA) or generalized gradient approximation (GGA). Although they give useful total energies and structural parameters, both of them



are known to underestimate the band gap of most semiconductors and insulators.

As explained in Section 1.4.5 there are several functionals that can provide more accurate values for band gaps. On the one hand, staying inside the true Kohn-Sham (KS) framework (multiplicative potential), the newly developed semilocal potentials (such as the one developed by Tran and Blaha based on a modification of the Becke-Johnson potential, from hereon TB-mBJLDA) can give good results [56, 57]. But on the other hand, nonmultiplicative potentials can also be used. These methods belong to the so-called generalized KS framework [60] and most of them mix DFT and Hartree-Fock (HF) theories. The most used ones are the LDA+ $U$  approach and hybrid methods [124].

In order to analyze the electronic structure of the compound, we have performed calculations with all these methods: PBE (which is of the GGA form), LDA+ $U$  with several values of  $U$  (2-5 eV), TB-mBJLDA, and hybrid functionals (screened and unscreened).

As extensively described in the Introduction, the LDA+ $U$  scheme improves over GGA or LDA in the study of systems containing correlated electrons by introducing the on-site Coulomb repulsion  $U$  applied to localized electrons (e.g  $3d$  or  $4f$ ). We have performed calculations on CrN within the LDA+ $U$  method taking  $U$  in a reasonable range for this type of  $3d$  electron systems (from 2 to 5 eV) comparable to the values obtained by PES experiments. The exchange parameter  $J$  in this case was set to zero.

In hybrid methods a certain amount of semilocal exchange is replaced by HF exchange with the correlation remaining purely semilocal. They usually lead to improved band structures in good agreement with experiments as shown for several semiconductors and insulators or even strongly correlated electron systems [125–127]. We have applied one of the most common hybrid functionals (PBE0)[128, 129] to the study of the electronic structure of CrN. However, traditional hybrid functionals are computationally very demanding due to the long-range nature of the HF exchange in solids. A way to reduce this problem

of convergence is to consider only the short-range part of the HF exchange as proposed by Bylander and Kleinman [130]. This scheme has been used by Heyd, Scuseria, and Ernzerhof [131, 132] who proposed a screened hybrid functional based on PBE0. We have also performed calculations using a screened hybrid functional as implemented in the WIEN2k code with the HF exchange screened by means of the Yukawa potential (so called, YS-PBE0) [71].

The calculations were done with  $R_{MT}K_{max} = 7$ . The chosen  $R_{MT}$  were 2.06 and 1.82 for Cr and N, respectively. The PBE, LDA+ $U$ , and TB-mBJLDA calculations were done with a  $7 \times 13 \times 9$  k-mesh for the integrations over the Brillouin zone. Since calculations with hybrid functionals are much more costly, a less dense k-mesh of  $4 \times 8 \times 6$  was used for the YS-PBE0 and PBE0 functionals. Convergence for the total energies presented is achieved with that k-mesh. The transport properties are very sensitive to the Brillouin zone sampling, therefore an even denser grid ( $19 \times 37 \times 27$ ) was used to obtain convergence.

### 3.2.1 Structure

As mentioned in Section 3.1, the transition at  $T_N$  in CrN from the PM to the AFM phase is accompanied by a distortion of the rocksalt structure. The shear distortion consists of a contraction of the angle from the cubic ( $90^\circ$ ) to  $88.23^\circ$  (see [105] for a more detailed description). Calculations were done both, with and without distortion at the experimental lattice constants [104]. In order to accommodate the AFM2 phase, a unit cell comprising four formula units has been used. The calculations for the other magnetic phases were also performed with this unit cell.

## 3.3 Results

A crude estimate of the possible electronic configuration of CrN can be obtained from an ionic model since it is a moderately correlated

transition-metal nitride. Taking the usual valency for N, the average valence for the octahedrally coordinated Cr is +3. In a high-spin state ( $S = 3/2$ , magnetic moment of  $3 \mu_B$ ), the threefold-degenerate majority-spin channel  $t_{2g}^\uparrow$  is completely filled while the minority  $t_{2g}^\downarrow$  remains empty with the  $e_g$  states for both spin channels also completely empty above the Fermi level. This electronic configuration can be observed in Fig. 3.1. Depending on the balance between crystal-field splitting ( $\Delta_{CF}$ ) and Hund's rule coupling strength ( $J_H$ ), the first unoccupied bands could be  $e_g^\uparrow$  ( $J_H > \Delta_{CF}$ ) or  $t_{2g}^\downarrow$  ( $J_H < \Delta_{CF}$ ). Significant contribution of the N  $p$  bands below the Fermi level is expected due to hybridization of these states with the Cr  $d$  bands.

Tables 3.1 and 3.2 show the relative energies, band gaps, and magnetic moment on the Cr cation obtained for the AFM1, AFM2, FM and non-magnetic (NM) configurations calculated with the various exchange-correlation potentials explained above.

Looking at Tables 3.1 and 3.2, it can be seen that the orthorhombic AFM2 phase is favored overall, independent on the functional. For the cubic phase, this magnetic arrangement is also the more favored for the LDA+ $U$  and hybrid functionals. The other phases are clearly less stable. For instance, with LDA+ $U$  AFM1 is disfavored by 35-41 meV/-formula unit, FM by 146-209 meV/formula unit, and NM by 1074-2456 meV/ formula unit. Hybrid functionals retain the relative energies between the AFM2 and AFM1 phases and make the FM phase even more unstable with respect to the ground state AFM2. It has to be remarked that for PBE within the cubic phase (as it occurred with LDA in the calculations carried out by Filippetti *et al.*[105, 106]), the AFM1 phase is more favored than the AFM2 although by just 4 meV/formula unit. An important point to note is that if the AFM1 is kept, no orthorhombic distortion would be predicted, independently of the functional used (i.e., the cubic AFM1 phase is always more stable than the orthorhombic AFM1 one). This is a consequence of the magnetostriction/stress relief issues described above and already found by Filippetti *et al.* using LDA [105, 106].

**Table 3.1:**

Relative energy (in meV/formula unit), band gap (in eV), and Cr atomic moment (in  $\mu_B$ ) of CrN for the different methods used in this work for the orthorhombic phase. It was not possible to converge the calculations with the hybrid functionals for the metallic NM phase.

	orthorhombic			
	AFM2	AFM1	FM	NM
Relative energy				
PBE	0	20	211	504
LDA+ $U$ ( $U_{\text{eff}} = 2$ eV)	0	42	215	1068
LDA+ $U$ ( $U_{\text{eff}} = 3$ eV)	0	49	202	1540
LDA+ $U$ ( $U_{\text{eff}} = 4$ eV)	0	50	180	2028
LDA+ $U$ ( $U_{\text{eff}} = 5$ eV)	0	51	156	2405
YS-PBE0 ( $\alpha = 0.1$ )	0	34	270	
PBE0 ( $\alpha = 0.1$ )	0	36	279	
YS-PBE0 ( $\alpha = 0.25$ )	0	34	232	
PBE0 ( $\alpha = 0.25$ )	0	35	229	
Band gap				
PBE	0	0	0	0
LDA+ $U$ ( $U_{\text{eff}} = 2$ eV)	0	0	0	0
LDA+ $U$ ( $U_{\text{eff}} = 3$ eV)	0.30	0	0	0
LDA+ $U$ ( $U_{\text{eff}} = 4$ eV)	0.68	0.17	0	0
LDA+ $U$ ( $U_{\text{eff}} = 5$ eV)	0.91	0.51	0	0
TB-mBJLDA	0.79	0.22	0	0
YS-PBE0 ( $\alpha = 0.1$ )	0.20	0	0	0
PBE0 ( $\alpha = 0.1$ )	0.48	0	0	0
YS-PBE0 ( $\alpha = 0.25$ )	1.45	0.84	0	0
PBE0 ( $\alpha = 0.25$ )	2.13	1.53	0.43	0
Cr spin magnetic moment				
PBE	2.32	2.23	2.28	0
LDA+ $U$ ( $U_{\text{eff}} = 2$ eV)	2.51	2.43	2.61	0
LDA+ $U$ ( $U_{\text{eff}} = 3$ eV)	2.59	2.52	2.70	0
LDA+ $U$ ( $U_{\text{eff}} = 4$ eV)	2.65	2.58	2.74	0
LDA+ $U$ ( $U_{\text{eff}} = 5$ eV)	2.69	2.62	2.76	0
TB-mBJLDA	2.52	2.48	2.64	0
YS-PBE0 ( $\alpha = 0.1$ )	2.49	2.42	2.62	0
PBE0 ( $\alpha = 0.1$ )	2.49	2.42	2.64	0
YS-PBE0 ( $\alpha = 0.25$ )	2.59	2.54	2.67	0
PBE0 ( $\alpha = 0.25$ )	2.59	2.54	2.67	0

**Table 3.2:**

Relative energy (in meV/formula unit), band gap (in eV), and Cr atomic moment (in  $\mu_B$ ) of CrN for the different methods used in this work for the cubic phase. It was not possible to converge the calculations with the hybrid functionals for the metallic NM phase.

	cubic			
	AFM2	AFM1	FM	NM
Relative energy				
PBE	17	13	208	507
LDA+ $U$ ( $U_{\text{eff}} = 2$ eV)	14	35	209	1074
LDA+ $U$ ( $U_{\text{eff}} = 3$ eV)	11	41	194	1548
LDA+ $U$ ( $U_{\text{eff}} = 4$ eV)	8	41	170	2049
LDA+ $U$ ( $U_{\text{eff}} = 5$ eV)	5	41	146	2456
YS-PBE0 ( $\alpha = 0.1$ )	12	25	261	
PBE0 ( $\alpha = 0.1$ )	12	26	270	
YS-PBE0 ( $\alpha = 0.25$ )	7	23	220	
PBE0 ( $\alpha = 0.25$ )	7	24	218	
Band gap				
PBE	0	0	0	0
LDA+ $U$ ( $U_{\text{eff}} = 2$ eV)	0	0	0	0
LDA+ $U$ ( $U_{\text{eff}} = 3$ eV)	0.30	0	0	0
LDA+ $U$ ( $U_{\text{eff}} = 4$ eV)	0.66	0.20	0	0
LDA+ $U$ ( $U_{\text{eff}} = 5$ eV)	0.89	0.56	0	0
TB-mBJLDA	0.80	0.27	0	0
YS-PBE0 ( $\alpha = 0.1$ )	0.20	0	0	
PBE0 ( $\alpha = 0.1$ )	0.47	0	0	
YS-PBE0 ( $\alpha = 0.25$ )	1.44	0.95	0	
PBE0 ( $\alpha = 0.25$ )	2.11	1.66	0.47	
Cr spin magnetic moment				
PBE	2.33	2.23	2.30	0
LDA+ $U$ ( $U_{\text{eff}} = 2$ eV)	2.51	2.43	2.61	0
LDA+ $U$ ( $U_{\text{eff}} = 3$ eV)	2.59	2.52	2.70	0
LDA+ $U$ ( $U_{\text{eff}} = 4$ eV)	2.65	2.58	2.74	0
LDA+ $U$ ( $U_{\text{eff}} = 5$ eV)	2.69	2.62	2.76	0
TB-mBJLDA	2.52	2.49	2.64	0
YS-PBE0 ( $\alpha = 0.1$ )	2.49	2.42	2.63	
PBE0 ( $\alpha = 0.1$ )	2.50	2.43	2.65	
YS-PBE0 ( $\alpha = 0.25$ )	2.59	2.54	2.67	
PBE0 ( $\alpha = 0.25$ )	2.60	2.54	2.67	

Concerning the band gap values, both the NM and FM configurations remain metallic for all the functionals except PBE0 with  $\alpha = 0.25$ , which gives a band gap around 0.45 eV for the FM case. In LDA+ $U$  calculations with  $U = 3$  eV (both for cubic -undistorted- and orthorhombic -distorted- structures), a gap of 0.3 eV already opens for the AFM2 configuration while the AFM1 remains metallic for this particular value of  $U$  (a gap of about 0.2 eV opens for the AFM1 ordering at  $U = 4$  eV). If the value of  $U$  is increased up to 5 eV, the value of the band gap is 0.9 eV for the AFM2 configuration and about 0.5 eV for AFM1. Hence, from LDA+ $U$  calculations it can be concluded that the opening of a band gap is easier for the AFM2 (ground state) phase. The same conclusions can be drawn from the TB-mBJLDA calculations: both AFM configurations are insulating with values of the band gap similar to those obtained within LDA+ $U$  for  $U = 4$  eV (0.79 and 0.22 eV for the AFM2 and AFM1 distorted structure, respectively). For hybrid functionals, the values of the band gap are very dependent on the amount of HF exchange ( $\alpha$ ) and on whether it is screened or not. For  $\alpha = 0.25$ , PBE0 gives a band gap for the AFM2 distorted phase of about 2.1 eV and of 1.5 eV for AFM1, whereas the screened YS-PBE0 gives much lower values of the band gap (1.45 eV for AFM2 and 0.84 eV for AFM1). Furthermore, the reduction of  $\alpha$  to 0.1, leads to a huge reduction of the gap values, making the AFM1 phase metallic and reducing significantly the AFM2 band gap.

Concerning the magnetic moments of Cr ions, the values for LDA+ $U$  are in between the reported experimental values of  $2.36 \mu_B$  [104] and  $3.17 \mu_B$  [133] and increase with  $U$ . They change from 2.51 to  $2.69 \mu_B$  for the AFM2 configuration and from 2.43 to  $2.62 \mu_B$  for the AFM1 when varying  $U$  from 2 to 5 eV. Slightly larger values are obtained for the FM phase (from 2.61 to  $2.76 \mu_B$ ), reaching values close to the atomic limit for a  $d^3$  cation in the high-spin state. This increase is due to the reduction of the  $p$ - $d$  hybridization caused by  $U$ . For TB-mBJLDA, the magnetic moments are close to the values obtained from LDA+ $U$  with low values of  $U = 2$ -3 eV. Hybrid functionals (both screened and

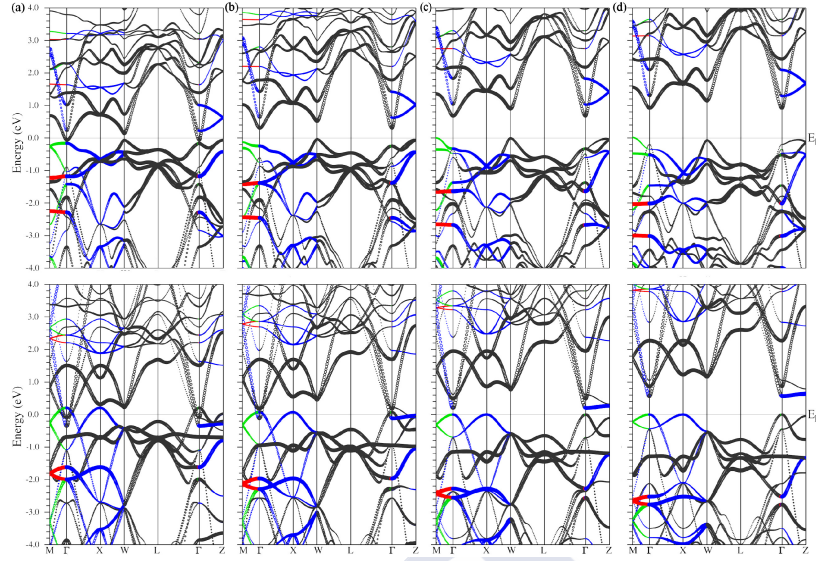


**Figure 3.2:**

Band structures with band character plot (Cr  $d$  highlighted) of the orthorhombic AFM2 phase (upper panels) and cubic AFM1 (lower panels) of CrN obtained from the LDA+ $U$  method with (a)  $U = 2$  eV, (b)  $U = 3$  eV, (c)  $U = 4$  eV, and (d)  $U = 5$  eV. The colors indicate the irreducible representation of the eigenvalues.

unscreened) give magnetic moments which are slightly larger (smaller) than TB-mBJLDA for  $\alpha = 0.25$  ( $\alpha = 0.1$ ).

Below, a more detailed discussion of the electronic structure is given for each functional separately.

### 3.3.1 LDA+ $U$ electronic structure analysis

The evolution of the band structure with the  $U$  value for both the cubic AFM1 and orthorhombic AFM2 phases can be seen in Fig. 3.2. We use an orthorhombic Brillouin zone in all cases and the following  $k$ -path:  $M(\pi/a, 0, 0)$ - $\Gamma(0, 0, 0)$ - $X(0, \pi/b, 0)$ - $W(\pi/a, 3\pi/2b, 0)$ - $L(0, \pi/b, \pi/c)$ - $\Gamma$ - $Z(0, 0, \pi/c)$ . In Fig. 3.3, the density of states (DOS) for the orthorhombic AFM2 phase (for  $U = 4$  eV) is also shown.

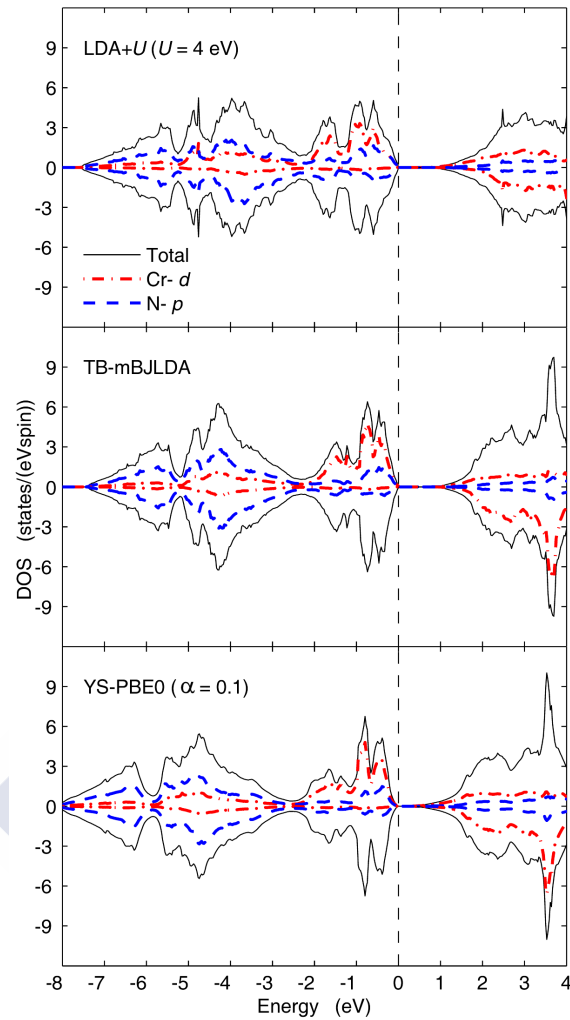
For both magnetic configurations, the rough ionic electronic structure described above for the majority spin state of Cr atoms can be easily distinguished: the  $t_{2g}^\uparrow$  manifold is filled (in the range between  $-2$  and  $0$  eV below the Fermi energy), while only a small amount of (bonding)  $e_g$  levels (in the range between  $-6$  and  $-3$  eV and hybridizing with the N  $p$  orbitals) are occupied. As can be seen in Fig. 3.3, the band gap character is clearly  $d-d$  ( $t_{2g}^\uparrow-e_g^\uparrow$ ) although some rather small contribution of N  $p$  states is also observed. Hence, CrN can be better described as a Mott-Hubbard insulator than as a charge-transfer insulator [134].

For the AFM2 configuration (upper panels of Fig. 3.2), it can be seen how for the lowest  $U$  value, the band structure remains metallic with a gap opening already for  $U = 3$  eV. The unoccupied bands move up gradually as  $U$  increases. This is particularly noticeable for the first unoccupied band at  $\Gamma$  for  $U = 2$  eV and also the one that forms the small electron pocket. Also, as  $U$  increases, the bands right below the Fermi level move down in energy. For larger  $U$ , the Cr  $d$  character near  $M$  is reduced since the Cr  $t_{2g}^\uparrow$  states are shifted down in energy. The splitting between the first two bands right below the Fermi energy decreases at  $\Gamma$  with increasing  $U$ , increases at  $M$  and  $W$  causing in principle a displacement of the top of the valence band from  $W$  for lower  $U$  values to  $M$  for higher ones (for  $U = 4$  eV, almost the same eigenvalue is obtained at  $M$  and  $W$ ). Some features of the band structure are  $U$ -independent: the conduction band minimum is always at  $\Gamma$  and the existence of degenerate bands at  $L$  which is not accidental but symmetry required.

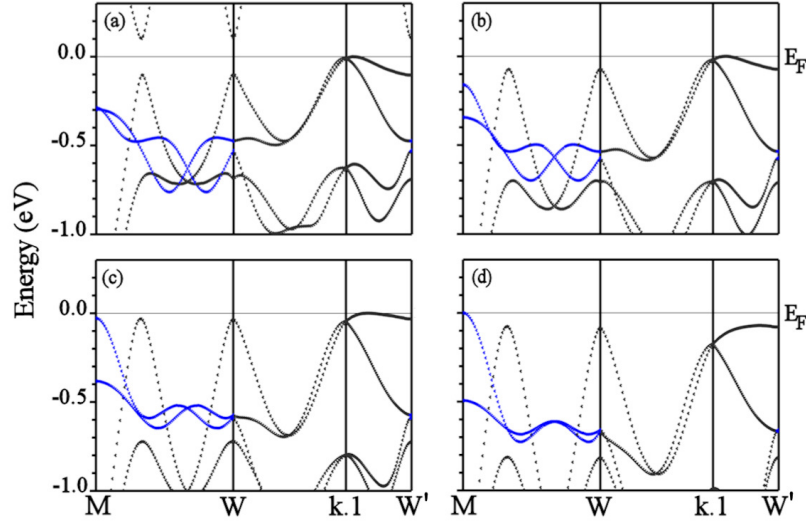
Another observation that can be made by looking at the changes in the DOS, is a decrease of the distance between the main peaks of the occupied Cr  $t_{2g}$  and N- $p$  bands. For  $U = 2$  eV, the distance is approximately 4 eV, while for  $U = 5$  eV it is reduced to about 2.5 eV.

Previous band structure calculations [122] reported that when the gap first opens at low  $U$ , the top of the valence band (VBM) is at  $W$  moving to  $M$  as  $U$  increases. Figure 3.4 shows the LDA+ $U$  band



**Figure 3.3:**

Density of states of CrN (orthorhombic AFM2 phase) calculated with different methods. The Fermi energy is set at  $E = 0$  eV. The positive and negative values on the  $y$ -axis are for spin-up and spin-down, respectively.

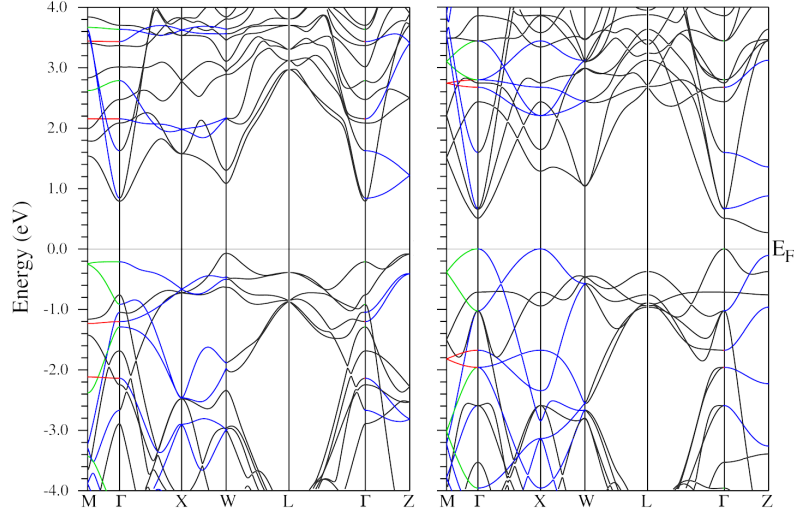


**Figure 3.4:**

Band structures blown-up around  $E_F$  for the orthorhombic AFM2 phase within LDA+ $U$  [(a)  $U = 2$  eV, (b)  $U = 3$  eV, (c)  $U = 4$  eV, and (d)  $U = 5$  eV] in a special  $k$ -path showing the displacement of the VBM with the  $U$  value. The colors indicate the irreducible representation of the eigenvalues.

structure along the path  $M (\pi/a, 0, 0)$ - $W (\pi/a, 3\pi/2b, 0)$ - $k.1 (\pi/a, 3\pi/2b, \pi/c)$ - $W' (\pi/a, \pi/2b, 0)$ . Our calculations show that when the gap opens (at  $U \sim 3$  eV), the VBM is not at  $W$  but displaced to a non-high symmetry point in the direction from  $k.1$  to  $W'$ , and then moving to  $M$  at  $U = 5$  eV.

For the cubic AFM1 phase, a small gap of 0.20 eV is opened for  $U = 4$  eV becoming 0.56 eV for  $U = 5$  eV. We can see this evolution in the lower panels of Fig. 3.2. In addition, numerous degenerate bands can be seen at  $M$  and  $W$  (with these degeneracies clearly lifted in the orthorhombic AFM2 phase).

**Figure 3.5:**

Band structures with TB-mBJLDA for the orthorhombic AFM2 (left panel) and cubic AFM1 (right panel) phase. The colors indicate the irreducible representation of the eigenvalues.

### 3.3.2 TB-mBJLDA electronic structure analysis

As mentioned above, the band gap values obtained for TB-mBJLDA are rather similar to those obtained from LDA+ $U$  with  $U = 4$  eV (Bhobe *et al.*[113] determined an experimental value of  $U$  of about 4.5 eV by PES).

For the cubic AFM1 configuration, the band structure plot is shown in Fig. 3.5 (right panel). Below the Fermi level it is fairly different from the one obtained within LDA+ $U$  (with low  $U$ ). In addition, the first band above the Fermi level at  $\Gamma$  in LDA+ $U$  calculations lies lower in energy than with TB-mBJLDA, but it is not just a rigid band shift, some differences are noticeable particularly around the  $\Gamma$  point. Actually, the bottom of the conduction band in TB-mBJLDA is no longer at  $\Gamma$  but displaced to  $Z$ . In addition, the band gap character changes from LDA+ $U$  results being in this case a  $t_{2g}^{\uparrow}-t_{2g}^{\downarrow}$  band gap.

For the orthorhombic AFM2 phase, the splitting at  $\Gamma$  between the first two bands above the Fermi level is reduced in TB-mBJLDA (see left panel of Fig. 3.5). The band structure obtained below the Fermi energy is very similar to the one obtained from LDA+ $U$  with  $U = 2$  eV. In addition, as for LDA+ $U$  calculations with the values of  $U$  3 to 4 eV, the VBM is not at  $W$  but displaced to a non-high symmetry point in the direction  $k_1 - W'$ . In Fig. 3.3 we can compare the DOS calculated from LDA+ $U$  and TB-mBJLDA. We can see that the N  $p$  character in the Cr  $t_{2g}^\uparrow$  band (from  $-2.5$  to  $0$  eV) is smaller in TB-mBJLDA than in LDA+ $U$  (and the opposite is true for the Cr  $e_g^\uparrow$  character in the N  $p$  bands below  $-3$  eV). This effect has to do with the different hybridizations obtained with the two schemes (enhanced with the LDA+ $U$  method). In addition, the separation of N  $p$  and Cr  $t_{2g}^\uparrow$  bands is larger in TB-mBJLDA, although the total valence band width is almost the same ( $\sim 7.5$  eV)

The optical transmission and reflection spectra of CrN are shown in [112]. A band-gap-like optical transmission feature is found at  $0.7$  eV suggesting that CrN is a semiconductor with an indirect gap of approximately  $0.7$  eV and a  $\Gamma$ -valley gap greater than  $0.7$  eV. The values of the band gap (indirect) obtained from LDA+ $U$  ( $U = 4$  eV) and TB-mBJLDA calculations for the AFM2 phase are very close to this  $0.7$  eV value ( $0.68$  eV and  $0.79$  eV, respectively). A gap at  $\Gamma$  of about  $1$  eV ( $> 0.7$  eV) is also found in our calculations.

Thus, TB-mBJLDA is able to reproduce some of the effects on the electronic structure caused by the on-site Coulomb repulsion between Cr  $d$  electrons without using a tunable parameter and being consistent with the results found for bulk CrN stoichiometric samples.

### 3.3.3 Hybrid functionals electronic structure analysis

As can be seen from Tables 3.1 and 3.2, the results with hybrid functionals strongly depend on the amount of HF exchange  $\alpha$ . If we take as

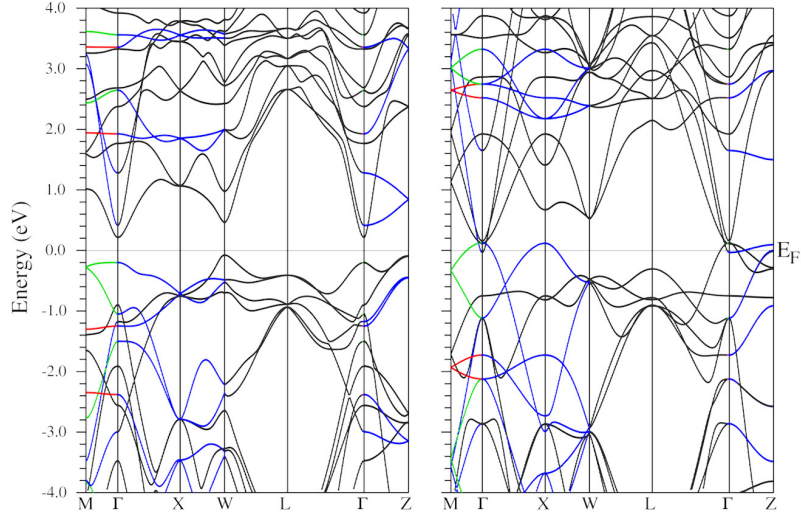


**Figure 3.6:**

Band structures with YS-PBE0 ( $\alpha = 0.1$ ) for the orthorhombic AFM2 (left panel, insulating) and cubic AFM1 phase (right panel, metallic). The colors indicate the irreducible representation of the eigenvalues.

a reference the values obtained within TB-mBJLDA (similar to those from LDA+ $U$  with  $U = 4$  eV), using  $\alpha = 0.1$  gives closer results than using  $\alpha = 0.25$ . The band structure for the cubic AFM1 and orthorhombic AFM2 phase are shown in Fig. 3.6 for the screened YS-PBE0 functional with  $\alpha = 0.1$ .

For the ground state orthorhombic AFM2 phase, there is a reduction of the band gap with respect to LDA+ $U$  or TB-mBJLDA (as a consequence of the reduction of  $\alpha$ ) to 0.2 eV. The band structures retain the same features that we discussed above for LDA+ $U$  or TB-mBJLDA. In particular, the VBM is also not at  $W$ , but displaced to a non-high symmetry point (see Fig. 3.4 for LDA+ $U$ ). Above the Fermi level, the splittings between the bands show more similarities with those obtained from LDA+ $U$  with  $U = 4$  eV. Figure 3.3 shows that the shape of the DOS is very similar to the TB-mBJLDA DOS, but the total valence

band width is increased to about 8.2 eV. The same trend can be observed for the AFM1 phase: the band structure below the Fermi energy is more similar to the one obtained with TB-mBJLDA and above to that obtained with LDA+ $U$ .

Hence, hybrid functionals can also describe accurately the electronic structure of CrN, but by tuning the amount of HF exact exchange. Although results and tunability with hybrid functionals are comparable with LDA+ $U$ , this last method allows an easier physical description of the tuning parameter  $U$  and is computationally less expensive.

### 3.4 Discussion

As can be seen from the values of the band gap in Tables 3.1 and 3.2, the tendency towards a band gap opening is strongest for the AFM2 ground state phase (for LDA+ $U$  with  $U$  as low as 3 eV, TB-mBJLDA, and hybrid functionals). Although more difficult, it is also possible to open a gap in the other AFM ordering (AFM1).

As mentioned in Section 3.1, the intrinsic mechanism of electronic transport in CrN is a controversial issue. Most of the discrepancies in experimental works appear among those where the properties of thin films (where by epitaxial constraints even the phase transition can be suppressed) have been measured. Hence, we will focus in the couple of works where bulk polycrystalline samples have been studied to reconcile our results with previous data [111, 113].

In the work by Quintela *et al.* [111] the resistivity of  $\text{Cr}_{1-x}\text{V}_x\text{N}$  has been measured. Negative temperature coefficient of resistivity ( $\text{TCR} = d\rho/dT$ ), typical for semiconducting behavior, was observed for samples with V doping  $x \leq 0.1$ . For  $x \geq 0.2$  the system shows a positive TCR pointing to an itinerant electron behavior. Stoichiometric CrN exhibits  $\text{TCR} < 0$  (nonitinerant) over the whole  $T$ -range although only for  $T > T_N$  the behavior can be fit to that of an activated semiconductor with a value of the activation energy of 75 meV. In the low-temperature AFM orthorhombic phase, the mechanism of electronic transport is not

fully understood: neither a simple thermal activation nor a variable range hopping behavior describe the resistivity below  $T_N$ . In a system with a charge gap, given the exponential dependence of  $\rho(T)$  with  $T$ ,  $d(\ln \sigma)/d(\ln T)$  should diverge as  $T \rightarrow 0$ . However, for CrN, it goes to zero as  $T \rightarrow 0$ . Hence, despite the negative TCR, CrN cannot be classified as a typical thermally activated semiconductor. The different semiconducting behavior in the low- $T$  phase was ascribed to the changes in chemical bond linked to the AFM order. Deriving the same result for stoichiometric CrN, Bhoje *et al.* [113] concluded that the low- $T$  phase of CrN is one of the rare examples of AFM-itinerant (metallic) systems in spite of the negative TCR. Back to [111], for  $x = 0.1$  in the  $\text{Cr}_{1-x}\text{V}_x\text{N}$  series, there is a sudden change in the sign of TCR at the Néel temperature:  $\text{TCR} > 0$  (itinerant) for the high- $T$  PM phase and  $\text{TCR} < 0$  (nonitinerant) for the low- $T$  AFM phase. Hence, it seems that for  $T < T_N$ , the opening of a charge gap at the magnetic ordering temperature increases the activation energy, recovering semiconducting like behavior below  $T_N$ .

The fact that the opening of a charge gap is intrinsic to the ground-state AFM ordering is consistent with our calculations. We show that the onset of magnetism should be accompanied of a gap opening. The behavior of the transport properties in the PM phase is beyond the scope of this work, but our calculations can conclude that the AFM phase is always insulating and, if it is not, then it has to do with issues caused by nanostructuring such as non-stoichiometries, strain, surface effects, etc. In a system situated close to a metal-insulator transition, small changes can induce a transition from localized to itinerant behavior, but this is not reachable in bulk-stoichiometric CrN in the magnetic phase, as our calculations show.

Further evidence of the existence of an unconventional electronic state in the AFM phase of CrN, not thermally activated neither fully

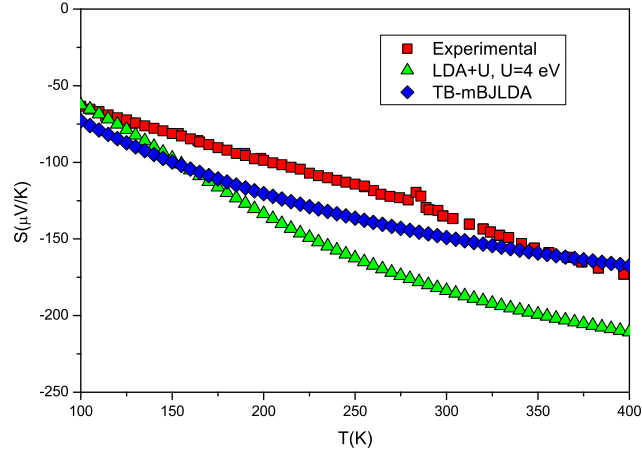


**Figure 3.7:**

Experimental [111] and calculated temperature dependence of the thermopower. The results for both TB-mBJLDA and LDA+ $U$  ( $U = 4$  eV) are shown.

itinerant, was observed comparing the behavior of the electrical resistivity with the thermoelectric power measurements [111]. For stoichiometric CrN, the thermoelectric power shows linear temperature dependence (typical for metals or highly degenerate semiconductors). In addition, no discontinuity is observed at  $x = 0.2$ , where TCR changed from negative to positive at low temperatures.

In order to check if the experimental behavior of the thermoelectric power can be reproduced from our calculations, we have obtained its dependence with temperature in the magnetic ground state (AFM2) for LDA+ $U$  ( $U = 4$  eV) and TB-mBJLDA calculations.

For the sake of comparison, we present the calculations together with the experimental values of the Seebeck coefficient taken from [111] (see Fig. 3.7). The results for the AFM2 phase fit the experimental values rather well, particularly using the TB-mBJLDA scheme, both in order of magnitude of the thermopower and also on the observed evolution with temperature ( $dS/dT < 0$ ) (although the behavior found from the calculations is not as linear as obtained experimentally).



Hence, our thermopower calculations confirm that stoichiometric CrN in the magnetic phase is semiconducting, but close to a transition from localized to itinerant electronic behavior.

### 3.5 Summary and conclusions

We have performed electronic structure calculations for CrN using a diverse set of exchange-correlation potentials: PBE, LDA+ $U$ , the semilocal functional developed by Tran and Blaha based on a modification of the Becke Johnson potential, and hybrid functionals both in screened (YS-PBE0) and unscreened (PBE0) modes.

In any case, our calculations show that the onset of magnetism in CrN should be accompanied of a gap opening. We can conclude that the AFM phase is always insulating in agreement with experiments in stoichiometric bulk samples. The different metallic behavior found in various thin films most likely has to do with nanostructuring that could include vacancies, strain, surface effects, etc. In a system situated so close to the itinerant boundary, small changes can yield metallicity and even the suppression of the magnetic transition (which we have seen from our calculations it is strongly dependent on the structural details). The behavior obtained for the thermoelectric power confirms that stoichiometric CrN in the magnetic phase is semiconducting, but close to the transition from localized to itinerant behavior. The solution we found as ground state can describe accurately the transport properties of the system.

In addition, our results give further evidence that the TB-mBJLDA functional is very useful for treating the electronic structure of correlated semiconductors giving almost the same band gaps as obtained from LDA+ $U$  with  $U = 4$  eV (close to the one determined experimentally) for different magnetic configurations allowing a parameter free description of the system. Hybrid functionals are also well capable of describing the electronic structure of CrN by tuning the amount of HF exact exchange. However, results and tunability are comparable

with LDA+ $U$ , that allows an easier physical description of the tuning parameter  $U$ .



## **Sr<sub>6</sub>Co<sub>5</sub>O<sub>15</sub>: non-one-dimensional behavior of a charge ordered structurally quasi-one-dimensional oxide**

“

*It is a good morning exercise for a research scientist to discard a pet hypothesis every day before breakfast. It keeps him young.*

*[Konrad Lorenz]*

”

### **4.1 Background**

We have seen for CrN that the agreement between the calculated and experimental values of the thermopower can lead us to the confirmation of the magnetic ground state. We saw how, through the understanding of the thermopower of a material, we could also understand important features of its electronic structure. Back in the 1960s John M. Ziman, already pointed out in his book *Electrons and Phonons* that the most sensitive electronic transport property of a metal is its thermopower so the fact that its behavior can be useful to understand features of

the electronic structure of a material is nothing new. In this Chapter, we will use again the analysis of the thermoelectric power behavior as a tool to further understand the electronic properties of a different material, the cobaltate  $Sr_6Co_5O_{15}$ , a member of the the homologous series  $A_{n+2}B'B_nO_{3n+3}$  [135–137] (A alkaline or alkaline earth cations, B' and B commonly corresponding to Co cations in a trigonal prismatic and octahedral position, respectively, and  $n \in [1, \infty)$ ). This series has focused particular interest for the one-dimensional behavior that most of its members exhibit with the one-dimensional chain being represented by  $B'B_nO_{3n+3}$ . One-dimensional (1D) systems are key to elaborate models for strongly correlated electron materials, since they are the easiest to study because all the interesting phenomena take place along one direction.

In particular, both the end members of the series ( $Ca_3Co_2O_6$  ( $n=1$ ) and  $BaCoO_3$  ( $n=\infty$ )) have focused much attention for the past years. The  $n=1$  compound ( $Ca_3Co_2O_6$ ) has been analyzed in several previous works [135, 138–144]. The valence state of Co ions in this case is assigned to be  $3+$  ( $d^6$ ), with low-spin state for Co ions in the  $CoO_6$  octahedron ( $S=0$ ) and high-spin state within the trigonal prism ( $S=2$ ). This compound shows a paramagnetic behavior at high temperature. In-chain ferromagnetic (FM) interactions arise below 80 K, reaching 1D FM order at 30 K. Below this temperature, interchain two-dimensional (2D) antiferromagnetic (AFM) interactions appear, evolving into a ferromagnetic order below 24 K (FM order within the chains that are partly antiferromagnetically coupled). According to Wu *et al.* [143], the FM intrachain interactions obey an Ising-type model due to the strong spin-orbit coupling effects on the Co ions within a trigonal prismatic environment. This material has attracted much attention due to the magnetization plateaus observed in the magnetization versus field curves [138, 145].

The  $n=\infty$  member ( $BaCoO_3$ ) has also drawn considerable interest [135, 146–154]. It crystallizes in a 2H hexagonal pseudo-perovskite

structure, in which there are just face-sharing  $CoO_6$  octahedra forming the 1D  $CoO_3$  chain. In this case, the valence state of Co atoms is  $4+(d^5)$ . *Ab initio* calculations predicted a FM ground state along the chains [149]. The c-axis is assigned to be an easy direction for the magnetization, leading to a large value of the orbital angular momentum. Also a large, Ising-type, magnetocrystalline anisotropy has been estimated [153].

However, there are fewer works on the magnetic or electronic structure properties for the compounds with  $2 \leq n \leq \infty$ . Sugiyama *et al.* [135] studied the electronic structure and magnetic properties of the members  $n=1, 2, 3, 5$ , and  $\infty$ , reporting an  $n$ -dependence of the charge and spin distribution of the Co chains. They proposed a charge distribution within the chains based on  $Co^{4+}$  cations (located in octahedra) and  $Co^{3+}$  ones (located in both trigonal prisms and octahedra). The existence of a magnetic transition was shown for all the compounds. Above the temperature attributed to this transition ( $T_C^{on}$ ), a relatively strong 1D FM order appears. They suggested that, for the compounds with  $n=1, 2, 3$ , and  $5$ ,  $T_C^{on}$  is induced by an interchain 2D AFM interaction. Another magnetic study reported by Sugiyama *et al.* [155] confirmed the role of this 2D AFM interaction in the series.

Focusing in the  $n=4$  member of the series, its magnetic structure has been a controversial issue. Single crystals of the oxygen-deficient compound  $Sr_6Co_5O_{14.7}$  have been studied by Sun *et al.* [156]. They showed this compound to have unique polyhedral chains, consisting of a random composite of octahedra+trigonal prisms and octahedra+intermediate polyhedra. The magnetic properties of the compound can be understood according to that structural picture being the  $Co^{4+}$  ions located in the octahedra and the  $Co^{2+}$  ones in either the trigonal prisms or the intermediate polyhedra. Whangbo *et al.* [157] proposed an interpretation of the electronic structure of  $Sr_6Co_5O_{15}$  using a Hückel tight binding calculation [158]. According to their model, the polyhedral chains are composed by  $Co^{4+}$  ions in the octahedral

sites and  $Co^{2+}$  ions in the trigonal prismatic ones. The electrical resistivity and Seebeck coefficient temperature dependence of  $Sr_6Co_5O_{15}$  have been measured in some previous works [159, 160] showing a semiconducting behavior [161].

Our purpose in this Chapter will be to further analyze the electronic structure and special magnetic properties of the  $n=4$  member of the series,  $Sr_6Co_5O_{15}$ . In order to do that, we will study the plausible magnetic configurations and obtain the magnetic ground state of the system. Also, we will calculate the thermopower using the standard Boltzmann transport theory based on the electronic structure obtained by first principles [162, 163].

## 4.2 Computational details

For this moderately correlated transition metal oxide, we again used the LDA+ $U$  approach with the on-site Coulomb repulsion values in the interval from 4 to 8 eV, in a reasonable range compared to other similar cobaltates [143, 153], to describe correctly the semiconducting behavior of the material and the localized nature of the Co 3d electrons. We will focus in part of the analysis in a value of  $U= 4.8$  eV and of the on-site Hund's rule coupling  $J= 0.7$  eV (results presented are in any case consistent for values of  $U$  from 4 to 8 eV). Values used for the k-mesh were a  $6 \times 6 \times 6$  sampling of the full Brillouin zone for electronic structure calculations, and  $21 \times 21 \times 21$  for the transport properties.  $R_{mt}K_{max}= 6.0$  was chosen for all the calculations. Selected muffin-tin radii were the following: 1.82 a.u. for Co, 2.28 a.u. for Sr, and 1.61 a.u. for O. Based on scalar relativistic basis functions, spin orbit coupling (SOC) effects were included in a second-variational procedure [164].

## 4.3 Results

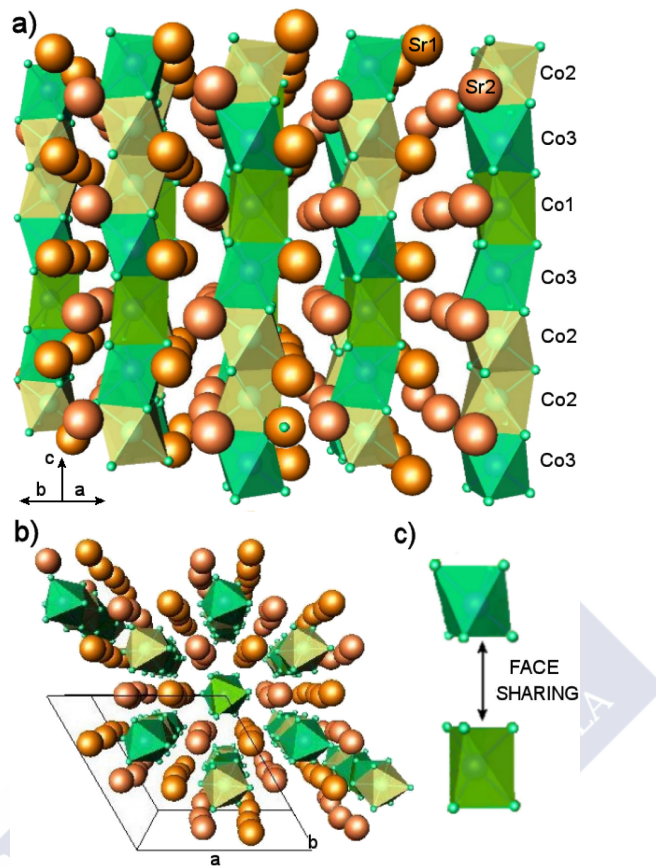
### 4.3.1 Structure

The structural data for the *ab initio* calculations were taken from [165]. The unit cell contains two strontium, three cobalt, and three oxygen atoms. The basic structure consists of isolated, 1D infinite chains of CoO<sub>6</sub> polyhedra sharing faces along the c-axis that form a hexagonal lattice in the ab plane as can be seen in Fig. 4.1b. The unit cell is formed by 5 Co atoms, 4 of them are situated in distorted octahedra and one is in a trigonal prismatic environment (see Fig. 4.1a, c). The in-plane distance between Co chains is significantly larger than the Co-Co in-chain distance, leading to the structural quasi-one-dimensionality. Giving the actual numbers, the inter-octahedral cobalt-cobalt distances are: Co2-Co3 = 2.39(3) Å, Co2-Co2 = 2.54(3) Å and the face-sharing prismatic/octahedra Co1-Co3 distance is 2.53(2) Å. The average in-plane distance between Co chains is 5.64 Å.

### 4.3.2 An ionic model

Again, being the compound a correlated semiconducting oxide [159], an image based on an ionic point charge model (PCM) can give us a crude estimate of the possible electronic configuration of the material. We will use such a model to describe the charge distribution of the cations along the Co chain. We will consider possible ionic configurations for the different Co ions along the chain and calculate their total energy, just based on the electrostatic repulsion, simplifying to take into account only the first neighbor contribution, and neglecting other energetic terms.

Taking the usual valencies for Sr and O, the average valence for Co in the ideal stoichiometric compound Sr<sub>6</sub>Co<sub>5</sub>O<sub>15</sub> is +3.6. Following the PCM we have just described, the valencies of the Co ions can be distributed in two isoenergetic ways in order to minimize the Coulomb repulsion: i) 4 Co<sup>4+</sup> (*d*<sup>5</sup>) + 1 Co<sup>2+</sup> (*d*<sup>7</sup>); ii) 3 Co<sup>4+</sup> (*d*<sup>5</sup>) + 2 Co<sup>3+</sup> (*d*<sup>6</sup>).

**Figure 4.1:**

(a) Schematic picture of the structure of the  $CoO_3$  chains in  $Sr_6Co_5O_{15}$  showing the polyhedral environment of the different Co cations that occur along them. In the unit cell, formed by 5 Co atoms, 4 of them are situated in a distorted octahedron (green color) and one is in a trigonal prismatic environment (yellow color). (b) Top view of the structure of  $Sr_6Co_5O_{15}$  showing the hexagonal symmetry of the ab plane, and the 6-fold coordination of the Co atoms by O atoms. The in-plane distance between Co chains is significantly larger than the Co-Co in-chain distance, leading to the structural quasi-one-dimensionality. (c) Detail of the face-sharing arrangement along the chains.



Various ionic arrangements have been considered in the literature. According to the structure determined by Harrison *et al.* [166], Sun *et al.* [156] proposed 4 Co<sup>4+</sup> + 1 Co<sup>2+</sup> is the most suitable model because the polyhedral chain with 4 octahedral sites and one trigonal prismatic allows Co<sup>4+</sup> and Co<sup>2+</sup> to be located in different sites. Whangbo *et al.* [157] also suggested the 4 Co<sup>4+</sup> (*d*<sup>5</sup>) + 1 Co<sup>2+</sup> (*d*<sup>7</sup>) model using a Hückel tight binding calculation. This would be what we called solution i). Instead, Sugiyama *et al.* [135] proposed the existence of at least one nonmagnetic atom in the chain for all the members of the series A<sub>n+2</sub>Co<sub>n+1</sub>O<sub>3n+3</sub>: as n increases from 1 up to infinity, the Co valence increases from +3 and approaches +4 (e.g. for n=1, the charge distribution in the unit cell is 2 Co<sup>3+</sup>; for n=2, 2 Co<sup>3+</sup> + 1 Co<sup>4+</sup> and in our case for n=4, 2 Co<sup>3+</sup> + 3 Co<sup>4+</sup>). This, we called solution ii). In addition, in [135] it is suggested that the spin distribution for the 2 Co<sup>3+</sup> ions in the chain is: a high-spin state (HSS) with S=2 for the Co within a trigonal prismatic environment and a low-spin state (LSS) with S=0 for the octahedral one. Meanwhile, the Co<sup>4+</sup> ions are all in a LSS with S=1/2 and located in the remaining octahedra.

Both solutions are energetically equivalent from an oversimplified ionic picture, but can be easily distinguished because solution ii) could lead to two nonmagnetic Co atoms, whereas solution i) will have all the atoms being magnetic. Our *ab initio* calculations confirm that the ground state electronic structure can be well described by an ionic model with 3 Co<sup>4+</sup> and 2 Co<sup>3+</sup> cations (solution ii) of our PCM). Below, we will give further details of the electronic structure beyond this simple ionic model.

### 4.3.3 Electronic structure calculations

In the previous Chapter, we saw the evolution of the electronic structure of an insulating transition metal nitride with the on-site Coulomb repulsion studying the system within the LDA+ *U* method. To understand how Sr<sub>6</sub>Co<sub>5</sub>O<sub>15</sub> is influenced by the on-site Coulomb repulsion,

**Table 4.1:**

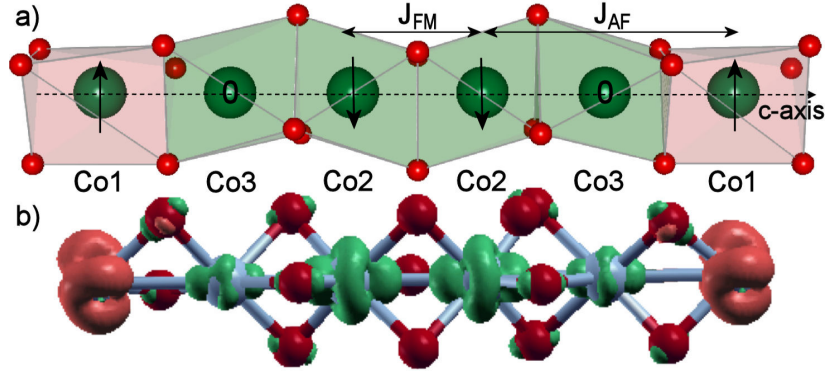
Projection of the spin MM inside the muffin-tin spheres of Co atoms in the Sr<sub>6</sub>Co<sub>5</sub>O<sub>15</sub> ground state for different  $U$  values.

Atom	MM for different $U$ values in $\mu_B$ units				
	6.4 eV	5.8 eV	5.4 eV	5.2 eV	4.8 eV
Co1	1.24	1.17	1.12	1.09	1.05
Co2	-1.01	-0.95	-0.90	-0.87	-0.81
Co3	-0.06	-0.08	-0.10	-0.13	-0.17

Table 4.1 shows the magnetic moments (MM) of each cation in the structure at different  $U$  values in a range from 4.8 to 6.4 eV for the magnetic ground state solution. Smaller values of  $U$  do not stabilize a ferrimagnetic (FiM) insulating solution, underestimating the correlation effects. The moments are consistent with the ionic distribution that would predict two nonmagnetic Co<sup>3+</sup>:  $d^6$  cations to occur along the chain. In such an insulating solution, Co1 is a Co<sup>4+</sup>:  $d^5$  cation with a MM of  $\approx 1 \mu_B$ . Co2 is also a Co<sup>4+</sup>:  $d^5$  cation and Co3 is close to a Co<sup>3+</sup>:  $d^6$  configuration. The details of the Co2 and Co3 dependence of the magnetic moments with  $U$  can be understood looking at the magnetic interactions in the chain (see Fig. 4.2a). The coupling between Co1 and Co2 is mediated by a nonmagnetic Co3. The overlap between Co3 and Co2 d-orbitals motivates a charge transfer which is higher as  $U$  decreases. We will deepen into the magnetic properties of the system in the next Section.

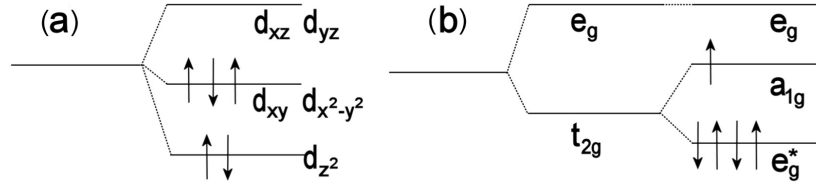
The Co<sup>4+</sup> cations are in a low-spin state ( $S=1/2$ ) in agreement with [135] inside both octahedral (Co2) and trigonal prismatic (Co1) environments. However, for our compound, both the Co<sup>3+</sup> atoms are nonmagnetic (LSS) and located in octahedra. We will focus in the nature of the hole in the Co<sup>4+</sup>  $d$ -levels that depends on several factors: the different crystal field environment of each magnetic Co, the Co in-chain interaction and the crystal field distortion.

In order to interpret the electronic structure of the compound, we can consider a three-dimensional representation of the spin density. Figure 4.2b shows such representation for  $U= 4.8$  eV (this particular

**Figure 4.2:**

(a) Schematic picture of the structure of the  $\text{CoO}_3$  chains in  $\text{Sr}_6\text{Co}_5\text{O}_{15}$ . Octahedral (trigonal prismatic) Co-environments are shown in green (red) color. We also show the ferromagnetic (FM) coupling ( $J_{FM}$ ) between neighbor Co2 atoms and the antiferromagnetic (AFM) one between Co2 and Co1 mediated by a nonmagnetic Co3 ( $J_{AF}$ ). (b) Three dimensional plot of the spin density in the FiM ground state, isosurface at  $0.1 \text{ e}/\text{\AA}^3$  obtained using XCRYSDEN [95] Red (green) color corresponds to spin-up (spin-down) densities.

choice of  $U$  will be discussed below). The spin density for Co atoms within a trigonal prismatic environment is clearly different from the octahedral one. For analyzing the spin density, we have to consider the proper coordinate system for the Co ions. The Co1 spin density can be interpreted according to the prismatic crystal field splitting, taking the  $z$  axis along the Co-chains ( $c$ -axis). The electronic structure of a  $\text{Co}^{4+}$ :  $d^5$  cation in such environment is depicted in Fig. 4.3a with the hole occupying the  $d_{xy}/d_{x^2-y^2}$  level in agreement with the spin density seen in Fig. 4.2b for Co1. For the octahedral Co atoms (Co2 and Co3), the trigonal distortion has to be taken into account (see Fig. 4.3b). The  $e_g$  orbitals are not affected by the trigonal distortion. The  $t_{2g}$  levels split into a higher-lying singlet  $a_{1g}$  and a lower-lying  $e_g^*$  doublet. The  $a_{1g}$  singlet spatial shape is that of a  $d_{z^2}$  orbital along the trigonal  $c$ -axis. The spin density shown in Fig. 4.2b for Co2 (and also for Co3 due to hybridization) corresponds to one hole in the singlet. In this case, the  $a_{1g}$  orbital is the higher-lying one since the octahedral  $\text{Co}^{4+}$ :  $d^5$  are

**Figure 4.3:**

Level scheme representing (a) the prismatic crystal field levels for a  $Co^{4+}$  cation and (b) the electronic structure for a  $Co^{4+}$  cation in a trigonally distorted octahedral environment. The splitting of the  $t_{2g}$  levels caused by this distortion can be observed.

surrounded not only by  $Co^{4+}$  but also by  $Co^{3+}$  cations and the  $Co^{4+}-Co^{3+}$  distance is smaller than the  $Co^{4+}-Co^{4+}$  one.

To better understand the changes in the electronic structure of the compound as  $U$  increases, Fig. 4.4 shows the density of states (DOS) plots of the Co atoms in the unit cell for the two extremal  $U$  values shown in Table 4.1 ( $U = 4.8$  eV and  $U = 6.4$  eV). The material is an insulator for this range of  $U$  values, with a  $d-d$  gap that increases from 0.5 eV to 1 eV as  $U$  does. For Co1 ( $Co^{4+}: d^5$ ) we can see the spin split  $d_{xz}/d_{yz}$  bands (by about 1 eV for  $U = 4.8$  eV and 1.5 eV for  $U = 6.4$  eV). For  $U = 4.8$  eV, the unoccupied  $d_{xy}/d_{x^2-y^2}$  orbital for Co1 is shifted respect to the  $d_{xz}/d_{yz}$  one at about 2 eV above the Fermi level. For  $U = 6.4$  eV, such a shift does not appear and the hole is at about 2.5 eV. For Co2 ( $Co^{4+}: d^5$ ), we can see a spin splitting of the  $e_g$  bands (by less than 1 eV for  $U = 4.8$  eV and 1 eV for  $U = 6.4$  eV). The hole in the  $a_{1g}$  singlet of Co2 presents a double peak structure at about 1 eV above the Fermi level for the lower  $U$  value and at 1.5 eV for the higher one. For Co3, we can observe an approximate  $d^6$  DOS plot. Due to the hybridization between Co3 and Co2 d-orbitals a double peak structure arises (at the same energy than for Co2), showing a small density of unoccupied  $t_{2g}$  states for Co3. As the overlap diminishes with increasing  $U$  values, this density is reduced for  $U = 6.4$  eV. The  $e_g$  bands for Co3 present a small spin-splitting for  $U = 4.8$  eV, negligible for the higher  $U$  value. The evolution with  $U$  of the MM for Co3 can be observed: its value rises

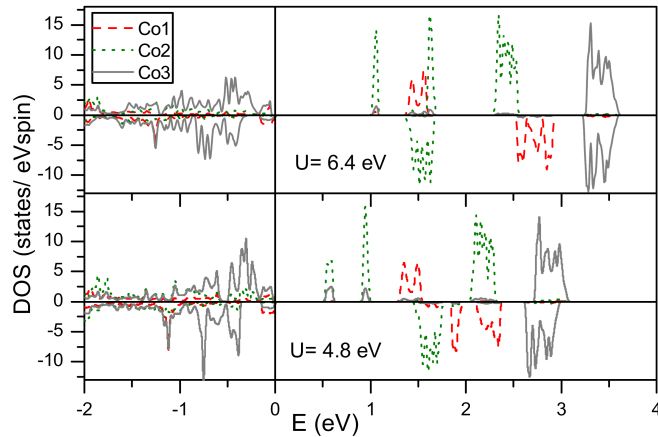


**Figure 4.4:**

Partial spin-polarized DOS of Co1, Co2, and Co3 atoms for  $U= 4.8$  eV and  $U= 6.4$  eV. Fermi energy is represented by the solid vertical line at zero. Upper (lower) panels show the spin-up (down) channels. Co1 and Co2 are close to a  $d^5$  electronic structure. Co3 is closer to a  $d^6$  configuration with a little unoccupied  $t_{2g}$  character.

from 0 as  $U$  decreases, while it lowers from  $1 \mu_B$  for Co2. An ionic picture works in explaining the electronic structure of this insulating compound, characterized by very narrow bands. This is more evidently so for larger values of  $U$ .

Two features can be observed in these plots: i) the strongly localized nature of the electrons, with very narrow bands, less than 0.5 eV wide. The band widths are always smaller than the typical energies involved: both the Hund's rule coupling strength (1 eV for the  $e_g$  bands of the  $Co^{4+}$ :  $d^5$  cations) and crystal field splitting, ii) the different crystal field environments of the Co cations (octahedral for Co2 and Co3, trigonal prismatic for Co1), that lead to well different splittings with the  $e_g$  states of Co3 being highest in energy, at  $\approx 3$  eV above the Fermi level for the  $U$  value of 4.8 eV. Higher  $U$  values produce a rigid shift of the bands shown in Fig. 4.4 with an increase of the band gap, but the description of the band structure and the main conclusions remain unchanged.

From these results, we can roughly sketch the electronic structure of Sr<sub>6</sub>Co<sub>5</sub>O<sub>15</sub>: its unit cell is formed by three magnetic Co<sup>4+</sup>:  $d^5$  cations (one Co1 in a trigonal prismatic environment and two Co2 in an octahedral environment) and two nonmagnetic Co<sup>3+</sup>:  $d^6$  atoms (Co3) in an octahedral environment.

#### 4.3.4 Magnetic properties

We have performed LDA+ $U$  calculations for several values of the on-site Coulomb repulsion term. Since we are dealing with a semiconducting  $d^5/d^6$  system a value of  $U$  between 4 and 8 eV is reasonable to describe it correctly as we have explained above [73]. The magnetic ground state solution we will describe below (magnetic moments of Co atoms in the ground state are written in Table 4.1) is the most stable for the above mentioned range of values of the on-site Coulomb repulsion.

Starting from the electronic structure described above, we can understand the magnetic couplings in the unit cell. Two couplings can be considered (see Fig. 4.2a): one ferromagnetic ( $J_{FM}$ ) direct exchange between nearest neighbor magnetic Co2:  $d^5$  cations and another one antiferromagnetic ( $J_{AFM}$ ) between Co1:  $d^5$  and Co2:  $d^5$  mediated by a nonmagnetic cation Co3:  $d^6$ , that acts in a similar way to O anions in the oxygen-mediated superexchange in perovskites. Both these couplings can be understood in terms of the Goodenough-Kanamori-Anderson rules [167]. We can use our total energy calculations to describe and quantify the magnetic interactions in the unit cell (schematically depicted in Fig. 4.2). In order to give an estimate of the couplings along the chain, we can fit the total energies resulting from various possible collinear magnetic configurations to a Heisenberg model, in the form  $H = \frac{1}{2} \sum_{i,j} J_{ij} S_i S_j$ . Calculations reveal the following values for the coupling constants  $J_{FM} \approx 220$  K and  $J_{AFM} \approx 6$  K (of opposite sign). As expected, the FM coupling is stronger than the AFM one, that occurs between second-neighbor cations mediated by a nonmagnetic ion. Because of this peculiar magnetic arrangement, no 1D FM order (along

the Co chains) is observed, but only a short-ranged FM coupling between Co<sup>2+</sup> cations survives at high temperature. The existence of an in-chain AFM coupling and two nonmagnetic Co atoms per unit cell will also affect the inter-chain interactions. Being the in-chain magnetic couplings not purely FM, the magnetic properties of Sr<sub>6</sub>Co<sub>5</sub>O<sub>15</sub> can no longer be understood as FM spin-chains coupled antiferromagnetically in-plane, as occurs in Ca<sub>3</sub>Co<sub>2</sub>O<sub>6</sub> [143]. Also reasoning in terms of the hexagonal planes, the nonmagnetic planes formed by Co<sup>3+</sup> atoms which intercalate between the magnetic ones will contribute to the lowering of the inter-chain magnetic couplings. The total ordered moment is 1  $\mu_B$  per unit cell.

Experiments [162, 165] give further evidence of the lack of long-range magnetic order due to the particular magnetic ground state predicted *ab initio*. Magnetic susceptibility *vs.* temperature measured at H=100 Oe under ZFC and FC conditions shows, below 220 K, a splitting between ZFC and FC curves. This effect is quite common in other cobaltates [168, 169], and it is often attributed to spin-glass effects or other types of magnetic inhomogeneities. According to the refinement of NPD data [165], the average cobalt deficiency was determined to be of around 6%. The observed effects due to magnetic inhomogeneities are brought about in this particular case by the arrangement of Co<sup>3+</sup> and Co<sup>4+</sup> cations, that are not homogeneously distributed throughout the solid. On the 5 K NPD pattern there is no additional contribution to the scattering [165]. These experimental results indicate that there is no long-range ordering over a sufficiently large coherent domain to give rise to magnetic scattering as has also been observed by Zhao *et al.* [170]. As mentioned above, we could be in the presence of a partially disordered structure with spin-glass-like features. In addition, the described FiM ground state found *ab initio* could perfectly take place in spatially limited regions of the structure lacking the required long-range coherence to be detected by diffraction methods.

At 32 K a kink corresponding to an intrinsic magnetic transition is observed in the susceptibility *vs.* temperature curve [162]. The linear

fitting of  $\chi(T)^{-1}$  curve in the paramagnetic region reveals a negative Curie-Weiss temperature (in agreement with that obtained by Zhao *et al.* [170] and by Sugiyama *et al.* [135] for other intermediate members of the series). Based on the similarities among the family of cobaltates Sr<sub>6</sub>Co<sub>5</sub>O<sub>15</sub> structurally belongs to, and considering we do not have purely FM in-chain couplings, the kink observed at 32 K can be assigned to the existence of an interchain 2D AFM order in the triangular lattice of the ab plane as in the other members of the series. Because the in-chain magnetic couplings are not purely FM and a long-range FM order cannot be established along the chains, the occurrence of 1D-FM order slightly above T<sub>N</sub> is not expected in this compound, as it occurs in other members of the series. Based on the FiM ground state obtained from our calculations, the importance of the inter-chain AFM interactions (non-one-dimensional magnetic couplings) has been further confirmed by Lin *et al.* [171].

From our calculations at  $U=4.8$  eV, we can also obtain the value of the effective magnetic moment per formula unit and compare it with the experimental findings [162]. Hence, taking the usual expressions for the square effective paramagnetic moment of each magnetic Co,  $\mu_{eff}^2 = [g_l^2 l(l+1) + g_s^2 s(s+1)] \mu_B^2$  and considering  $l=0$  or  $1$ ,  $\mu \in [5.2, 6.7] \mu_B$  for the whole unit cell formed by 5 Co cations. Depending on the value of the orbital angular momentum (see below the details of our calculations), that would be the range of possible values for  $\mu_{eff}$ . This is consistent with the  $5.6 \mu_B$  value obtained by Sun *et al.* [156], (if the orbital angular momenta were negligible), and it agrees with the experimental magnetic moment of  $6.9 \mu_B$  per formula (if the orbital angular momenta were aligned with the magnetization). This value was obtained from the linear fitting of  $\chi^{-1}$  vs T curve in the paramagnetic region [162]).



### 4.3.5 A peculiar quasi-one-dimensional oxide

The two end members of the series have in common an Ising-type behavior [143, 153], with moments aligned along the chain direction with large values of the magnetocrystalline anisotropy. This quasi-one-dimensionality is somehow not observed in Sr<sub>6</sub>Co<sub>5</sub>O<sub>15</sub>. We have studied the system by introducing SOC in the calculations with the magnetization lying along different crystallographic directions. However, none of these directions can align the orbital and magnetic moments of all the Co atoms at the same time (see Table 4.2). Large values of the orbital angular momenta are obtained for the Co atoms in the structure when the magnetization is set along different directions: the preferred direction for orienting their moments is different for each magnetic Co (Co1 and Co2) in the unit cell. For them, the orbital angular momentum is parallel to the spin moment, as a result of Hund's third rule. For Co1, the degenerate  $x^2-y^2$  and  $xy$  levels (where the hole resides) can form a linear combination of eigenstates with  $l_z=2$  [143], so the Co<sup>4+</sup>: $d^5$  cation in a prismatic environment is susceptible of developing a ground state with a large value of the orbital angular momentum. On the other hand, Co2 (Co<sup>4+</sup>:  $d^5$ ) can develop an  $l_z=1$  eigenstate since the  $t_{2g}$  multiplet acts as an effective  $l=1$  multiplet [172–176]. The ground state quantization axis will be related to the local environment which is rotated for the two Co2 atoms in the unit cell. This explains why we have different  $l_z$  values even for the two equivalent Co2 atoms in the structure. Consequently, this spin-system cannot be described as an Ising-type one due to the canting of the moments of the various magnetic ions with respect to each other. Such canting can be understood according to the different Co environments and as a local orientation of the moments along their particular symmetry axis. The values are summarized in Table 4.2, and help understand the measured  $\mu_{eff}$  value.

Another difference with the other compounds in the series is that, in this case, the 2Co<sup>3+</sup> atoms are non magnetic (LSS) and located in

**Table 4.2:**

Projection of the orbital angular momenta of Co atoms along the magnetization axis for different directions of the magnetization (in  $\mu_B$  units).

Atom	$l_z$ for various magnetization directions						
	(111)	(101)	(110)	(011)	(100)	(010)	(001)
Co1	0.99	0.75	0.66	0.72	0.41	0.36	0.44
Co2(a)	-0.05	-0.15	-0.17	-0.19	-0.22	-0.28	-0.31
Co2(b)	-0.05	-0.20	-0.18	-0.17	-0.28	-0.29	-0.27

octahedra while in the other members of the series one of them is in a LSS in an octahedral environment and the other one in a HSS and located in the trigonal prismatic site. In addition, we do not have a strong in-chain FM coupling for all the Co atoms in the unit cell. Thus, the magnetic properties of Sr<sub>6</sub>Co<sub>5</sub>O<sub>15</sub> cannot be understood as FM spin chains because of the AFM coupling that (though weak) occurs within them and the two nonmagnetic Co atoms in every unit cell.

Clearly, the magnetic properties of this compound differ from the other members of the series making it less quasi-one-dimensional.

### 4.3.6 Transport properties.

We have calculated the temperature dependence of the thermoelectric power to analyze the system properties and the magnetic ground state. For the FiM ground state solution, taking the conductivity ( $\sigma$ ) and Seebeck coefficient ( $S$ ) calculated for both spin channels, the total thermopower has been obtained according to the two-current model expression [177]:

$$S = \frac{\sigma'(\uparrow)S(\uparrow) + \sigma'(\downarrow)S(\downarrow)}{\sigma'(\uparrow) + \sigma'(\downarrow)} \quad (4.1)$$

where  $\sigma' = \sigma/\tau$ , within the constant scattering time ( $\tau$ ) approximation (the overall expression is  $\tau$  independent. For the sake of comparison, we present the calculations obtained for the ground state in-chain FiM spin configuration shown in Fig. 4.2 and also for a FM solution (which is higher in energy according to our calculations). We present the data

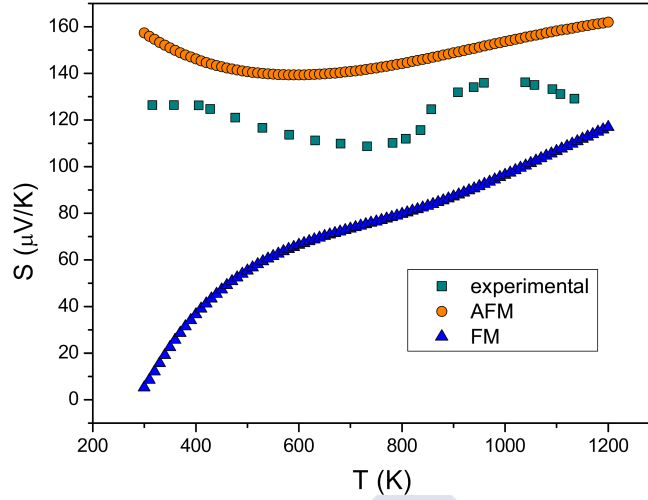


**Figure 4.5:**

Experimental [159] and calculated temperature dependence of the thermopower. The results for both the FM and FiM spin-configurations are plotted.

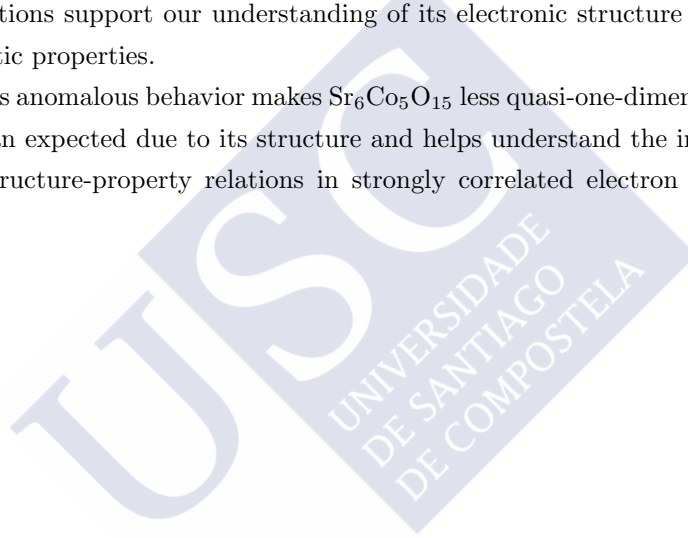
calculated for both spin configurations at  $U = 4.8$  eV, together with the experimental values of the Seebeck coefficient [159] (see Fig. 4.5). The results for the FiM solution fit the experimental values nicely, both in order of magnitude of the thermopower and also on the observed non-activated evolution with temperature (higher  $U$  values just cause a rigid shift of the curve towards higher values of the thermopower). However, the FM one differs clearly from the experiment, giving further evidence of the validity of our description of the electronic structure of the compound.

## 4.4 Summary

We have performed *ab initio* calculations on the compound  $Sr_6Co_5O_{15}$ . The material is structurally quasi-one-dimensional and can be identified as a member of the structural series  $A_{n+2}B'B_nO_{3n+3}$  of hexagonal quasi-one-dimensional Co oxides. It is a semiconductor with a FiM

ground state that shows some peculiar electronic structure properties that make it different than the other members of the series: i) Both the  $Co^{3+}$  atoms are nonmagnetic and located in octahedra. ii) The in-chain couplings are not purely FM, AFM couplings (though weak) occur within the chains. iii) This, together with the existence of two nonmagnetic Co atoms in the unit cell, reduce not only the in-chain but also the inter-chain magnetic couplings. iv) Due to ii) and iii) the magnetic properties of the material can no longer be understood as FM spin chains coupled AFM in-plane as occurs in other members of the series. v) The preferred orientation of the orbital angular momenta is non-collinear, in contrast to the strong Ising-type behavior found in  $Ca_3Co_2O_6$  and  $BaCoO_3$ . In addition, transport properties calculations support our understanding of its electronic structure and magnetic properties.

This anomalous behavior makes  $Sr_6Co_5O_{15}$  less quasi-one-dimensional than expected due to its structure and helps understand the intricate structure-property relations in strongly correlated electron systems.



## Enhanced thermoelectric response of hole-doped $\text{La}_2\text{NiO}_{4+\delta}$ by ab initio calculations

“

*In all affairs it's a healthy thing now and then to hang a question mark on the things you have long taken for granted.*

*[Bertrand Russell]*

”

### 5.1 Background

Up to now, we have used transport properties calculations as a guide to confirm the magnetic ground state of two different systems ( $\text{CrN}$ , and  $\text{Sr}_6\text{Co}_5\text{O}_{15}$ ). However, as we saw in Chapter 1, the optimization of the thermoelectric properties of a material has become a very important issue in Materials Science since thermoelectric materials with an enhanced efficiency show up as an alternative to the use of fossil fuels. We already explained that transition metal oxides, and particularly misfit layered cobaltates are promising in principle because of

their chemical stability and possibility of usage in high temperature devices [177–179]. Large thermopower together with metallic conductivities place that family as one of the most relevant and thoroughly studied within the oxides. One electronic structure reason behind their interesting thermoelectric properties is the existence of two electronic systems within those cobaltates [180]. Due to the trigonally distorted octahedral environment, the Co  $t_{2g}$  bands are split between a highly mobile wide band that drives metallic conduction (of  $e_g^*$  character) and a more localized band (with  $a_{1g}$  parentage), narrow in nature that provides a large Seebeck coefficient (see Fig. 5.1b) [42].

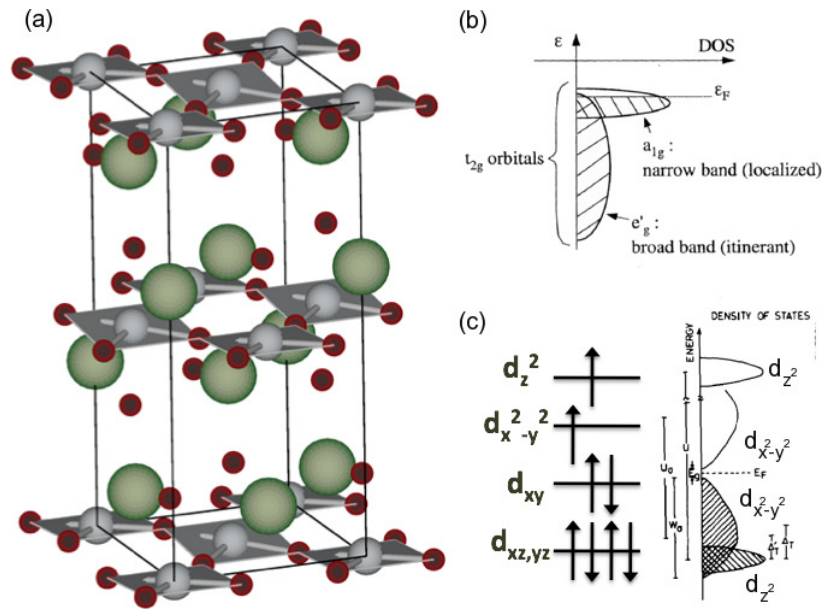


**Figure 5.1:** (a) Layered structure of  $\text{La}_2\text{NiO}_4$  with La atoms depicted in green, oxygens in red and Ni in gray. The building blocks formed by  $\text{NiO}_2$  planes with a square planar coordination around the metal cations and La acting as spacer between the layers can be seen. (b) Schematic illustration of energy levels for the split Co  $t_{2g}$  bands in layered cobaltates. (c) Level scheme representing the square planar crystal field levels of a  $\text{Ni}^{2+}$  cation and schematic illustration of energy levels for the split Ni  $e_g$  bands in  $\text{La}_2\text{NiO}_4$  taken from [181].

The search for new oxide compounds that could present a similar thermoelectric response is hence an interesting issue to be pursued. We consider here that a possible candidate family for that sake are a particular kind of layered nickelates: hole-doped  $\text{La}_2\text{NiO}_4$ . This compound and others related to it have drawn the attention of the community for various reasons: i)  $\text{La}_2\text{NiO}_4$  is isostructural with the parent compound of the high- $T_c$  cuprates [182]:  $\text{NiO}_2$  planes with a square planar coordination around the metal cations form the building blocks of this layered material, with La acting as spacer between the layers, as can be seen in Fig. 5.1a ii) an interesting temperature-induced metal-insulator transition (MIT) occurs in it [183], and links it with the compounds we have studied up to now in this Thesis, iii) it is possible to lower further the valence of the Ni cation in a layered structure to compare it with superconducting cuprates, not only in terms of structure but also with the same electron count [184–190]. Back in the eighties, the MIT was explained by Goodenough and Ramasesha [181] as occurring in a system where two different  $d$ -states coexist around the Fermi level, having clearly distinct band widths. This is reminiscent of the above mentioned cobaltates, but in this case two different  $e_g$  bands exist, a more localized  $d_{z^2}$  and a more itinerant  $d_{x^2-y^2}$  band as can be seen in Fig. 5.1c. These yield reasonable conductivities, and also due to the existence of a more localized set of narrow bands, interesting values of the thermopower could emerge.

Experimental studies of the Seebeck coefficient in  $\text{La}_2\text{NiO}_4$  show promising values exceeding  $100 \mu\text{V}/\text{K}$  at room temperature [191], (the typical minimum value for a material to be considered a high performance thermoelectric) even though most reports with oxygen-rich samples show smaller values (we will argue below what the reason for this is). The electrical conductivity is larger in the  $\text{NiO}_2$  planes [192], which is the expected behavior for such a layered structure. As explained in the Introduction, to obtain an estimate of the thermoelectric performance of a material, it is common to use the so-called dimensionless figure of merit, which is defined as the quantity  $zT = \sigma TS^2 / \kappa$ . With

the best values obtained experimentally for  $S \sim 100 \mu\text{V/K}$  [191],  $\rho \sim 5 \text{ m}\Omega\cdot\text{cm}$  [192, 193] and  $\kappa \sim 7.5 \text{ W/m}\cdot\text{K}$  [194], a  $zT$  at room temperature of about 0.01 can be estimated, which is comparable to other promising compounds such as CrN (treated in Chapter 3), particularly so because of the large room for improvement, some of which we will discuss in this Chapter. In particular, the layered structure of the compound would be prone to yield better conductivity when grown in the form of thin films, and this has been shown in the past [193]. As explained in the Introduction, a thin film geometry would hamper thermal conductivity along the  $c$ -axis, which would eventually improve the thermoelectric figure of merit as long as thermopower and mobility are not reduced [195]. Also, oxygen excess can lead to hole doping and a corresponding increase in electrical conductivity. A vast amount of experimental information existed on the thermoelectric and transport properties of  $\text{La}_2\text{NiO}_4$ . However, an exact account of the oxygen content is necessary to obtain good systematics, and this is not easily found in literature, probably due to complications in the correct determination and stabilization of a particular oxygen content.

This leads us to explore a possible path towards an improved thermoelectric response via oxygen doping in  $\text{La}_2\text{NiO}_4$ . In particular, we will discuss in this Chapter how moving the system into the more itinerant limit by hole doping can reduce further the importance of the phononic part of the thermal conductivity (that works against a good thermoelectric performance) relative to the electronic part, and also improving the figure of merit if a decrease in the thermopower is prevented [196]. Concerning the magnetic order, it has been shown that  $\text{La}_2\text{NiO}_4$  is an antiferromagnet with an in-plane ordering such that an antiferromagnetic (AFM) interaction between nearest neighbor Ni atoms is stabilized through an  $e_g^2$ -O- $e_g^2$  superexchange interaction. The commensurability of the ordering has been put into question [197], but careful studies with respect to the oxygen content show how the Néel temperature is significant even at values of  $\delta \sim 0.1$  [198], and could vanish at  $\delta \sim 0.14$  [191]. We will focus our calculations in that doping



level ( $\delta < 0.15$ ), close to the localized electron limit where magnetic order is present at low temperature and our DFT calculations, that assume a magnetically ordered phase at zero temperature, can describe the system more accurately. All calculations presented here will have that type of ordering imposed.

## 5.2 Computational Procedures

We will present calculations of the electronic structure and transport properties obtained with various exchange-correlation functionals (as we did in Chapter 3 for CrN) and for several doping levels. For the exchange-correlation functional in the calculations at  $U = 0$ , we have used the Perdew-Burke-Ernzerhof of the GGA.

To deal with strong correlation effects that are widely acknowledged to play an important role in this type of nickelates, we apply again the LDA+ $U$  scheme. A description of the results obtained at different values of  $U$  (in a reasonably broad range 4.5-8.5 eV for the Ni cations) was performed, but results presented here will be for  $U = 7$  eV. No significant changes in the main conclusions are found within that range of  $U$  values. The value chosen for the on-site Hund's rule strength is  $J = 0.7$  eV and is kept fixed.

Also, the Tran-Blaha modified Becke-Johnson (TB-mBJLDA) potential was used. We have seen in Chapter 3 that this potential has been shown to provide an accurate account of the electronic structure of correlated compounds using a parameter-free description.

All calculations were fully converged with respect to all the parameters used. In particular, we used  $R_{mt}K_{max} = 7.0$ , a k-mesh of  $10 \times 10 \times 4$ , and muffin-tin radii of 2.35 a.u. for La, 1.97 a.u. for Ni and 1.75 a.u. for O. For the transport properties calculations, denser k-meshes up to  $40 \times 40 \times 15$  were used to reach convergence.

To simulate small doping values we have used the virtual crystal approximation (VCA) [199]. This consists on modifying the total number of electrons in the system (also the total atomic number for charge neutrality) to simulate a particular doping level.

## 5.3 Results

### 5.3.1 Basic description of the electronic structure

As in previous chapters, a simple ionic picture can give us a first view of the electronic structure of  $\text{La}_2\text{NiO}_4$ . An ionic model gives a formal valence  $\text{Ni}^{2+}:\text{d}^8$ , which is always a  $S=1$  ion. Typically, for this type of low-valence nickelate, with the  $\text{Ni}^{2+}$  cations in a square planar environment, one would expect the  $xz/yz$  doublet fully occupied, and a higher position of the  $xy$  singlet competing in occupation with the  $e_g$  bands (which are also split and will have significantly different band widths). The expected situation would be a lower  $xy$  band fully occupied and two  $e_g^\perp$  unoccupied bands, being the band gap [200] of a distinct  $d-d$  character. (see Fig. 5.1c)

Figure 5.2 shows the calculated density of states (DOS) for  $\text{La}_2\text{NiO}_4$  in an AFM solution, both for GGA and a TB-mBJLDA scheme together with the GGA band structure in the lower panel (with the different  $d$ -character of the various Ni bands specified). Similar DOS curves are obtained with the various functionals, the size of the gap being the main difference, and also some differences exist in the particular band widths and position of the bands, but even calculations with  $U=0$  yield an insulating solution as long as in-plane AFM order is set. In the DOS plots, we only show the  $e_g$  states of the Ni cations since these are often quoted to have the dominant contribution above and immediately below the Fermi level (and we want to see them with some degree of clarity). Furthermore, due to the square planar oxygen environment, the  $e_g$  states are significantly split, and differ substantially not only in position but in width. The  $d_{x^2-y^2}$  band is higher in energy due to

crystal-field splitting caused by the larger distance to the apical oxygens around the Ni cations, but it is slightly wider, whereas the  $d_{z^2}$  band is lower but it is composed of more localized electrons (it is narrower). One can see this very clearly in the band structure figure. The  $d_{z^2}$  bands appear both in the GGA and TB-mBJLDA calculations much narrower, less than 1 eV band wide, being the corresponding  $d_{x^2-y^2}$  band width at least 2 eV. In the band structure figure (lower panel), we can also see that not only the  $e_g$  levels are in the vicinity of the Fermi level but also the  $t_{2g}$  states are placed somewhat close to it, and are actually in the same energy region as the majority-spin  $d_{z^2}$  band. However, the top of the valence band is distinctly of  $d_{x^2-y^2}$  character.

This is a narrow-gap oxide (of only 70 meV [200] according to resistivity measurements), but calculations show that the gap is substantial (0.6 eV for GGA, 1 eV for LDA+ $U$  at  $U=7$  eV and 2 eV for TBmBJLDA). Other narrow-gap oxides show this type of band gap overestimation coming out from calculations and still the calculations of the transport properties agree well with experiments (as we could see in Chapters 3 and 4 for CrN and  $\text{Sr}_6\text{Co}_5\text{O}_{15}$ , respectively). One possibility for this could be the fact that the low gap value obtained from resistivity measurements comes from shallow states in the gap, being the actual band gap much larger, as happens in CrN. In the case of  $\text{La}_2\text{NiO}_4$ , a small band gap is consistent with the temperature-induced MIT observed. The MIT in this system has been described as a temperature-induced broadening of the  $d_{x^2-y^2}$  bands that eventually overlap the occupied with the unoccupied band of opposite spin yielding metallic behavior at high temperature in the parent compound [183]. The large gap is consistent with a temperature-induced broadening as a cause of the metal-insulator transition, both in the GGA case and more so with the larger gap predicted by TB-mBJLDA.

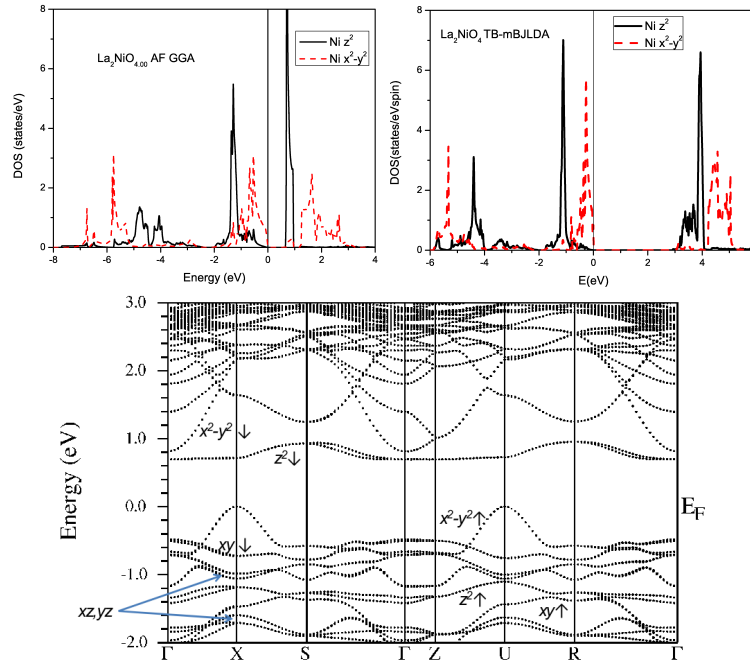


**Figure 5.2:**

DOS of the Ni  $e_g$  levels in  $\text{La}_2\text{NiO}_4$  ordered AFM within GGA and TB-mBJLDA. Observe the more localized  $d_{z^2}$  band and the broader  $d_{x^2-y^2}$ , particularly noticeable in the GGA calculation. The lower panel shows the band structure in the GGA calculation. The  $t_{2g}$  bands are in the same energy region as the majority  $d_{z^2}$  band.

### 5.3.2 Tuning the electronic structure via hole-doping

As mentioned before, if somehow one can complement metallic conductivity with the maintenance of a large thermopower and a reduced thermal conductivity, the material could then be comparable in thermoelectric performance to other transition metal oxides such as  $\text{Na}_x\text{Co}_2\text{O}_4$  [201]. Let us see how this can be done in this particular case. As can be seen, the DOS rises rapidly right below the top of the valence band

( $d_{x^2-y^2}$ -character) which is generally favorable for having a large thermopower according to the Mahan-Sofa theory, as seen in Chapter 1. A similar heavy-electron band appears somewhat also in the electron-doping region just above the bottom of the conduction band (in that case, of  $d_{z^2}$  parentage) although with less dispersive character. Hence, the more localized  $d_{z^2}$  band should contribute substantially to the Seebeck coefficient in the hole-doping region as well, but its DOS peak is very far from the Fermi level to be attained by a relatively small hole-doping level. This would instead move the chemical potential into the occupied  $x^2-y^2$  band with a noticeable increase in electrical conductivity. This band could also be sufficiently narrow to retain a substantial value of the thermopower if the chemical potential lies in a region inside the valence band comprising a large derivative of the density of states.

In order to see this in detail, we can start by analyzing the electronic transport properties of the parent compound. We have calculated these for  $\text{La}_2\text{NiO}_4$  using various exchange-correlation potentials. The value of the thermoelectric dimensionless figure of merit  $zT = T\sigma S^2/\kappa$  is independent of the scattering time chosen and so are the thermopower and  $\sigma/\kappa$ , as long as the constant scattering time approximation is retained, as explained in Chapter 1. In Fig. 5.3 we present the thermoelectric figure of merit as a function of the chemical potential calculated at 400 K using different exchange-correlation functionals. We study the electronic part only, we do not consider phonon terms in the thermal conductivity, which might be substantial in particular for the localized electron limit. Thus, this electronic-only  $zT$  can be considered as a theoretical upper limit of the figure of merit for this system. We will see below how we can make an estimate of these effects based on the experimental data for  $\sigma$  and  $\kappa$  taken from experiments [192–194].

Figure 5.3 shows a reasonably large value of the thermoelectric figure of merit for the stoichiometric compound (chemical potential at the top of the valence band), which is given by the large positive Seebeck coefficient, in qualitative agreement (see the discussion below) with experimental observations at low- $\delta$  (oxygen excess) values [191]. However,

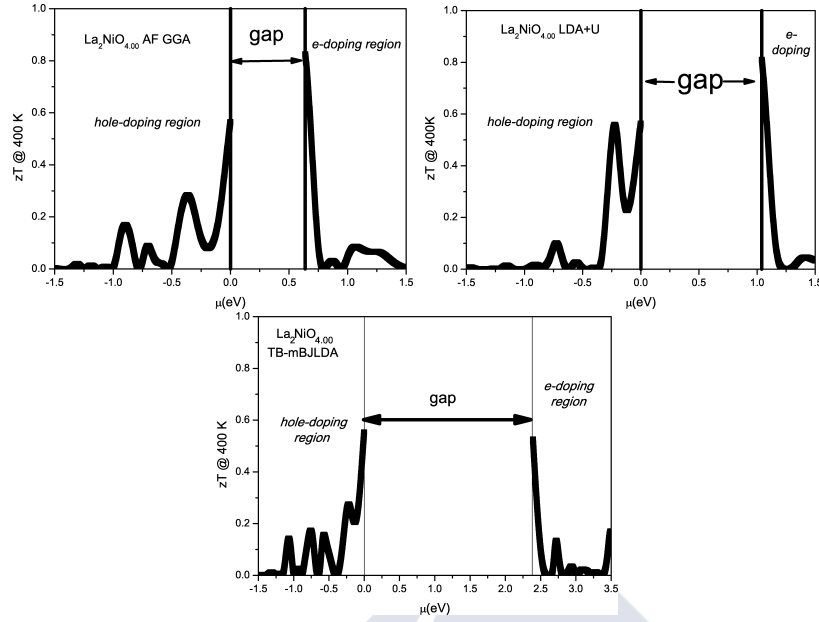


**Figure 5.3:**

Dimensionless figure of merit calculated at 400 K (electronic part only) of  $\text{La}_2\text{NiO}_4$  AFM within GGA, the LDA+ $U$  approach and TB-mBJLDA as a function of chemical potential ( $\mu=0$  represents the Fermi level). Observe a peak in the figure of merit for small hole-doping levels.  $zT$  becomes zero at about -0.3 eV when the Seebeck coefficient changes sign from positive to negative, a similar feature happens in the electron-doped region,  $S$  goes from negative to positive when the system is further electron doped.

this is expected to be hampered by the large thermal conductivity due to phonons ( $\kappa_{ph}$ ), that would substantially surpass its electronic counterpart ( $\kappa_{el}$ ), which is the only component we are analyzing with these calculations. In any case, moving towards the itinerant-electron limit, when  $\kappa_{el}$  starts being comparable to  $\kappa_{ph}$ , these results become more significant. We observe an interesting peak in the figure of merit in the hole-doping region (oxygen excess, positive values of  $\delta$ , negative chemical potential). This peak is present independently of the exchange-correlation functional used, but the characteristics (height and position in chemical potential) vary depending on the method used.

Here we try to describe a physical phenomenon that occurs in a range of physical parameters (in this case  $\delta$ , the oxygen excess) in  $\text{La}_2\text{NiO}_{4+\delta}$  but the quantitative values of which are very difficult to obtain *ab initio*. The peak is related to the  $x^2 - y^2$  bands, as we can see comparing Fig. 5.3 with the DOS plots in Fig. 5.2 (the energy window of the large peak in  $zT$  lies inside that band). We also observe that other peaks in  $zT$  appear at higher hole-doping concentrations (more negative chemical potential), related in that case with the  $d_{z^2}$  and  $t_{2g}$  bands. Even though the  $d_{z^2}$  band is certainly narrower, it does not provide a sufficiently high  $zT$  compared to  $x^2 - y^2$  (a multipeak structure is predicted by the TB-mBJLDA functional) because it is merged in the same energy region as the  $t_{2g}$  bands. If somehow band engineering could be done to bring the  $d_{z^2}$  band closer to the Fermi level, the possible thermopower obtained could be enhanced taking benefit of the localized nature of the band, and at a significantly smaller doping level. The realization of this possibility looks difficult. We will deepen into this hypothesis in the next Chapter. It can also be observed how  $zT$  becomes zero at about -0.3 eV simultaneously with the Seebeck coefficient sign change from positive at low doping to negative at higher doping levels. A similar feature happens in the electron-doped region,  $S$  goes from negative to positive when the system is further electron doped (about 0.2 eV above the bottom of the conduction band).

In order to characterize in more detail that first peak in  $zT$  at  $\delta \neq 0$ , and see how the amount of oxygen excess (hole-doping) relates to a particular change in chemical potential in the system we present in Fig. 5.4 the calculated thermopower of the hole-doped system at 400 K for all the functionals used. Since the behavior of  $\sigma/\kappa$  is relatively monotonous both with temperature and doping, the behavior of the thermopower (its peaks and sign changes) gives the broad picture of how the figure of merit itself evolves. The dependence of the Seebeck coefficient with both doping level and  $\delta$  value is shown. A peak can be observed in all the curves although it is more pronounced for LDA+ $U$  and becomes broadened within TB-mBJLDA. The height of the peak

is related to the width of the  $x^2 - y^2$  band, which is narrowed by the LDA+ $U$  method, and broadened by the TB-mBJLDA scheme. An intermediate situation is given by uncorrelated GGA. The doping level necessary to reach it depends on the relative position of that band with respect to the Fermi level in the calculations, GGA placing it further away than the other methods (see Fig. 5.2, top panel). It can be seen that for LDA+ $U$  the peak is located at  $\delta \sim 0.03$ , whereas for GGA and TB-mBJLDA it appears at higher doping levels  $\delta \sim 0.06$  and  $0.07$ , respectively. In addition, the above described sign change of the Seebeck coefficient in the hole-doped region can be seen for both GGA and LDA+ $U$  at  $\delta$  close to 0.15 (larger, beyond the values of doping we are studying here, for TB-mBJLDA). This sign change has been observed experimentally [191] for values around  $\delta \sim 0.20$ , in good agreement with the result obtained from our calculations. All these calculations were obtained for the parent undoped compound  $\text{La}_2\text{NiO}_4$  as a function of the chemical potential, what could be called a rigid-band approach. We will argue below how the picture is modified when VCA is applied.

### 5.3.3 VCA calculations

Once we have localized the position of the peak as a function of doping, we will study the evolution with hole-doping of the Seebeck coefficient (comparing it with available experimental data) and the other transport properties that can be calculated. In order to do that, we have performed VCA calculations (modifying the total number of electrons in the system to simulate the dopant concentration). Since we will be dealing with small doping levels ( $\delta \leq 0.15$ ), we will consider the ground state AFM configuration and also the structural properties of the parent compound. With this, we neglect the effects of the known orthorhombic distortion [202, 203] that occurs in this nickelate and would be a second order effect for the properties we try to estimate. The shape of the curves in Fig. 5.3 will not remain the same when VCA



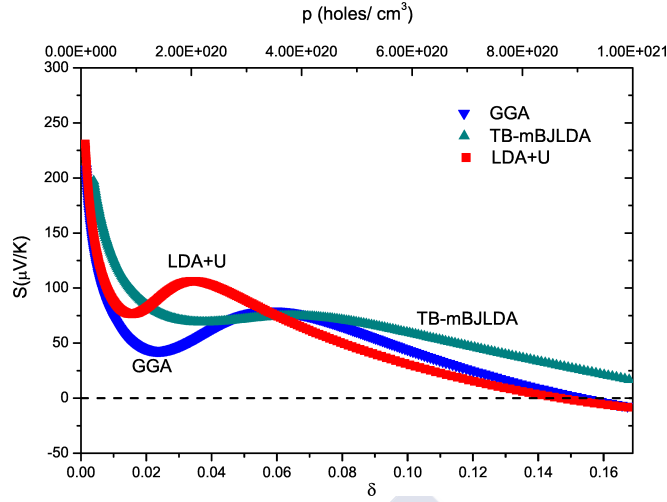


**Figure 5.4:** Calculated thermopower at  $T=400$  K as a function of hole doping in  $\text{La}_2\text{NiO}_{4+\delta}$  AFM within GGA, the LDA+ $U$  approach and TB-mBJLDA. A peak in a region close to  $\delta \sim 0.05$  is found for all the functionals. Negative thermopower is obtained for  $\delta > 0.15$ .

is applied because the effect of doping is not just a rigid band shift, but the existence of an optimum  $zT$  with doping remains true. Also, the more pronounced maximum in figure of merit at negative values of the chemical potential occurs for the LDA+ $U$  calculations, as we have seen in Figs. 5.3 and 5.4 and will further confirm below.

Figure 5.5 shows the thermopower at different doping levels calculated within the various exchange-correlation potentials we are using, and an additional figure with some experimental data from the literature. We can observe large values of the Seebeck coefficient for the most insulating samples, where the thermopower is above  $200 \mu\text{V}/\text{K}$  for the whole temperature range. The large Seebeck coefficient at low doping [191], is well predicted by all functionals. In every case, the maximum in  $zT$  occurs in the doping region of our interest ( $\delta \leq 0.15$ ) for values that coincide roughly with the maxima in thermopower vs.  $\delta$  at 400 K we analyzed in Fig. 5.4 (below  $\delta \sim 0.05$  within LDA+ $U$  and

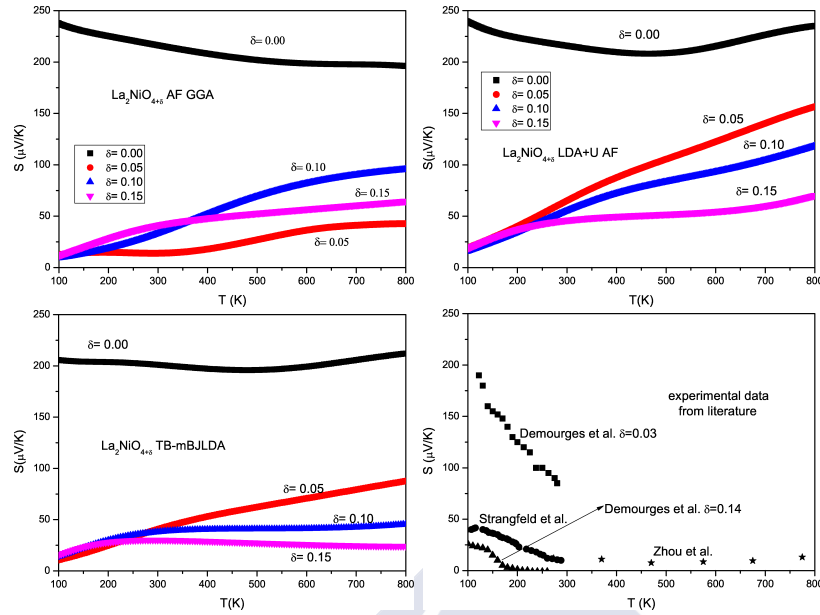


**Figure 5.5:**

Thermopower of  $\text{La}_2\text{NiO}_4$  AFM within GGA, the LDA+ $U$  approach and TB-mBJLDA and experimental values as a function of temperature for various values of the hole doping concentration  $\delta$  simulated using the virtual crystal approximation. Observe the different tendency with temperature for optimum-doping values (increasing at high temperature) and higher values of doping (oscillating with temperature and flat at the high temperature end). These tendencies are consistent with experiments (shown in the lower right panel).

at slightly higher values for GGA and TB-mBJLDA). For these “optimum” doping values the thermopower increases at high temperatures while for the other  $\delta$  values it shows an oscillating behavior and a flattening at higher temperatures, results that are compatible with most experiments available. The oscillating behavior of the thermopower with temperature that has been found in literature is particularly well described by a GGA calculation at  $\delta \sim 0.05$  and also TB-mBJLDA

at  $\delta \sim 0.10$ . According to our calculations, experiments showing thermopower oscillating with temperature (with a maximum at intermediate temperatures) have been obtained analyzing samples in that doping region (hole-doped, non-stoichiometric, even if some of them do not explicitly mention the oxygen content) [204–206]. However, an accurate placement of the maximum in the Seebeck coefficient as a function of temperature is not given by our calculations, that type of agreement being similar to what has been found in other correlated oxides [162]. Zhou *et al.*[204] have shown a slight increase in  $S$  at high temperature experimentally, but the exact  $\delta$  value of their samples is not provided; from our calculations we can argue that those samples would have a substantial  $\delta$ -value on the order of  $\delta \sim 0.15$ - $0.2$ . The best quantitative agreement between our calculations and those reported from experiments at low-doping levels can be obtained with the TB-mBJLDA functional. This was also found for the thermoelectric properties of CrN, when compared with experiments and with LDA+ $U$  calculations as we could see in Chapter 3. This functional provides a purely *ab initio* parameter-free description of the system, not depending on the choice of an arbitrary parameter.

In Fig. 5.6 we present the evolution with temperature of the thermoelectric figure of merit (electronic-only) for various doping levels. The figure complements the description given by the thermopower analysis alone, with similar conclusions. LDA+ $U$  values for  $\delta=0.05$  would be very promising in terms of the figure of merit obtained, even surpassing that of the undoped compound at high T. Also the values predicted by the parameter-free TB-mBJLDA functional would exceed  $zT=0.5$  at high temperatures for  $\delta=0.05$ . Uncorrelated GGA predicts an optimum hole-doping content at  $\delta=0.10$  with large figure of merit at high temperature. LDA+ $U$  also gives a very good response for  $\delta=0.10$  and  $0.15$ , especially due to a large increase at high temperature. From Figs. 5.6 and 5.4, focused at 400 K and carried out with a rigid-band approach, we expected a sharper behavior in  $\delta$ -values, but the VCA results show a broader range of efficient thermoelectric response being

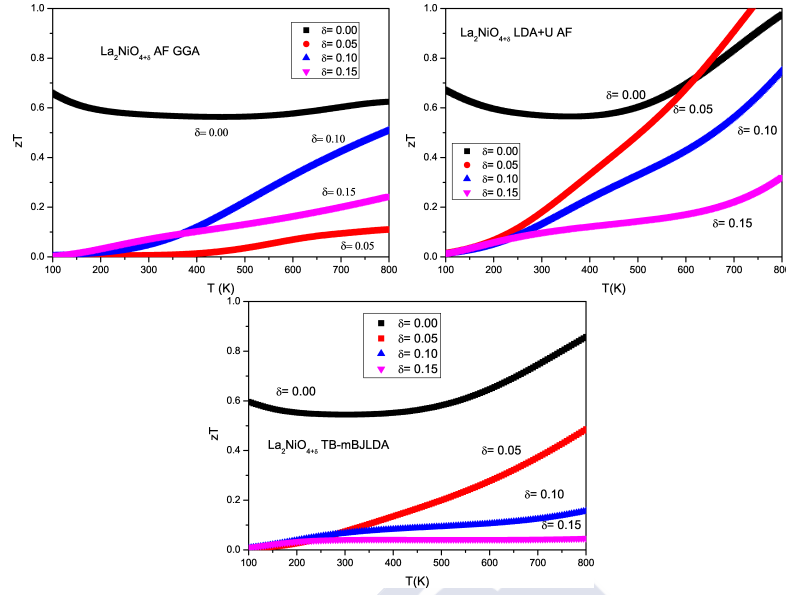


**Figure 5.6:**

Dimensionless figure of merit (electronic only) of  $\text{La}_2\text{NiO}_4$  AFM within GGA, the LDA+ $U$  approach and TB-mBJLDA as a function of temperature for various values of the hole doping concentration  $\delta$  calculated using the virtual crystal approximation. Observe the large high temperature figure of merit attainable at small doping values.

predicted. We have already discussed that the large  $zT$  of the  $\delta = 0$  case would need to be reduced by introducing a substantial  $\kappa_{ph}$ . This would be particularly important at  $\delta = 0$ . Being the system an insulator,  $\kappa_{ph}$  should be much higher than its electronic counterpart. Our calculations at  $\delta \neq 0$  should be more realistic, with the system approaching the metallic limit, specially if the thermal conductivity due to phonons can be further reduced by nanostructuring. This has been shown in the past to be a key ingredient in the design of high performance thermoelectric devices as we extensively explained in Chapter 1. In that case,  $\kappa_{el}$  could become more important compared to  $\kappa_{ph}$ , as discussed above. Let us give some rough numbers. According to our calculations (within GGA, not shown), the conductivity increases by a factor 20 at room

temperature for  $\delta = 0.05$  with respect to the stoichiometric compound, and by a factor 80 for  $\delta = 0.15$ , explainable by the increase in carrier concentration that is also given in Fig. 5.4. Also, if one can make thin films of the appropriate oxygen excess concentration, the conductivity can be made even larger, and the phonon thermal conductivity can be killed off by cutting away the long-wavelength phonon paths along the c-axis.

### 5.3.4 More realistic estimates

To further validate our results, we can give an estimate of the overall  $zT$  (up to now, we have studied the electronic part only). Considering the Wiedemann-Franz relation, the figure of merit can be rewritten as:  $zT = \sigma T S^2 / \kappa = \kappa_{el} S^2 / \kappa L_0$  being  $L_0$  the Lorenz number with a value for free electrons  $L_0 = 2.45 \times 10^{-8} (V/K)^2$  and  $\kappa_{el} \leq \kappa$  in general, but approaching 1 at large doping. At high enough temperatures, the lattice thermal conductivity term typically decreases as  $1/T$  (with the electronic term roughly temperature independent). This type of behavior was observed in experiments [194]. Taking the experimental values at the transition temperature for the thermal conductivity from [194] (that of course include both lattice and electronic contributions), the electrical conductivity from [193], and using our calculated values for the thermopower, we can obtain a more realistic estimate of the  $zT$  values for each functional at each doping level. The behavior of this estimated  $zT$  with temperature for the various doping levels and functionals used can be seen in Fig. 5.7. It can be observed that the shape of the curves for each functional remains roughly the same than in Fig. 5.6. The calculated electronic-only factor  $\sigma T / \kappa$  is not far from constant when the real band structure of the material is introduced in the calculations. However, the overall values of  $zT$  are reduced with respect to those obtained only with the electronic contribution in approximately one order of magnitude due to the phonon thermal conductivity.  $zT \sim 0.1$  is predicted from our calculations at high temperature if the proper

oxygen content is chosen. In any case, the growth in the form of thin films with the appropriate oxygen content would increase the electrical conductivity and reduce the phonon contribution to the thermal conductivity. Our results show that, in that case, the system could become promising for further research in terms of its thermoelectric properties, trying to find other oxides with performance comparable to that of layered cobaltates.

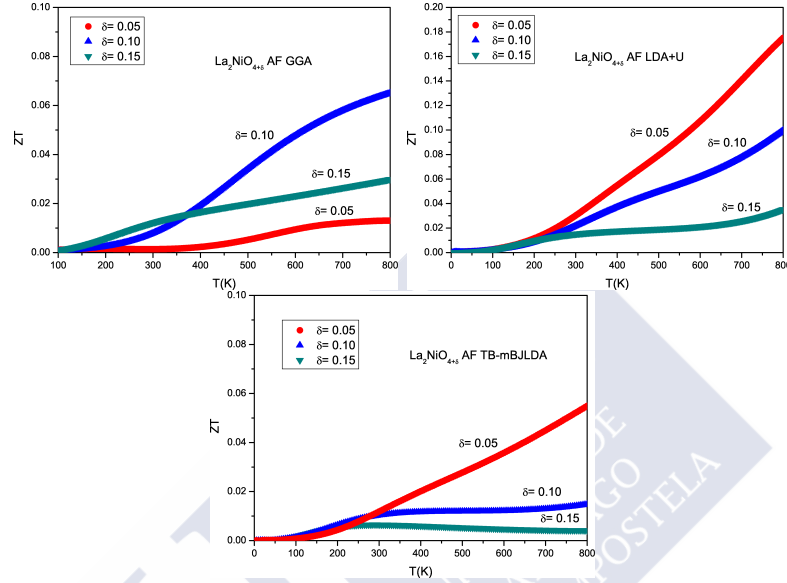
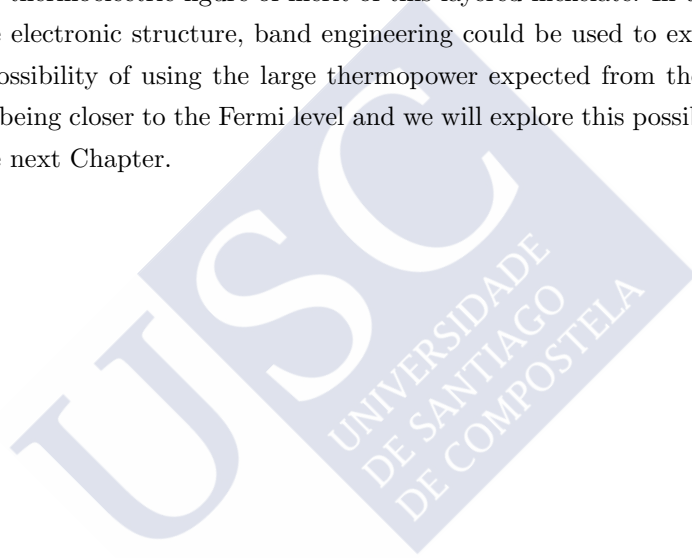


**Figure 5.7:** Thermoelectric figure of merit of  $\text{La}_2\text{NiO}_4$  AFM as a function of temperature for various values of the hole doping concentration  $\delta$  within GGA, the LDA+ $U$  approach and TB-mBJLDA estimated using the experimental values of  $\kappa$  and  $\sigma$ .

## 5.4 Summary

Our *ab initio* calculations for the compound indicate some promising features of hole-doped  $\text{La}_2\text{NiO}_{4+\delta}$  as a possible oxide thermoelectric

compound. If the thermal conductivity can be reduced by nanostructuring, e.g. in the form of thin films, the system could show an enhanced thermoelectric performance at low hole-doping levels, attainable by the appropriate control of the interstitial oxygen content. Our calculations show that a region with relatively large Seebeck coefficient exists in this compound at small doping levels, within the realistic AFM description. A careful experimental study needs to be performed in this respect controlling the oxygen content, and also making thin films with the appropriate oxygen composition. Hole-doping will increase the conductivity, as the thin film geometry does, which together with the reduction in thermal conductivity could leave room for an improvement of the thermoelectric figure of merit of this layered nickelate. In terms of the electronic structure, band engineering could be used to explore the possibility of using the large thermopower expected from the  $d_{z^2}$  band being closer to the Fermi level and we will explore this possibility in the next Chapter.







## Strain effects to optimize thermoelectric properties of hole-doped $\text{La}_2\text{NiO}_{4+\delta}$ via ab initio calculations

“

*The scientist is motivated primarily by curiosity and a desire for truth.*

*[Irving Langmuir]*

”

### 6.1 Introduction

We have seen that the appropriate oxygen excess  $\delta$  together with a thin film growth could significantly enhance the thermoelectric response in  $\text{La}_2\text{NiO}_{4+\delta}$ . From our results, we proposed band engineering as a possible mechanism to further enhance its thermoelectric response.

As we saw in the Introduction, strongly correlated electron systems are potentially good thermoelectrics since they provide additional ingredients that allow to tune the band structure to try to optimize separately the different magnitudes involved in the thermoelectric response (TE): having localized electrons, allowing for the tuning of band

splittings, band widths, etc. Moreover, band engineering is possible in order to tune the electronic structure for an enhanced thermoelectric response, i.e. they are flexible to a modification of their band structure not only through doping or nanostructuring but also using strain, ordering phenomena, electron localization mechanisms, pressure effects, etc. that commonly play a big role in their electronic structure [207]. Strain engineering has recently been shown as a direct method to control the thermoelectric properties in thermoelectric topological insulator materials  $Bi_2Se_3$  and  $Bi_2Te_3$  [208].

Having this and our results from Chapter 5 in mind, we will analyze here how one can refine even further the thermoelectric properties of  $La_2NiO_{4+\delta}$ , when both oxygen-excess and strain are introduced [209]. We will perform a band engineering study of how strain effects, attainable experimentally via thin film growth, can enhance the thermoelectric performance in a  $3d$  electron system that has been predicted to yield an interesting thermoelectric response. The goal would be designing the proper growth conditions for an improved efficiency.

## 6.2 Computational Procedures

For the exchange-correlation functional in the structural relaxations we have used the Perdew-Burke-Ernzerhof version of the generalized gradient approximation (GGA). To study the effects of strain, we have analyzed different in-plane  $a$ ,  $b$  lattice parameters, and for each of them the  $c$  parameter was calculated. We have optimized also the value of the  $c$ -parameter for each  $a$ ,  $b$  in-plane lattice parameters presented. Consequences will be drawn for strains in thin films but the actual calculations are done in bulk-like unit cells with tetragonal symmetry for various  $c/a$  ratios.

For the calculations of the transport properties, we have used the Tran-Blaha modified Becke-Johnson (TB-mBJLDA) potential that in the previous Chapter has been shown to yield the best results for this material.

For the transport properties, denser k-meshes are required, up to  $40 \times 40 \times 15$  to reach convergence.

Again, the simulation of different doping levels was performed in two different ways: i) by a shift in the chemical potential for the undoped compound, calculating the hole concentration at each temperature (we have seen in the previous Chapter that the essential features and trends can be obtained by this method), ii) using the virtual crystal approximation (VCA), that provides a more accurate description of the doped material and yields substantial differences in quantitative values of the thermoelectric properties, as we will discuss in detail below.

In this particular case, we used  $R_{mt}K_{max} = 7.0$ , a k-mesh of  $10 \times 10 \times 4$ , and muffin-tin radii of 2.35 a.u. for La, 1.97 a.u. for Ni and 1.75 a.u. for O.

## 6.3 Results

### 6.3.1 Revisiting the electronic structure and magnetic properties of unstrained $\text{La}_2\text{NiO}_4$

Let us recall some basic ideas about the electronic structure of  $\text{La}_2\text{NiO}_{4+\delta}$ . This is a compound containing  $\text{Ni}^{2+}:\text{d}^8$  cations in a largely elongated octahedral environment. The crystal field splittings in such geometry lead to a breakup of the  $e_g$  degeneracy with the  $d_{x^2-y^2}$  band higher in energy than the  $d_{z^2}$  (as sketched in Fig. 6.1a). A significant Hund's rule coupling stabilizes the high-spin state (HSS)  $t_{2g}^6 e_g^0$  ( $S=1$ ). In the previous Chapter it was seen that hole-doping via oxygen excess introduces holes in the Ni  $d_{x^2-y^2}$  band, which is somewhat localized. This  $d_{x^2-y^2}$  band below the Fermi level can be substantially modified in a process one can call "band engineering" in order to improve the thermoelectric response of the compound. For that sake one needs, e.g. a larger thermopower (proportional to the derivative of the density of states (DOS), and hence increasing with a reduced bandwidth) without compromising electrical conductivity. One possibility for that is

to bring the  $d_{z^2}$  band (whose bandwidth is smaller due to the comparably smaller off-plane hopping) closer to the Fermi level, and make use of its reduced band width to enlarge the thermopower. Of course, this is not exactly so because, as mentioned above, the electronic-only magnitudes in semiconductors are all closely related, and in principle a reduced band width might lead to an increased band gap and a reduction of the conductivity. Yet an optimum performance can be sought, as we will see below. In any case, to bring the  $d_{z^2}$  higher in energy (closer to the Fermi level for the majority spin channel), this band needs to be destabilized with respect to the  $d_{xy}$  (which itself is split from the lower-lying  $d_{xz}/d_{yz}$  doublet) and  $d_{x^2-y^2}$  bands (see Fig. 6.1). Thus, enlarging the a,b plane could produce the required effect. This would, however, significantly reduce the in-plane conductivity, which is the largest component in this layered compound, with the corresponding fall-out in figure of merit (let us recall,  $zT = \sigma S^2 T / \kappa$ ).

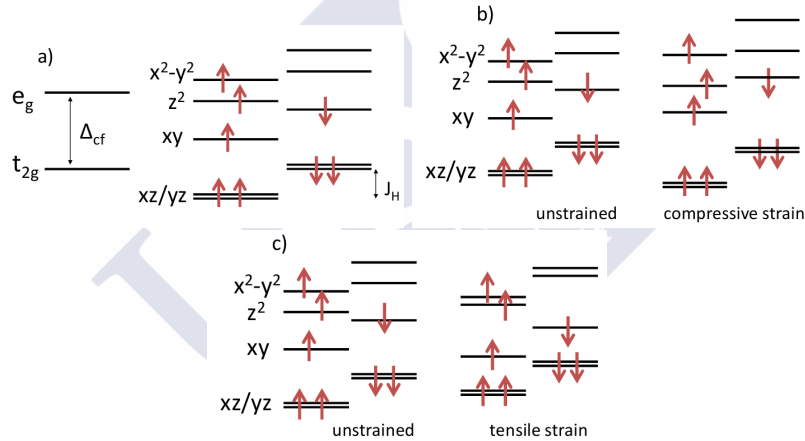


**Figure 6.1:**

Sketch of the crystal field levels of a  $Ni^{2+}:d^8$  cation in a HS state to observe the effects of: a) a distortion below octahedral symmetry in an elongated octahedron, and the effects of both compressive (b) and tensile (c) strain. The gap is expected to be reduced (increased) for the compressive (tensile) strain case.

If, however, a,b lattice parameters are reduced,  $\sigma$  can be increased, but the  $d_{x^2-y^2}$  band will be moved up in energy so that it will remain the only accessible band via hole-doping (a sketch of how all these bands shift with strain can be seen in Fig. 6.1). In that case, the band will become broadened (lower peaks for the DOS, smaller thermopower) by the increased in-plane hopping caused by the smaller lattice parameter. Hence, there will be optimum values (a compromise) for both strain and doping (trying to tune the oxygen excess to reach the chemical potential where thermopower is maximized) that one could use for designing thin films with optimal conditions so that an enhanced TE response can be obtained. Changes in the in-plane lattice parameters are induced by growing epitaxial thin films on different substrates. As explained above, a thin film geometry is beneficial for the overall TE response since  $\kappa$  will be drastically reduced and  $\sigma$  has been observed to increase due to its large two-dimensional anisotropy [193].

Concerning the magnetic order, we will focus our calculations in the doping level region  $\delta < 0.15$ , where magnetic order exists as we discussed in Chapter 5. All our calculations assume an in-plane checkerboard AFM ordered phase.

### 6.3.2 Changes in the electronic structure caused by strain

We have performed calculations at various in-plane lattice parameters, that try to simulate both compressive and tensile strains caused by growth of  $\text{La}_2\text{NiO}_{4+\delta}$  thin films on top of different substrates. Calculations are carried out in bulk-like unit cells but help us draw conclusions about the changes in the electronic structure undergone by the compound if grown epitaxially on top of different substrates, with different in-plane strains and c/a ratios.

We have optimized the out-of-plane c lattice parameter of the structure for each value of the in-plane a, b lattice parameters chosen. We have performed GGA calculations for several values of the in-plane

**Table 6.1:**

In-plane vs. out-of-plane optimized lattice parameters for various strains. A compression in the  $xy$ -plane leads to an elongation in  $c$  to try to keep the volume constant.

$a$ (Å)	$c$ (Å)
3.73	13.27
3.84	12.70
3.93	12.51
4.00	12.33
4.10	12.03

lattice parameters from 3.7 to 4.1 Å. The bulk value of the  $a$  lattice parameter in the tetragonal structure [182] of  $\text{La}_2\text{NiO}_4$  is 3.89 Å (on a  $\text{SrTiO}_3$  substrate, it would be roughly unstrained). For each  $a$ ,  $c$  combination, the atomic positions were relaxed and the minimum-energy  $c$ -value was obtained for each in-plane area. In Table 6.1 we can see the results of the lattice parameter optimizations.

We know from the previous Chapter and the discussions above that the only band available in unstrained  $\text{La}_2\text{NiO}_{4+\delta}$  (with  $\text{Ni}^{2+}:\text{d}^8$   $S=1$ , HSS) to be populated with holes via oxygen excess is the majority-spin  $d_{x^2-y^2}$  band. Compressive strain (reducing the in-plane lattice parameter) will move this  $d_{x^2-y^2}$  band further up in energy but at the same time it will increase its bandwidth (together, an increase in conductivity and decrease in the derivative of the DOS, and hence a reduction of the thermopower, is expected). If, on the other hand tensile strain is applied, this band moves further down in energy (it gets stabilized by the larger in-plane lattice parameter) closer to the energy window where the majority  $d_{z^2}$  band and the minority  $t_{2g}$  bands reside. Thus, the effects of applying a tensile strain are slightly more complicated because more bands are involved. Moreover, tensile strain would reduce the in-plane conductivity (due to the larger in-plane lattice parameter) but could enlarge the Seebeck coefficient if a large DOS is retained close to the Fermi level (accessible via hole-doping).

Figure 6.2 shows the band structure for the two types of strain studied: compressive and tensile. We see that compressive strain (on the left) reduces significantly the band gap, driving the system towards a bigger in-plane conductivity caused by the reduced Ni-Ni in-plane distance and corresponding increase in the Ni  $d_{x^2-y^2}$  bandwidth (larger in-plane hopping mediated by those orbitals via a large  $\sigma$ -bond with oxygens). The  $d_{x^2-y^2}$  band is significantly less wide in the right panel (tensile strain) due to the reduced hopping caused by the enlarged in-plane lattice parameter. Moreover, tensile strain leads to a stabilization of the  $d_{x^2-y^2}$  band, that places it closer to all the other occupied bands (we see the band very distinctly below the Fermi level in the compressive strain case, where the opposite is true, but somewhat mixed with many other bands for the tensile one).

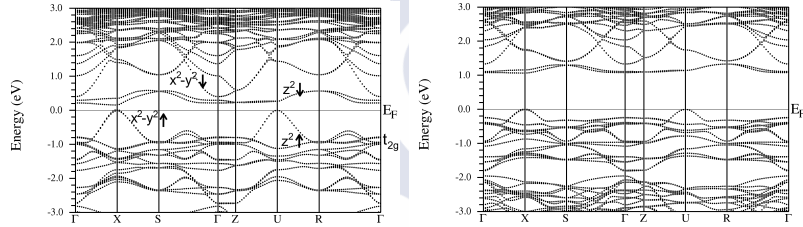


**Figure 6.2:**

Band structure (calculated within GGA) for two types of strain: compressive on the left ( $a= 3.74 \text{ \AA}$ ) and tensile on the right ( $a= 4.11 \text{ \AA}$ ). Notice the displacement of the  $d_{x^2-y^2}$  band (easy to identify with maxima at X and U, being 1 eV wide, and occurring just below the Fermi level specially in the left panel) to a lower position in the tensile strain case. A significant reduction of the gap occurs for the compressive strain case and a somewhat smaller band width of the  $d_{x^2-y^2}$  band in the tensile strain case.

There are various factors at play here that can enhance or reduce the different TE properties: conductivity and thermopower. Thus, calculations need to be performed to account for them all (doping, strain, changes in bandwidth, introduction of more bands near the Fermi level, etc.) properly. All in all, we have various conflicting parameters to tune

and calculations are required to see the balance between them in order to obtain a compromise that might enhance the TE response.

### 6.3.3 Influence of strain on the thermoelectric properties

We can quantify all the important magnitudes for the TE response of a material in terms of the dimensionless TE figure of merit  $zT = \sigma TS^2 / \kappa$ . As mentioned above,  $zT$  needs to be larger than 1 for applications. As extensively explained in Chapter 5, we can, from first principles calculations through the electronic structure of the material, give an estimate of the electronic part of the figure of merit. However, again, for the thermal conductivity,  $\kappa = \kappa_e + \kappa_{ph}$ , we can only estimate the electronic part, which becomes more important in the itinerant electron limit. In the localized limit,  $\kappa_{ph}$  (the component due to the lattice) will be the only important contribution. Our results obtained from electronic structure calculations will be an upper limit for the overall  $zT$ , but still helpful to understand how to optimize and engineer a better response in this and other related systems. We will again try to give a more realistic estimate of  $zT$  using the experimental value of  $\kappa$  in the last part of this Chapter.

The first parameter to analyze the TE response of the material is the Seebeck coefficient, that can be calculated independently of the scattering time in the constant scattering time approximation we are using for our calculations. Figure 6.3 shows the thermopower calculated for three values of hole doping in  $\text{La}_2\text{NiO}_{4+\delta}$ :  $\delta = 0.05, 0.10$  and  $0.15$ , for several values of the lattice parameter from  $3.74$  to  $4.11 \text{ \AA}$ , that simulate both the compressive and tensile strain limits (let us recall the unstrained value of the in-plane lattice parameter is  $3.89 \text{ \AA}$ ). Results are presented using VCA (lower panel) for simulating doping or just displacing the chemical potential for the calculations in the undoped compound (upper panel). The values of doping chosen are, as explained above, in the range where the AFM ordering survives and



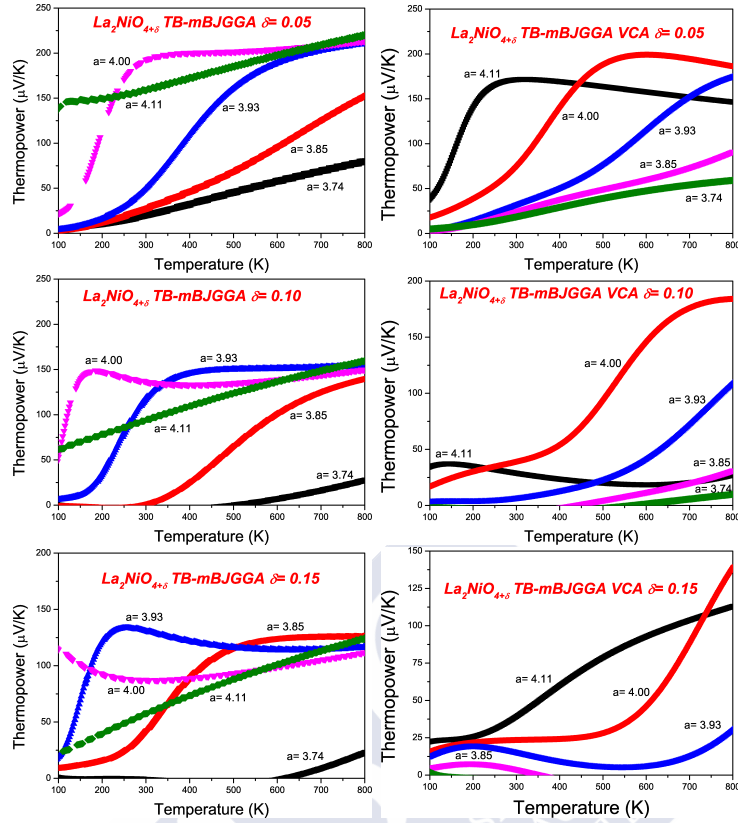


**Figure 6.3:**

Thermoelectric power of  $\text{La}_2\text{NiO}_{4+\delta}$  as a function of temperature for three doping values:  $\delta = 0.05$ ,  $\delta = 0.10$  and  $\delta = 0.15$  for various values of the in-plane lattice parameter (different strains). The left panels show calculations for undoped  $\text{La}_2\text{NiO}_4$  shifting the chemical potential to the desired carrier concentration, whereas the right panels were calculated using the VCA. The latter yields a more reliable and accurate description of the system. The exchange-correlation potential used was TB-mBJLDA. Observe that for various lattice parameters in the doping range  $\delta = 0.05 - 0.10$ , thermopower exceeding  $150 \mu\text{V/K}$  are predicted.

our calculations are more reliable, and also the interval where it was predicted the enhancement in TE figure of merit with doping for the unstrained compound (see Chapter 5). It was seen in previous studies [191] that large thermopower occurs for  $\delta = 0$  and then gets rapidly

reduced as doping is introduced. Here we can analyze in more detail the effects of such doping levels in the thermopower together with the effect of strain.

Looking at Fig. 6.3, one can see that in the tensile strain region ( $a > 3.90 \text{ \AA}$ ) the thermopower is enhanced, whereas in the compressive strain region it is reduced. This is the expected result because, as we have discussed above, enlarging the xy-plane leads to a wider gap and hence the thermopower will increase. We see that, as doping is increased, things get slightly more complicated than that, at the same time that thermopower is reduced. Putting everything together, values of the thermopower at room temperature in the range of  $S \sim 150 \mu\text{V/K}$  are predicted up to  $\delta = 0.10$  in the tensile strain regime. We observe in the right panels of Fig. 6.3 that the results using the VCA differ substantially in quantitative terms (some vague trends are maintained, but the values are very different to those obtained shifting the chemical potential in the undoped compound). We argue that using the VCA here, for these substantial doping levels, is necessary to yield a correct description of the system. We can see that the two methods give more similar accounts at low-doping ( $\delta \sim 0.05$ ), where shifting the chemical potential in the calculation for the undoped compound is enough to describe more or less accurately the system (it will work even better for  $\delta < 0.05$ ), but going to larger doping levels, one needs to include the change in the overall potential caused by the oxygen excess in the system to get a good description. In the VCA-based calculations, we see that as doping increases, the values of the thermopower decay quite fast, except at high temperatures. But even at high temperatures, the lattice parameter window where the response is promising becomes narrower, around  $4.00 \text{ \AA}$ . Focusing on that tensile strain value, we see that the values of the thermopower at room temperature are not promising:  $75 \mu\text{V/K}$  at  $\delta = 0.05$ ,  $40 \mu\text{V/K}$  at  $\delta = 0.10$  and only  $25 \mu\text{V/K}$  at  $\delta = 0.15$ , yet the high temperature response becomes enhanced. It has been observed experimentally that  $\text{La}_2\text{NiO}_{4+\delta}$  has an increasing thermopower at high temperatures [204, 206].

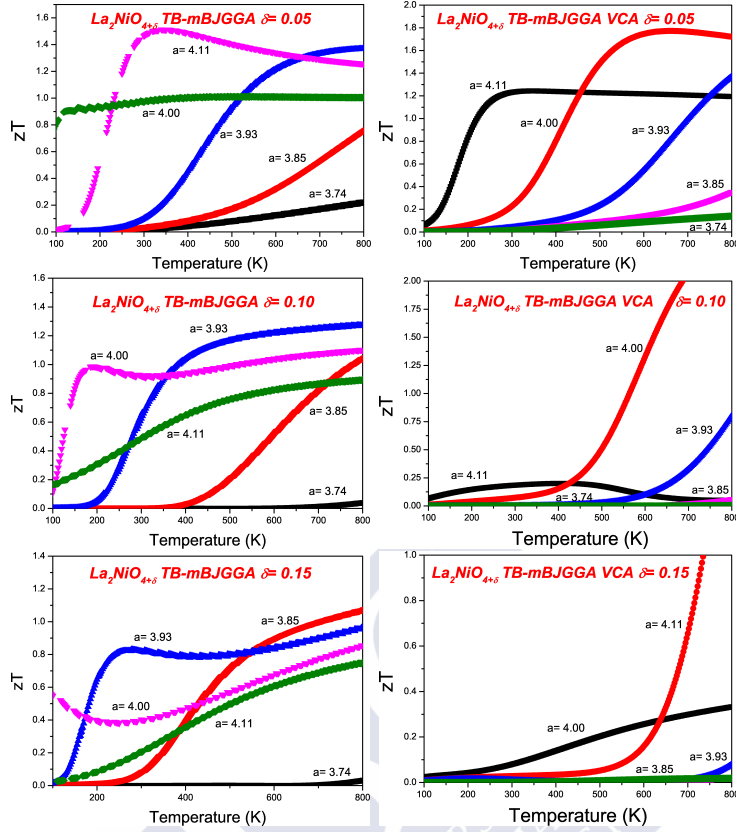


**Figure 6.4:**

Figure of merit of  $\text{La}_2\text{NiO}_{4+\delta}$  as a function of temperature for three doping values:  $\delta = 0.05$ ,  $\delta = 0.10$  and  $\delta = 0.15$  for various values of the in-plane lattice parameter (different strains). The left panels were calculated for an undoped  $\text{La}_2\text{NiO}_4$  shifting the chemical potential to the desired carrier concentration, whereas the right ones were obtained using the VCA. The latter yields a more reliable and accurate description of the system. The exchange-correlation potential used for calculating all the transport properties was TB-mBJLDA. Observe that for various lattice parameters in the doping range  $\delta = 0.05 - 0.10$ , the electronic figure of merit exceeds unity.

However, we know that the larger the  $a$  parameter is, the wider the band gap gets (and that is why even upon doping large thermopower values can be obtained) but the conductivity will be reduced (in-plane

hopping decreases). We can compile both effects in the calculation of the dimensionless TE figure of merit, that is presented in Fig. 6.4 for several doping levels and lattice parameters (the same ones we have used for the thermopower) and with the same calculation schemes described above. We see at low-doping, around  $\delta=0.05$  and for a slight tensile strain ( $a > 3.90 \text{ \AA}$ ), values of the electronic-only TE figure of merit exceeding unity can be obtained even at room temperature for the larger lattice parameters tested, and at high temperatures for a very small tensile strain. Moving the system towards the compressive strain limit, even though in principle it should increase the conductivity, the gain through that term does not win over the loss in thermopower (which is substantial, as we saw above). We can see again that neglecting VCA and just shifting the chemical potential in the undoped compound will produce a large overestimation of the TE figure of merit (but the agreement with VCA is again better at small doping). As doping is increased, as we saw for the thermopower, a promising TE response only occurs at large temperature and for a very critical range of in-plane lattice parameters (around  $a=4.00 \text{ \AA}$  for  $\delta=0.10$  and  $a=4.11 \text{ \AA}$  for  $\delta=0.15$ ). This means that one has to optimize doping for each strain analyzed to obtain a significant TE figure of merit. For the larger tensile strain considered ( $4.11 \text{ \AA}$ ), the behavior is quite peculiar, not being monotonic with doping. The large lattice parameter window with electronic-only figure of merit exceeding unity in the tensile strain limit occurs for small values of doping around  $\delta=0.05$ .

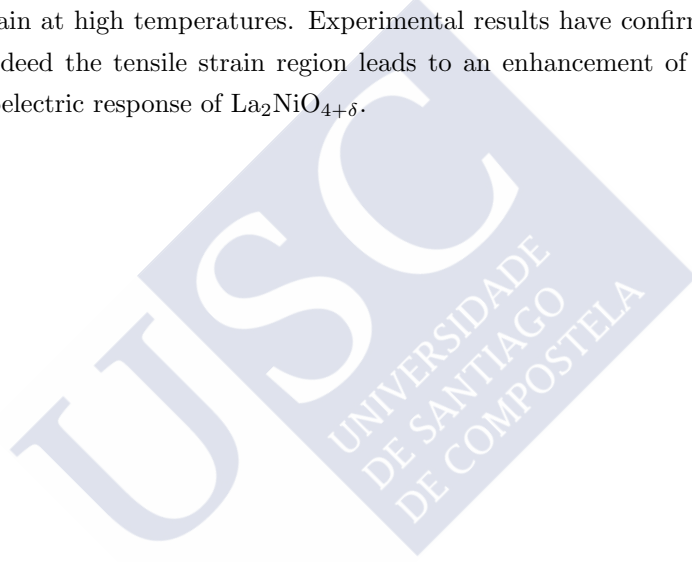
To further validate our results, we can give an estimate of the overall  $zT$  (up to now we have studied the electronic part only) as we did in Chapter 5. Considering the Wiedemann-Franz relation, we saw that the figure of merit can be rewritten as  $zT = \sigma TS^2 / \kappa = \kappa_e S^2 / \kappa L_0$ ,  $L_0$  being the Lorenz number with a value for free electrons  $L_0 = 2.45 \times 10^{-8} (V/K)^2$ . Taking again the experimental values for the thermal conductivity of the unstrained compound at the transition temperature [194], the electrical conductivity [193], and using our calculated values for the thermopower, we can obtain an estimation of the values of the


overall  $zT$ . At 400 K, for  $a=4.11 \text{ \AA}$ , a  $zT$  of 0.3 can be achieved for  $\delta=0.05$  while for  $\delta=0.15$  only a figure of merit of 0.04 can be obtained. For  $\delta=0.10$  and  $a=4.00 \text{ \AA}$ , a lower value of 0.02 is estimated at 400 K. However, at high temperatures (above 700 K),  $zT$ s close to one ( $\sim 0.8$ ) can be obtained for  $a=4.00 \text{ \AA}$  and values of doping between 0.05 and 0.10. This value of  $zT$  is eight times larger than the one obtained at high temperature for the compound hole-doped only without strain applied. Hence, as expected, band engineering shows up as a good method to increase the thermoelectric efficiency of this nickelate. The obtained  $zT$  values are already very promising but, again, if the thermal conductivity of the system can be reduced with respect to the bulk value when grown in a thin-film geometry, our calculations suggest that values of  $zT$  beyond one could in principle be achieved.

As we have been arguing, one possible route to reduce the thermal conductivity is the growth in thin films. It has been recently observed how oxygen non-stoichiometries can lead to a significant reduction of the thermal conductivity by creating new scattering centers that would hamper phonon propagation in  $\text{SrTiO}_{3-\delta}$  thin films at very low doping levels [210, 211]. The recipe for  $\text{La}_2\text{NiO}_{4+\delta}$ , according to our calculations, would be the growth in thin films with oxygen excess on the order of  $\delta \sim 0.10$ , grown on top of a substrate that provides some tensile strain, and studied at high temperatures, where the most plausible applications of this oxide and the larger figure of merit will occur. Very recently, experiments have been performed and confirmed our predictions [212]. They show that indeed tensile strain leads to an enhancement of the thermopower but not only that, this enhancement is independent of variations of the resistivity so it is possible to decouple the often inter-related transport coefficients by controlling the epitaxial growth.

## 6.4 Summary

Our *ab initio* calculations for the compound indicate some promising features in hole-doped  $\text{La}_2\text{NiO}_{4+\delta}$  under strain as a possible oxide thermoelectric material. Our calculations show that a region with relatively large Seebeck coefficient exists in this compound at small doping levels and the appropriate tensile strain, within the realistic AFM description. To enhance the thermoelectric response, our calculations show that the region of tensile strain should be explored, growing on substrates with a lattice parameter slightly larger than that of  $\text{SrTiO}_3$  (about 3.95 - 4.05 Å) predicting a reasonable thermoelectric performance (with figure of merit close to 1,  $zT \sim 0.8$ ) in those conditions of doping and tensile strain at high temperatures. Experimental results have confirmed that indeed the tensile strain region leads to an enhancement of the thermoelectric response of  $\text{La}_2\text{NiO}_{4+\delta}$ .





## Surface electric dipole formation in CrN(001) very thin films

“Do not fear to be eccentric in opinion for every opinion now accepted was once eccentric

[Bertrand Russell]

### 7.1 Background

In the two previous Chapters we have explained how a thin film geometry can lead to an enhanced thermoelectric response with respect to the material in its bulk shape in the particular case of a nickelate. But the manipulation of the electronic structure of a material via quantum confinement and dimensionality reduction has been shown to lead to many other electronic-structure related properties different from the ones of their three-dimensional precursors becoming one of the most prolific areas in the field of Materials Science nowadays. An exciting opportunity is to study interfaces and surfaces of materials that even in its bulk form exhibit functional properties. This is what we will do

in the next two Chapters with a material already studied in the present Thesis, CrN. We will also have the goal of shedding some light into the controversies concerning its electronic properties described in Chapter 3. Here we will study the changes in electronic structure this material experiences when grown on a thin film geometry and in Chapter 8 how its properties get modified when sandwiched between the band insulator MgO.

As explained in Chapter 1, the reduced symmetry at the surface of a crystalline solid allows for new phenomena to be observed, which are not possible in the bulk with the effects of shapes and boundaries becoming crucial. Surface reconstructions lead to new electronic phenomena where all the electronic, spin and orbital degrees of freedom become active and interact differently than in the case of the bulk. For instance, surface effects caused by vacancies produced mechanically have been shown to yield a 2D electron gas confined to a nanometric surface layer in SrTiO<sub>3</sub> [30]. Hence,

As we have extensively explained in detail in Chapter 3, the nature of the transition in CrN in terms of the electrical conduction behavior has had a wide range of interpretations in the literature. We saw that the material as a bulk is always semiconducting, but being very close to a metal-insulator transition. Hence, the suspicion that small perturbations like doping, pressure or thin-film deposition could drastically change its conduction properties is justified. Experimentally, we saw that the nature of the transition in thin films is modified with respect to the case of the bulk: the low-temperature phase is found to be metallic in various works and under different growth conditions.

To elucidate the origin of the experimentally found metallic behavior in the low-temperature phase, whether it can be intrinsic or not, and also what the effects of the material being so close to a metal-insulator transition are when it is nanostructured in the form of thin films, we will study in this Chapter the electronic and magnetic properties of free-standing CrN thin films by using first principles electronic structure methods. Our goal is to analyze the changes in electronic



structure with respect to the material as a bulk, determine the relaxed equilibrium structures and the appearance of new electronic states and its origin as a consequence of nanostructuring [213].

## 7.2 Computational details

To deal with strong correlation effects, we apply the LDA+ $U$  scheme incorporating the on-site Coulomb repulsion  $U$  and Hund's rule coupling strength  $J_H$  for the Cr  $3d$  states, taking a  $U = 4$  eV value and setting the on-site Hund's exchange parameter  $J_H$  to zero. Such a value has been shown to be reliable for CrN bulk based on the agreement with photoemission experiments and transport properties, the comparison between band structure parameters and optical data, and a comparison with parameter-free functionals as we saw in Chapter 3. In this case, for the structural relaxations we have used the Perdew-Burke-Ernzerhof version of the generalized gradient approximation (GGA). Since  $U$  could in principle vary significantly on a surface, we have chosen a truly *ab initio* GGA-scheme for the structural relaxations.

All calculations were fully converged with respect to all the parameters used. In particular, we used  $R_{mt}K_{max} = 7.0$ , and muffin-tin radii of 1.95 a.u. for Cr, and 1.73 a.u. for N.

## 7.3 Results

### 7.3.1 Unit cell details.

We investigate the changes in the electronic structure that occur when nanostructuring CrN in the form of free-standing thin films. We have modeled 4-, 6-, 8- and 10- layer thick films grown along the (001) direction starting from both the experimentally observed low-temperature orthorhombic and the high-temperature cubic (rocksalt) bulk unit cells. For all the cases we have performed calculations keeping the bulk positions fixed (non-relaxed cases) or with fully relaxed atomic positions

(relaxed cases). Cubic lattice parameters would be the situation of a film on top of a cubic substrate whereas the orthorhombic lattice parameters would allow the relieve of exchange-related stress. For the orthorhombic unit cell, the optimized bulk cell parameters used as starting point to create the supercells were:  $a= 5.774 \text{ \AA}$ ,  $b= 2.973 \text{ \AA}$ ,  $c= 4.146 \text{ \AA}$ . For the cubic films, we have used as starting point the experimental cell parameter obtained by Corliss *et al.*[104]  $a= 4.134 \text{ \AA}$ . A vacuum of  $15 \text{ \AA}$  was used for all the calculations, after checking that it is enough to guarantee the lack of interaction between CrN blocks (see Fig. 7.1a). In-plane AFM order was imposed and in order to allow for this type of ordering within one plane, an in-plane  $\sqrt{2} \times \sqrt{2}$  supercell was constructed. Note that this imposed in-plane checkerboard AFM ordering is not the bulk CrN (AFM2) structure, since this would require larger supercells. However, we have checked other magnetic structures (such as G-type) and the effects of a particular magnetic order on our conclusions are minor.

### 7.3.2 Ionic model.

As happened for the bulk, a first picture of the possible electronic configuration of the material can be obtained from an ionic model. In the case of the films, two different types of Cr environments should be distinguished: octahedral for the inner Cr atoms and square pyramidal for the surface Cr atoms. In a square pyramidal environment caused at the surface by the absence of one apical nitrogen (surface termination is depicted in Fig. 7.1), the degeneracy of the octahedral  $t_{2g}$  levels is lifted with the  $d_{xz,yz}$  orbitals lying lower in energy. The degeneracy of the  $e_g$  levels is also lifted, lowering in energy the  $d_{z^2}$  orbital. (see Fig. 7.1b). Again, the average valence for the Cr cations is +3. The electronic configuration as well as the chosen in-plane AFM order can be observed in Fig. 7.1c. For both the octahedral and square pyramidal Cr atoms in a high-spin state ( $S = 3/2$ , magnetic moment of  $3 \mu_B$ ), the orbitals  $d_{xz,yz,xy}^\uparrow$  are completely filled while the minority  $d_{xz,yz,xy}^\downarrow$  remain empty,

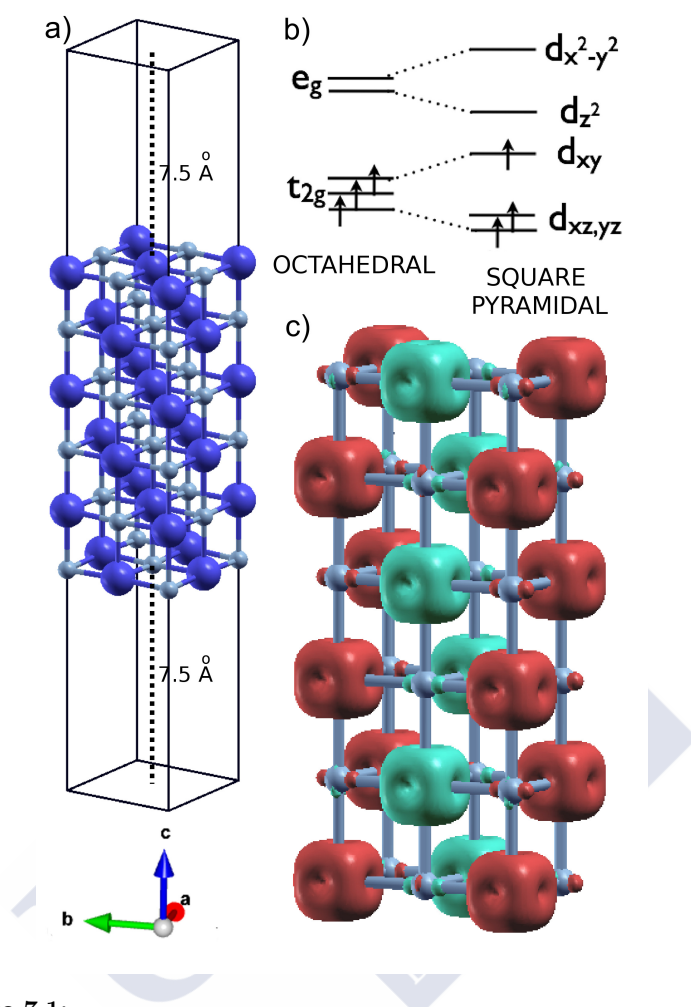


**Figure 7.1:**

(a) Unit cell of the orthorhombic 6-layer CrN film with the N atoms (smaller) in gray and the Cr atoms (larger) in blue. (b) Level schemes representing the electronic structure of a Cr<sup>3+</sup> cation in an octahedral environment (left) and in a square pyramidal one (right). The splitting of both e<sub>g</sub> and t<sub>2g</sub> levels in a square pyramidal environment can be observed. (c) Three-dimensional plot showing the difference between the spin-up and spin-down (different color/grayscale) electron densities. The in-plane AFM order chosen for the calculations can be seen. The typical d<sup>3</sup>(t<sub>2g</sub>-like) electronic configuration of each Cr<sup>3+</sup> cation and the small magnetic polarization of the neighboring ligands can be observed.

with the  $d_{x^2-y^2, z^2}$  states for both spin channels also completely empty above the Fermi level. The competition between crystal-field splitting and Hund's rule coupling strength will dictate what the first unoccupied states are (whether  $t_{2g}^\downarrow$  or  $e_g^\uparrow$ ). Moreover, at the surface, it is important to understand the relative value of the splittings within the  $t_{2g}$  and  $e_g$  multiplets due to the reduced symmetry, with respect to the Hund's rule coupling strength and the octahedral  $t_{2g}$ - $e_g$  crystal-field splitting. These values could be such that there exist band crossings and metallic states arising due to the surface coordination of the Cr atoms. Just focusing on the majority spin-channel, if the  $t_{2g}$ - $e_g$  crystal-field splitting is on the order of the splittings inside the  $t_{2g}$  and  $e_g$  manifolds caused by the surface dangling bonds, bands coming from the surface Cr atom could cross at the Fermi level leading to a conducting state with strong surface Cr-d character. This would be an interesting conducting state confined to the surface. However, we will see below that crystal-field splittings at the surface are not the only effect that displaces the bands with respect to the bulk case, the effects of surface atomic relaxations play a role as well in very thin films.

### 7.3.3 Evolution with thickness.

CrN with an in-plane AFM ordering is a low band-gap material. Eventually nanostructuring in thin films will reorganize the bands around the Fermi level, with the possible appearance of surface states, as we described above. It is interesting to analyze the evolution of the band gap and the band structure in general in the different structures we have calculated. Looking at Table 7.1 one can see that the tendency of the films towards metallicity is increased by the orthorhombic distortion. In the insulating cases, the band gap can be obtained as the difference between the eigenvalues at  $\Gamma$  (bottom of the conduction band) and  $M$  (top of the valence band). If we keep this picture in mind, the evolution of the band gap can be extended to the metallic phase as the same difference between eigenvalues but in that case with negative values.

Hence, it can be seen how, for the cubic case, the relaxed 10-layer film is metallic and for the orthorhombic ones, already the 6-layer film is metallic with the tendency towards metallicity increasing as the number of layers does (with a band gap of -14 meV for the 6-layer case and -225 for the 10-layer one). The values of the band gap are always one order of magnitude higher for the cubic structures with respect to the orthorhombic ones. The non-relaxed structures remain insulating for both the cubic and orthorhombic films although the last ones are closer to metallicity with very small values of the band gap (from 4 to 18 meV). The structural relaxation increases the band gap for the thinner films (for the 4-layer cubic case, from 119 to 206 meV and for the orthorhombic, from 4 to 34 meV) and drastically decreases it for the thicker films. It is interesting to note that, contrary to most other correlated insulators, a structural relaxation does not favor the opening of a gap in the case of CrN thin films. This is quite peculiar and suggests that the formation of conducting states in a thin-film geometry is particularly favored energetically and will be directly connected to surface reconstructions. We will see below that the 4-layer system is different because being so thin, the structural relaxations do not allow for an accommodation of the surface Cr in its 5-neighbor environment as it does for the thicker films.

The evolution of the band structure within the LDA+ $U$  method ( $U= 4$  eV) with film thickness using the fully relaxed positions for the orthorhombic (distorted) structure is presented in Fig. 7.2. We have chosen an in-plane k-path  $\Gamma(0, 0, 0)$ -  $M(\pi/a, 0, 0)$ -  $X(\pi/a, \pi/b, 0)$ -  $M'(0, \pi/b, 0)$ -  $\Gamma$ . The band gap evolution with thickness we have analyzed in Table 7.1 can be seen, closing as the number of unit cells increases. The most noticeable feature arising in these band structure plots are the surface states appearing below the Fermi level. The surface Cr-d character of the bands is marked in Fig. 7.2. Due to the dangling bonds (lack of apical nitrogens) around the Cr atoms at the surface, the Cr d-levels split as sketched in Fig. 7.1(b): the  $t_{2g}$  triplet with the  $d_{xz,yz}$  doublet lying lower in energy completely occupied below

**Table 7.1:**

Band gap values (in meV) for CrN bulk and thin films of different thicknesses obtained within the LDA+ $U$  method ( $U=4$  eV) using an in-plane AFM order (both for the non-relaxed and the relaxed positions) using the cubic and orthorhombic bulk unit cells. In the insulating cases, the band gap is obtained as the difference between the eigenvalues at  $\Gamma$  (bottom of the conduction band) and  $M$  (top of the valence band). In the metallic cases, the degree of metallicity is measured as the same difference (in that case with negative value).

	NUMBER OF LAYERS				
	BULK	4	6	8	10
CUBIC					
<i>Non – relaxed</i>	200	119	128	122	113
<i>Relaxed</i>		206	195	19	-100
ORTHORHOMBIC					
<i>Non – relaxed</i>	170	4	18	16	10
<i>Relaxed</i>		34	-14	-170	-225

the Fermi level, the  $d_{xy}$  singlet also occupied but split with respect to the  $d_{xz,yz}$ ; the  $e_g$  bands present the  $d_{z^2}$  also split with respect to the  $d_{x^2-y^2}$ , with the latter lying higher in energy. Another feature is that the surface Cr energy bands lie higher in energy than those of the inner ones, well separated due to a surface effect (we will analyze this below in detail). Let us focus on the  $M$ -point and its evolution as the thickness is increased to the right of Fig. 7.2. The highest occupied valence band has always surface Cr  $d$  character but not so the lowest lying unoccupied conduction band. In addition there is a flattening of the dispersion of this conduction band from  $\Gamma$  to  $M$  and more so from  $M'$  to  $\Gamma$  (even crossing the Fermi level in the 10-layer case at the same time that it loses most of its surface Cr character). For the X-point, however, a large surface Cr  $d$  character is always retained. As the thickness increases, the difference in bandwidth between more inner layers and the surface one (smaller coordination) becomes more noticeable, eventually producing the band crossings at the Fermi level that we observe for the 8- and 10-layer cases.

Although the shape of the bands right below the Fermi level is

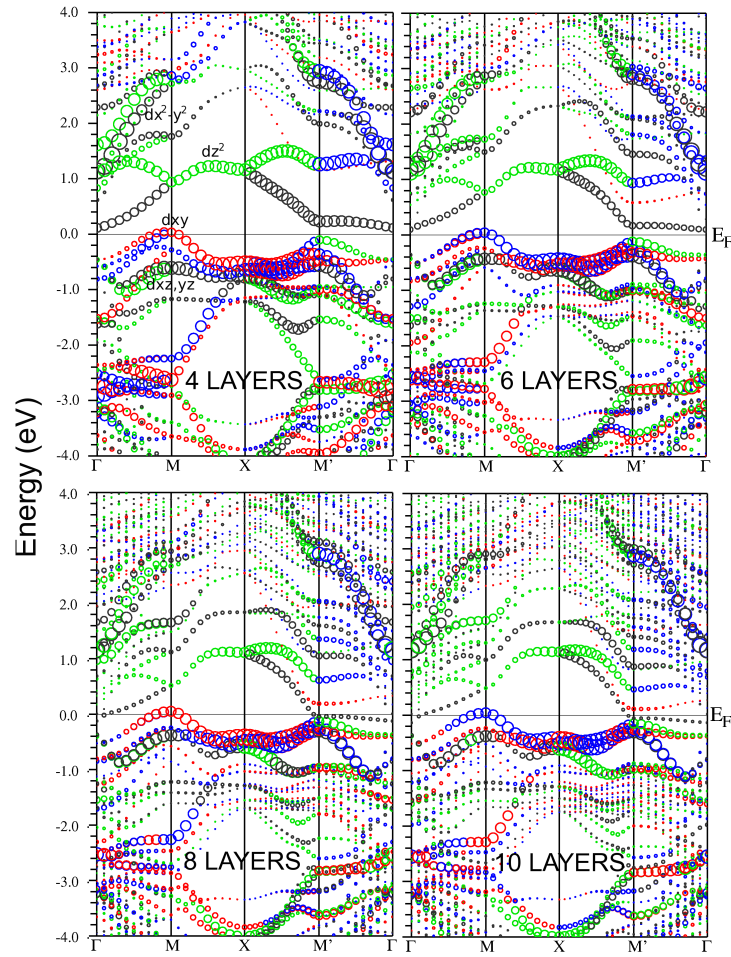


**Figure 7.2:**

Band structures with band character plot (surface Cr atom highlighted) for orthorhombic CrN films of 4, 6, 8 and 10 layers and relaxed positions. The size of the circles is proportional to the surface Cr character of the corresponding eigenstate. The colors indicate the irreducible representation of the eigenvalues. Whenever two bands cross, the connectivity of the band crossing can be seen just following the color of the band.

almost the same for all the thicknesses calculated, in the  $\Gamma$ - $M$  direction a different feature can be observed in the 4-layer (the thinner) case: the first two bands right below the Fermi level (of  $d_{xy}$  character and corresponding to the two surfaces) are split. The reason is that the distance between the two surfaces is not big enough and they actually interact through the CrN bulk (2-layer thick only) barrier leading to a bonding-antibonding splitting. Even for the 6-layer case a very small splitting along the same direction can be seen (particularly near the  $M$  point) but no splitting can be observed neither in the 8-layer nor in the 10-layer case indicating the thickness of the film in these cases is enough to guarantee the lack of interaction between the two surfaces across the CrN inner layers.

### 7.3.4 10-layer case in detail.

We will now focus on the 10-layer case to see the changes that happen when the atomic positions within the film are fixed at the bulk positions and also when relaxed. We have already mentioned that lattice relaxations lead to conducting states in these thin films. In order to check if these states right below the Fermi level with high surface Cr character are actually surface states, we have removed the vacuum (recovering the bulk solution but keeping the symmetries present in the films) and performed calculations in the same conditions (LDA+ $U$ ,  $U=4$  eV). The three band structure plots (non-relaxed, relaxed positions and vacuum suppressed) are shown in Fig. 7.3 with the surface Cr bands highlighted. For the non-relaxed case, the surface bands right below the Fermi level can be seen. These bands remain almost the same in the relaxed case (although with higher contribution from the surface Cr in the  $M$ '- $\Gamma$  direction). In both cases a very flat band appears in the  $M$ - $X$ - $M'$  direction at about -3.5 eV. The main contribution to this band comes from the surface N atom as a consequence of the hybridization of the N-p states with the Cr- $e_g$ -like ones. In both cases there is



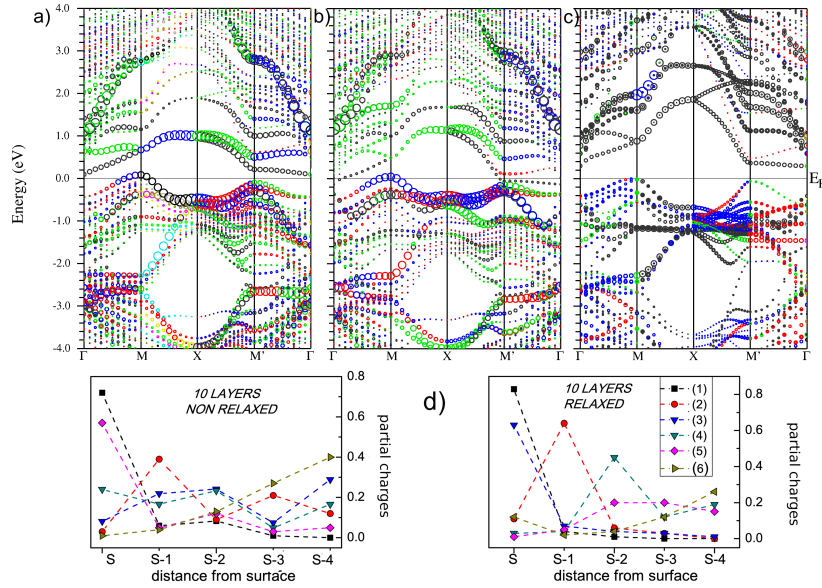


**Figure 7.3:**

Band structures with band character plot for the surface Cr atom in 10-layer thick CrN films within the orthorhombic structure (a) keeping the bulk positions fixed, (b) relaxing the atomic positions, and (c) without vacuum (in the (c) panel the character of the same atoms as in (a) and (b) is highlighted but of course there is no surface anymore since there is no vacuum). The (d) panel shows the sum of the partial charges of the atoms in each layer (from surface (S) to inner (S-n)) for the first six eigenvalues at  $M$  right below the Fermi level (being (1) the highest one) for both relaxed and non-relaxed structures.

a considerable contribution of the surface N atom to the surface bands particularly in the  $\Gamma$ - $M$  direction.

Let us see the main difference between the relaxed and the non-relaxed cases focusing on the bands around the Fermi level. In the non-relaxed case, the character of the band gap is clearly surface-like ( $d_{xy}$ - $d_{z^2}$ ) since most of the contribution to both the bands right above and below the Fermi level comes from the surface Cr atom. However, when the atomic positions are relaxed, the solution is metallic, and the character of the first band right above the Fermi level at  $M$  changes to

the more inner Cr atoms. The first band right below the Fermi level at  $M$  being of surface-Cr  $d_{xy}$  character and the first right above of innermost-Cr  $d_{z^2}$  character. Comparing with the case without vacuum, the curvature of the bands right below the Fermi level is different from the case with vacuum, indicating that the bands are different. As expected, the surface states shown in Fig. 7.3a and b no longer appear since there is no surface. In addition, the bands right below the Fermi level for the case without vacuum are not occupied by the interfacial Cr atom but by more inner ones.

Fig. 7.3d shows the sum of the partial charges of the atoms (Cr+N) in each layer (from surface (S) to inner (S-n) layers) for the first six (numbered 1 to 6, 1 being the highest one in energy) eigenvalues at  $M$  right below the Fermi level for the cases with a vacuum. This plot gives further confirmation of the surface character of the bands right below the Fermi level (shown in Fig. 7.3a and b). There are two eigenvalues whose highest partial charge comes from the surface. For those states, the value of the partial charges as a function of the layer decays rapidly as one moves away from the surface. These states should give rise to a non-negligible DOS at the Fermi level without contributing to the overall resistivity since they are states localized at the surface. Whether this is the observed effect in surface-sensitive photoemission experiments [113] or not, that is still an open question. Eigenvalue (2) is fairly delocalized in the non-relaxed case, but gets more localized in the S-1 layer (and a bit in S) after the relaxation. However, for the other eigenvalues the character of the partial charge is much more oscillating in the different layers suggesting that those states are more bulk-like states. Again, we see how the surface states are more localized than those in the more inner layers away from the surface.

Concerning the magnetic moments of Cr ions, the values are in between those reported experimentally (2.36 and 3.17  $\mu_B$ ) [104, 133]. Values of the magnetic moment inside the Cr muffin-tin spheres chosen change from 2.63  $\mu_B$  for the surface Cr to 2.57  $\mu_B$  for the inner ones in

the case of the non-relaxed structures. For the relaxed structures, the magnetic moment of the surface Cr is around  $2.53 \mu_B$  for the surface Cr and  $2.50 \mu_B$  for the other Cr atoms. Relaxations distribute moments more evenly, but still surface Cr atoms always have larger moments.

### 7.3.5 Influence of lattice relaxations: surface dipole formation.

We have seen that we have surface states crossing the Fermi level only in the relaxed cases. We will deepen into the details of structural relaxations in order to better understand their origin. The lattice relaxations were obtained within GGA allowing a displacement of the atoms along the  $z$ -direction. Looking at the average distances between planes shown in the inset of Fig. 7.4 at first we notice a Friedel-like surface relaxation where the surface atoms relax inwards (average distance to the S-1 plane only  $2.03 \text{ \AA}$ ) but the distance between the S-1 and S-2 layer increases to  $2.11 \text{ \AA}$  and the bulk distance ( $2.08 \text{ \AA}$ ) is reached in an oscillatory way. Atomic displacements from the ideal rocksalt structure that affect Cr cations and N anions in the same way will give no net lattice polarization. However, if the displacements are different for cations and anions, they have a polar character and will result in the appearance of a local electric field that should displace the bands to higher energies where the field is bigger. The difference in displacements experienced by Cr/N atoms for each layer is shown in Fig. 7.4. The largest displacements are always observed at the surface, where the differences in the electronic distribution are also larger due to the dangling bonds. The absence of an apical N forces the Cr atoms at the surface to relax inside the N-pyramid formed by its 5 anion neighbors. Thus, the surface CrN plane has higher N character, being the Cr atoms slightly lower in height, away from the surface. This type of surface relaxation pattern has been obtained in the past for the (001) surface of other TMN (VN and TiN). This will lead to a net polarization near

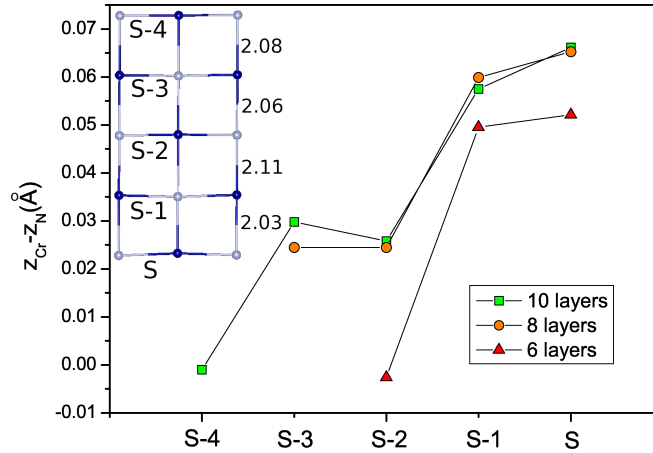


**Figure 7.4:**

Vertical displacements of N anions with respect to Cr cations ( $\Delta z = z_{Cr} - z_N$ ) in CrN films 6-, 8- and 10-layer thick obtained within GGA. The abscisse axis shows the distance from the surface in terms of number of layers (S-n). The inset shows half a unit cell of the relaxed 10-layer structure with the Cr atoms in blue (darker) and the N atoms in gray (lighter). The buckling of the octahedra/pyramids (particularly at the surface) can be observed. The average distances between layers along the z-axis (in Å) are also shown.

the surface and to some degree could lead to the appearance of a negatively charged plane caused by the higher density of  $N^{3-}$  anions at the surface. In any case, it can be seen that the difference in displacement of Cr and N atoms is reduced away from the surface towards the inner layers. For 10 and 6 layers, Fig. 7.4 shows the differences in the positions of Cr and N atoms for the central layers are almost negligible. The displacements are a clear indication of the potential being different for the surface atoms due to the dangling bonds.

Those ionic displacements and the redistribution of electrostatic potential near the surface will have consequences in the band structure. In order to analyze the distribution of electronic states around the Fermi level and their shift in energy with respect to the more inner layers we have plot in Fig. 7.5 the density of states (DOS) of Cr and N atoms in the 10-layer relaxed film. In Fig. 7.5a it can be seen that the  $t_{2g}$ -like,  $d_{xz,yz,xy}^\dagger$  orbitals (degenerate for the inner (S-4) Cr atom and with this

degeneracy lifted at the surface (S)) are filled (in the range between  $-2$  and  $0$  eV below the Fermi energy). A small amount of (bonding)  $e_g$  levels (in the range between  $-6$  and  $-3$  eV) are occupied for every Cr atom. Comparing the surface (S) and central (S-4) DOS of Cr atoms, an upward shift of the Cr- $t_{2g}$ -like bands of about  $1$  eV towards the Fermi level is observed (similar for the  $e_g$ 's but more difficult to observe due to their larger bandwidth). In Fig. 7.5b the features around the Fermi level can be distinguished: the metallic character (non-zero DOS at the Fermi level) and the larger contribution of the surface(S) Cr at  $E_F$ . It can also be seen that the upward shift is nearly rigid from layer to layer as the surface is approached: the inner the Cr atom is, the lower in energy the occupied  $t_{2g}^\uparrow$ -like and the unoccupied  $e_g$  manifolds are. This is consistent with the shift in potential as the surface is approached caused by the change in environment and the appearance of a surface dipole moment. We should clarify here that this situation is different to a potential build-up in polar interfaces, it is just a surface effect caused by dangling bonds at the surface. It will not be a cumulative effect as more layers are added up. In fact, the opposite is true, it should be more important for thinner layers, where the surface to volume ratio is higher and the surface states have a higher relative weight. Also, it becomes important in low-gap semiconductors like CrN, but (though still present) should be much less so for higher-gap ionic semiconductors like SrTiO<sub>3</sub>, TiO<sub>2</sub>, etc.

This can be analyzed more quantitatively using the shift in core-level energies (Cr-2s and N-1s) shown in Fig. 7.6. A shift of about  $1$  eV upwards as the surface is approached is observed here in Fig. 7.6 (core-level energies) as it was also in Fig. 7.5 (DOS). The electrons at the surface are less bound due to the absence of some ligands, which leads to a higher localization of their bands (smaller bandwidths), and also higher core-level energies caused by the local electric field produced by the atomic displacements we described above. Also, the broken symmetry reduces the crystal-field splittings and leads to a small increase in magnetic moment (that we quoted above). In metallic solutions, if

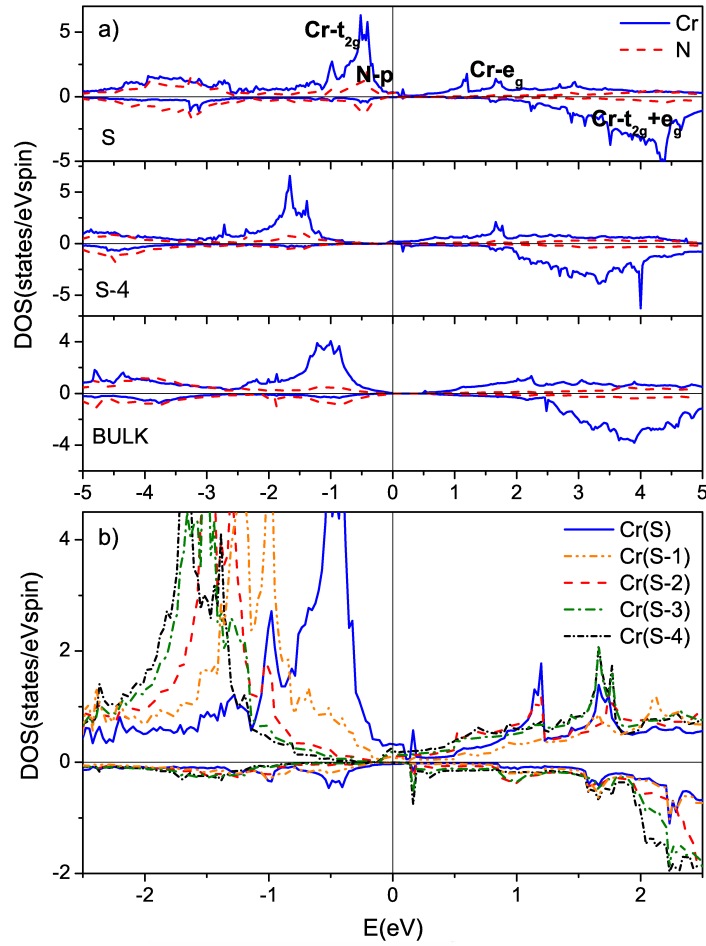


**Figure 7.5:** Density of states in the orthorhombic 10-layer CrN film with relaxed atomic positions of (a) the Cr and N atoms for the surface (S) and central (S-4) layers and, (b) the Cr atoms in each layer (from surface (S) to center (S-n)). The Fermi energy is set at zero. The positive and negative values are for spin-up and spin-down, respectively. The density of states of Cr and N atoms in bulk CrN is also shown in the (a) panel.

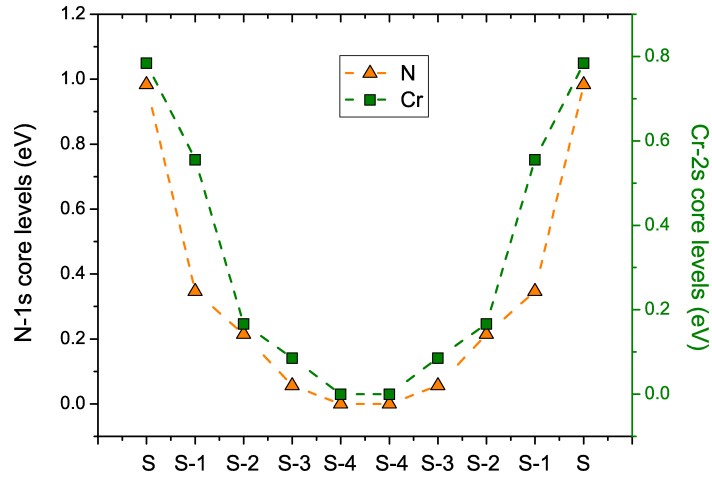


**Figure 7.6:** Energy difference of the N-1s and Cr-2s core level in the 10-layer case CrN film compared with the value of the central layer.

an ionic picture is still possible, one can argue that the lack of  $N^{3-}$  apical neighbors reduces the valence of the surface Cr atoms, leading to a larger magnetic moment. Being the system almost in the localized limit, with very small charge redistribution among bands, the effect is small but still noticeable in the calculations.

## 7.4 Summary

We have studied the appearance of surface states in thin CrN films due to the dangling bonds caused by the lack of apical N atoms at the surface. These states become further stabilized by structural relaxations, that tend to favor a gap closure and hence a metallic solution for the system. Partial charges analysis confirms these conducting states live very close to the surface. The band gap closure comes about due to the displacements of the ions at the surface, where an electric field is formed, with the corresponding band shifts, as high as 1 eV. The non-relaxed cases remain insulating because the atomic relaxations that lead to such a local electric polarization are suppressed. This suggests that

local strains and other defects can drastically modify the conduction properties of CrN as it is observed experimentally.





## Electronic structure of CrN/MgO multilayers

“

*Science is a way of thinking much more than it is a body of knowledge.*

*[Carl Sagan]*

”

### 8.1 Background

Based on the different features found experimentally in CrN films with respect to the material as a bulk, we studied in Chapter 7 free standing thin films of CrN. We saw that when CrN is nanostructured in free standing thin films, surface states appear due to the absence of an apical N atom at the surface [213]. These states come about due to a surface electric dipole produced by a surface reconstruction, driving CrN thin films metallic as the number of CrN layers is increased. Partial charges analysis confirms these conducting states live very close to the surface.

However, in the experiments, most of CrN films are grown on MgO substrates. To check what the effects of CrN grown on top of a MgO substrate are from first principles electronic structure calculations we will study in this Chapter the electronic, and transport properties of CrN/MgO multilayers. No experimental studies exist to the best of our knowledge on multilayers but from a theory standpoint it is the best scenario to analyze the effect of a drastic dimensionality reduction and also the evolution of the system with thickness without conducting surface states appearing, that complicate the picture and prevent the study of quantum confinement effects alone. Our goal is to analyze the changes in electronic structure with respect to the material as a bulk and in free-standing thin films, determine the relaxed equilibrium structures and the appearance of new interfacial electronic states and their origin as a consequence of quantum confinement.

## 8.2 Computational procedures

For the structural relaxations we have used the Wu-Cohen version of the generalized gradient approximation (GGA). Again, to deal with strong correlation effects, we apply the LDA+ $U$  scheme taking the optimal  $U$  value for bulk CrN ( $U = 4$  eV) as we discussed in Chapter 3. The on-site Hund's exchange parameter  $J_H$  was set to zero. All the calculations were fully converged with respect to all the parameters used. In particular, we used  $R_{mt}K_{max} = 7.0$ , and muffin-tin radii of 1.95 a.u. for Cr, 1.73 a.u. for N, 1.79 a.u. for Mg and 1.69 a.u. for O. For the transport properties calculations we used denser grids, with up to 40000 k-points ( $57 \times 57 \times 11$  for 5,  $61 \times 61 \times 10$  for 7 and  $64 \times 64 \times 9$  for 9 CrN layers) to obtain convergence.

## 8.3 Results

We investigate the changes in the electronic structure that occur when CrN is sandwiched between MgO. A barrier of 5 MgO layers (about 2

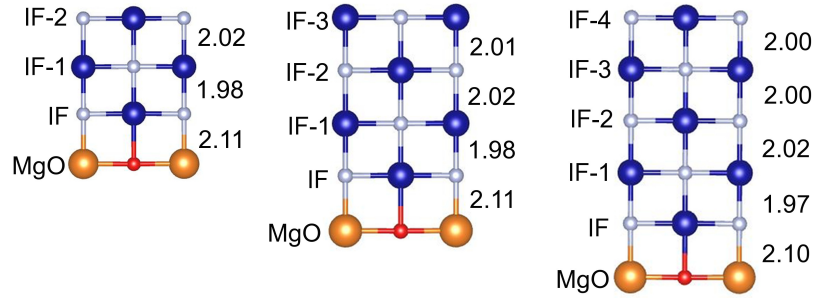
**Table 8.1:**

Out-of-plane optimized cell parameters for CrN/MgO multilayers 3-, 5-, 7- and 9- CrN layers thick (in Å) obtained using the Wu-Cohen version of the GGA.

	NUMBER OF LAYERS			
	3	5	7	9
<i>Relaxed</i>	31.7	39.2	46.5	53.7

nm thick) between CrN blocks has been used for all the calculations checking that it is enough to guarantee the lack of interaction between CrN blocks. We have modeled MgO/CrN multilayers 3-, 5-, 7- and 9- CrN layers thick grown along the (001) direction (approximately 1 to 4 nm thick). The in-plane lattice parameters are constrained to those of MgO. In-plane checkerboard AFM order (as the one used in Chapter 7 for free standing films) was imposed in the CrN blocks and again in order to allow for this type of ordering within one plane, an in-plane  $\sqrt{2} \times \sqrt{2}$  supercell was constructed. Let us recall that in multilayers grown along the (001) direction of the rocksalt structure, interfaces are non-polar in nature. A rather different and yet interesting situation happens when growing MgO(111) on top of a polar  $\text{Al}_2\text{O}_3(0001)$  substrate. Mg vacancies at the interface facilitate the lattice match with the hexagonal substrate and, after the structural relaxations, the distorted analog of the hexagonal (wurtzite-like) structure survives for a few nm until the interface effects are no longer felt inside the MgO block and the preferred bulk rocksalt structure is recovered [214].

For all the cases we have performed calculations with fully relaxed atomic positions also optimizing the value of the c-lattice parameter. We have used as starting point the optimized cell parameter for bulk MgO using the Wu-Cohen exchange-correlation potential of 4.23 Å. From this value, we have constructed the multilayers and optimized the out of plane c-lattice parameter for each number of CrN layers. The optimized values of the c-lattice parameter are shown in Table 8.1.

**Figure 8.1:**

Half a unit cell of CrN blocks of the relaxed 5-, 7- and 9- CrN layers with Cr atoms in blue (darker) and the N atoms in gray (lighter). The average distances between layers along the  $z$  axis (in Å) are shown.

The relaxed  $c$ -parameter is reduced with respect to the MgO bulk value (from a 1% to a 4% reduction for multilayers 3- to 9- CrN layers thick). The tendency is the expected one since the optimized cell parameter for MgO of 4.23 Å is slightly larger than that of CrN (4.13 Å for the cubic phase).

From an ionic model point of view, in this case we should distinguish two types of octahedral environments for the Cr cations: a N-only environment for the inner Cr atoms and with an O ion in one of the apical positions for the interfacial Cr atoms (see Fig. 8.1). The average valence for the Cr cations is again 3+ so we should expect for an octahedral Cr atom in a high-spin state ( $S = 3/2$ , magnetic moment of  $3 \mu_B$ ) the orbitals  $d_{xz,yz,xy}^\uparrow$  completely filled while the minority  $d_{xz,yz,xy}^\downarrow$  remain empty, with the  $d_{x^2-y^2,z^2}$  states for both spin channels also completely empty above the Fermi level. The type of environment at the IF will destabilize the  $d_{z^2}$  with respect to the  $d_{x^2-y^2}$  and stabilize the  $t_{2g}$ 's more with the concomitant increase of the magnetic moment due to the substitution of one apical N by an O.

When CrN is nanostructured in free-standing thin films as we saw in Chapter 7, surface states appear due to the absence of an apical N atom at the surface [213]. These states come about due to a surface

electronic dipole produced by a surface reconstruction, driving CrN thin films metallic as the number of CrN layers is increased. In the case of the CrN/MgO multilayers also the differences in electronic distribution are bigger at the interface. The environment there is still octahedral but instead of being formed by six N atoms, it has 5 N atoms and one O atom in an apical position. We can look at the results of the structural relaxations in order to understand what the consequences of the different electronic distribution at the interface can be. The atomic displacements of cations and anions in the multilayers are not significant (the biggest difference is around 0.01 Å) so no local electric fields appear at the interface. Hence, no metallic solutions should be expected for the atomic displacements at the IF as happened in free-standing films. Looking at the average distances between planes shown in Fig. 8.1 at first we notice a considerably larger distance between the interfacial MgO-CrN layers of around 2.11 Å (roughly the interface distance in bulk MgO) due to the different environment at the IF and the different charge of the O anion. The in-plane distance (fixed) is also 2.11 Å in all cases. The distance between the IF and IF-1 layers is always reduced to around 1.97 Å but the distance between the IF-1 and IF-2 CrN layers increases to 2.02 Å and is reduced and stabilized at around 2.00 Å for the inner layers. Consequently, the potential at the interface will change due to the different type of environment and significantly different distances from the Cr atom along the c-axis: one larger Cr-O distance of 2.11 Å and one shorter Cr-N distance of 1.97 Å giving rise to a largely distorted octahedron.

This local environment at the interface will have consequences in the electronic distribution. It is interesting to analyze the evolution of the band gap and the band structure in the various multilayers we have calculated. Looking at Table. 8.2 one can see that the band gap is widened as the number of CrN layers is reduced due to dimensionality reduction. In contrast with the case of free-standing films, for every thickness studied, all the solutions are insulating. However, the same effect observed in free-standing films of the closure of the band gap

**Table 8.2:**

Band gap values (in eV) for MgO/CrN multilayers of different thicknesses obtained within the LDA+ $U$  method ( $U=4$  eV) using an in-plane AFM order. The band gap is obtained as the difference between the eigenvalues at  $\Gamma$  (bottom of the conduction band) and  $M$  (top of the valence band).

	NUMBER OF LAYERS			
	3	5	7	9
<i>Relaxed</i>	0.69	0.42	0.25	0.14

as the number of CrN layers is increased can also be observed. As mentioned above, in the case of the CrN/MgO multilayers there is no lack of an apical N at the interface but a substitution of it by an O.

The evolution of the band structure within the LDA+ $U$  method ( $U=4$  eV) with the CrN block thickness using the fully relaxed positions is presented in Fig. 8.2, where the interfacial Cr-d character of the bands is marked. We have chosen a standard in-plane k-path  $\Gamma(0, 0, 0)$ -  $M(\pi/a, 0, 0)$ -  $X(\pi/a, \pi/b, 0)$ -  $M'(0, \pi/b, 0)$ -  $\Gamma$ . The band gap evolution with thickness we have analyzed in Table 8.2 can be seen, closing as the number of unit cells increases. The band gap increases as CrN is confined to the smallest thicknesses, as has been observed in other correlated 3d electron systems as we have seen in the Introduction for SrVO<sub>3</sub>/SrTiO<sub>3</sub>. The most noticeable feature arising in these band structure plots are the interface states appearing below the Fermi level. The basic electronic structure described above can be seen with the  $t_{2g}$  triplet ( $d_{xy, xz, yz}$ ) lying lower in energy completely occupied below the Fermi level; the  $e_g$  bands for the IF Cr atom present the  $d_{z^2}$  split with respect to the  $d_{x^2-y^2}$ , with the latter lying higher in energy. Due to the different environment of the interfacial Cr atoms with five N and one apical O, the interfacial Cr-d levels lie lower in energy with the bands right below the Fermi level not having interfacial Cr contribution but from the Cr atoms in the IF-1 layer. The fact that at the IF one of the apical N in the octahedral environment is substituted by an O lowers

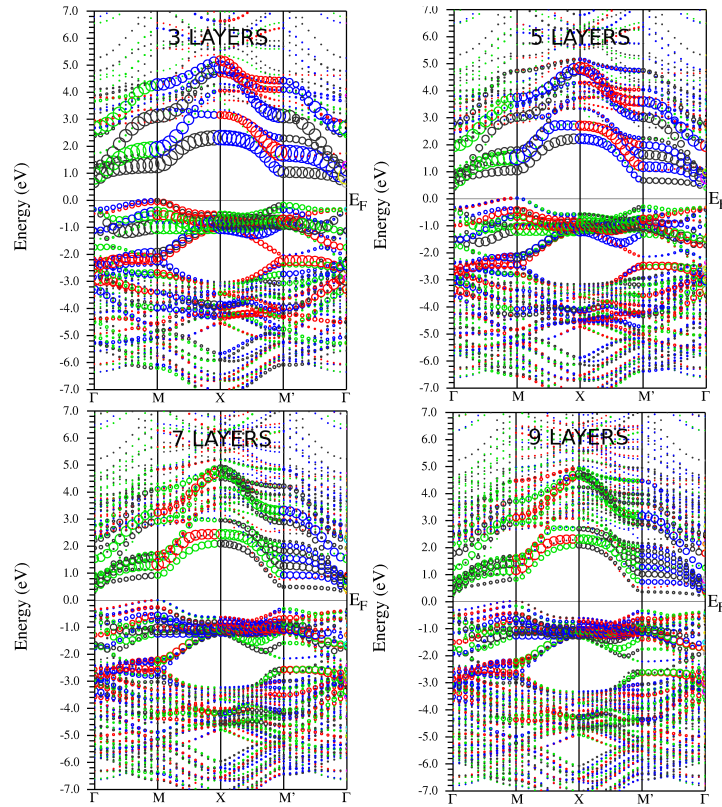


**Figure 8.2:**

Band structures with band character plot (interface Cr atom highlighted) for CrN/MgO multilayers 3-, 5-, 7- and 9- CrN layers thick and relaxed positions. The size of the circles is proportional to the interface Cr character of the corresponding eigenstate.

in energy the corresponding Cr-d levels, so they move away from the close vicinity of the Fermi energy, as explained above.

Let us focus on the  $M$ -point and its evolution as the thickness is increased to the right of Fig. 8.2 as we did with free-standing films. The highest occupied valence band has always IF-1 Cr-d character but not so the lowest-lying unoccupied conduction band whose biggest contribution comes from the IF Cr atom for thinner layers and from inner layers as the thickness is increased. Not only the occupied  $t_{2g}$  bands

coming from the IF Cr atom become lower, but also the unoccupied  $e_g$  ones (even though the splitting inside the  $e_g$  doublet is substantial). Thus, the character of the band gap is never interface-interface but IF-1 to IF ( $d_{xy}$ - $d_{z^2}$ ).

Concerning the magnetic moments of Cr ions, the values are in between those reported experimentally ( $2.36$  and  $3.17 \mu_B$ ) [104, 133]. Values of the magnetic moment inside the Cr muffin-tin spheres chosen change from  $2.51 \mu_B$  for the interfacial Cr to  $2.48 \mu_B$  for the inner ones in the case of the non-relaxed structures. The interfacial Cr atom always has a slightly higher value of the magnetic moment as a consequence of its different environment (lower lying  $d$ -levels imply a larger magnetic moment due to the larger  $d$  weight in the bonding states, in a molecular orbital picture). In a purely ionic picture one could reason that the interfacial Cr atoms have an effective lower valence and hence slightly larger moment (and  $d$  occupation).

Again, in order to study the distribution of electronic states around the Fermi level and the shift in energy at the interface with respect to the more inner layers the density of states can be analyzed. We have plot in Fig. 8.3 the density of states (DOS) of Cr atoms in multilayers with 5, 7 and 9 CrN layers. It can be seen that the  $t_{2g}$ -like orbitals are filled for all the Cr atoms. In the case of CrN films a nearly rigid upward shift of the Cr- $d$  levels of around 1 eV from the innermost one to the surface can be observed. This does not happen in the case of the multilayers. In the multilayers, the  $t_{2g}$  peak of the IF Cr atoms is always the lowest in energy (see arrow in Fig. 8.3) due to the different type of environment at the interface with an O atom and the larger Cr-O bond in comparison with the Cr-N ones that causes an opposite effect. This can be best noticed by the reduced DOS from the IF Cr atom in the energy window closer to the Fermi level. It is the IF-1 Cr the highest in energy for all the cases studied.

The effects happening at the interface can be analyzed more quantitatively using the shift in core-level energies (Cr-2s and N-1s). In the case of the free-standing films, as a consequence of the local electric



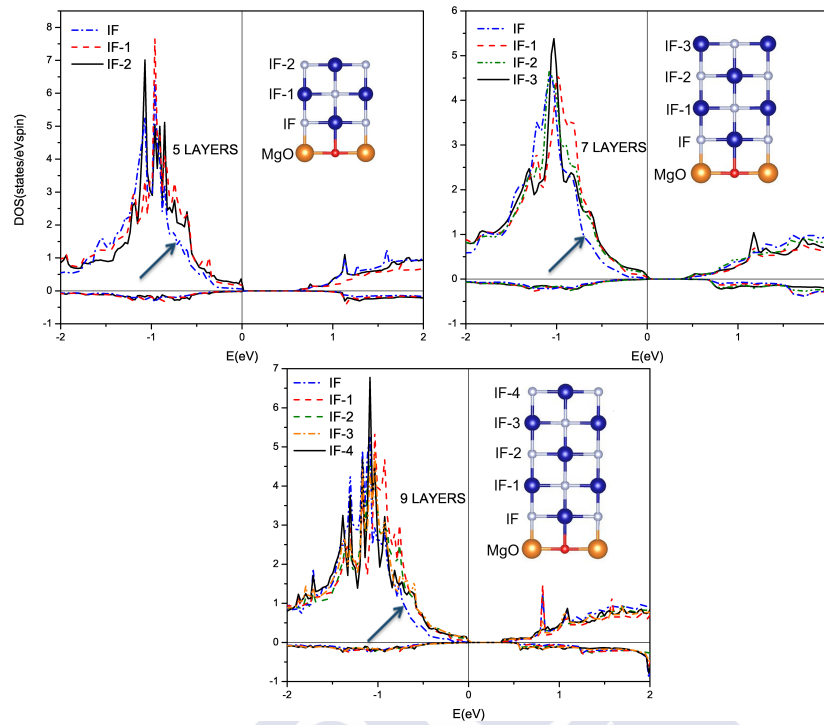


**Figure 8.3:**

Density of states of the Cr atoms in CrN/MgO multilayers 5-, 7- and 9- CrN layers thick (from left to right) from the innermost to the interfacial layer of the CrN block. The arrows mark the lower IF weight close to the Fermi level.

field formed at the surface, there is a shift of about 1 eV in the Cr-2s and N-1s upward as the surface is approached. The electrons at the surface are less bound due to the absence of some ligands, which leads to higher core-level energies caused by the local electric field produced by the atomic displacements. The shifts in the core levels from the interface to the central layers in CrN/MgO multilayers are shown in Fig. 8.4. Focusing on the Cr-2s core levels it can be seen how at the interface they are always around 0.2-0.3 eV lower than at the IF-1 layer. This is consistent with the picture of the DOS described above where the occupied  $t_{2g}$  peak for the interfacial Cr atom is always the lowest

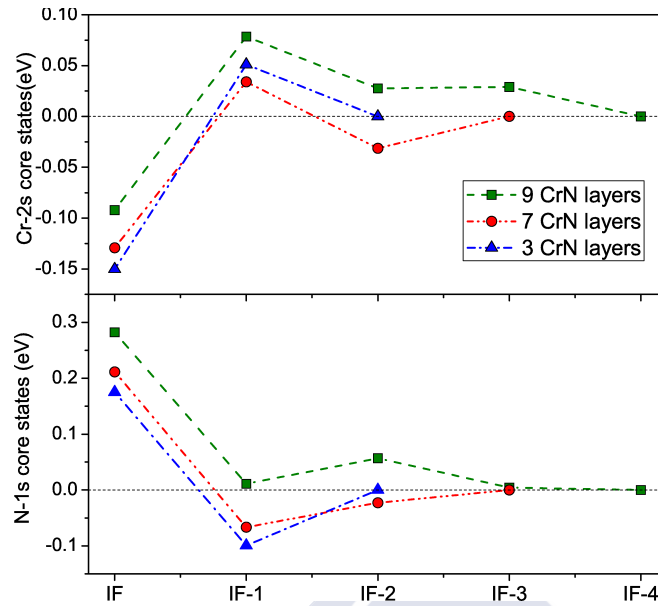


**Figure 8.4:**

Energy difference of the N 1s and Cr 2s core levels in CrN/MgO multilayers 5-, 7- and 9- CrN layers thick compared to the value of the central layer.

in energy. Again, this is a consequence of the different environment for Cr atoms at the interface and different to the situation in free-standing CrN films. For the N atoms, the behavior is the opposite with the core levels at the interface being higher in energy and decaying rapidly as one moves away from it.

CrN shows promising thermoelectric properties in its bulk shape [110, 111]. Potentially, thin films can be obtained that would increase the thermoelectric figure of merit via the mechanisms described in Chapter 1. This multilayered system provides a way to analyze the dependence of the thermoelectric properties (e.g. thermopower) as a function of the thickness without the additional ingredients of conducting surface states appearing, like it occurs in thin films. In order to check the quantum confinement effects in the thermoelectric properties of the material when sandwiched between MgO, we have calculated the

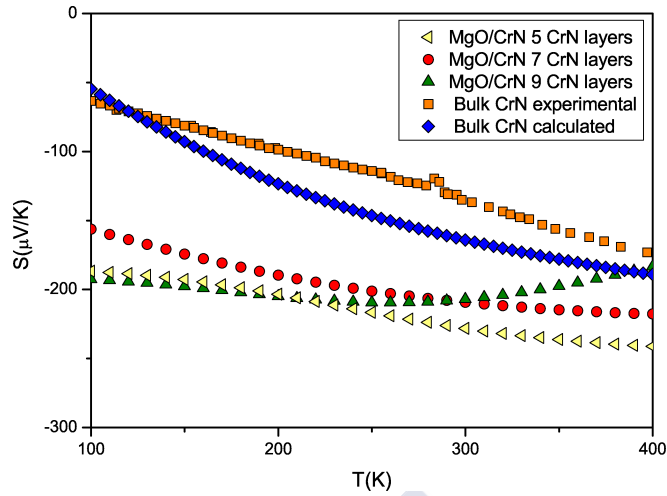


**Figure 8.5:**

Experimental and calculated temperature dependence of the thermopower for bulk and multilayers with different CrN thickness. Quantum confinement leads to an increase in the thermopower.

dependence of the thermoelectric power with temperature for different CrN thicknesses.

In Fig. 8.5, for the sake of comparison, we present the calculations together with the experimental values of the thermopower as well as the results for CrN bulk within LDA+ $U$  ( $U = 4$  eV). As we already saw in Chapter 3, the values of the thermopower obtained for the bulk fit the experimental results nicely. It can be seen how, overall, the growth of CrN films increases the values of the thermopower that can be obtained from the bulk, particularly at low temperature but also in the high temperature limit. No general tendency as the CrN thickness is increased can be obtained from the calculations. The curves for the different thicknesses studied are very similar, always larger than in the bulk. In calculations with much larger thicknesses it could be seen if any intermediate regime occurs before the bulk limit is reached. It is interesting to note that indeed the thermopower increases when films

sufficiently thin are grown and CrN remains stoichiometric, insulating and retains magnetic ordering similar to the one shown in bulk samples.

## 8.4 Summary

We have calculated the electronic structure of multilayers of CrN/MgO with varying CrN thickness. The band gap increases as CrN is confined to the smallest thicknesses, as has been observed in other correlated  $3d$  electron systems. This leads to an increase in the calculated thermopower. The interface between the nitride and the band insulating oxide leads to a small band shift that stabilizes the interfacial Cr- $d$  bands, as observed in the DOS and in the core-level energies. This would be the appropriate system to study the intrinsic non-metallic properties of CrN, that in the past has been observed to occur close to a metal-insulator transition: i) in the bulk non-stoichiometry always can distort the picture, allowing for a wide range of interpretations of its electronic structure to appear in the literature, ii) in the case of thin films, surface states due to the surface polarity complicate the understanding of its electronic properties. Those effects can be minimized in this multilayered system.



## List of Publications

- 1.-** A. Piñeiro, **A. S. Botana**, V. Pardo and D. Baldomir, “Fermiology and magnetism in weak itinerant ferromagnet  $\text{CoS}_2$ : an ab initio study”, *J. Phys.: Condens. Matter*, **22** (2010) 505602.
- 2.-** A. Piñeiro, **A. S. Botana**, V. Pardo, J. Botana, M. Pereiro and D. Baldomir, “Electronic structure and transport properties at high pressure in  $\text{ZnV}_2\text{O}_4$ ”, *J. Appl. Phys.* **109** (2011) 07E158.
- 3.-** **A. S. Botana**, P. M. Botta, C. de la Calle, A. Piñeiro, V. Pardo, D. Baldomir, J. A. Alonso and J. Rivas, “Electronic structure analysis of the quasi-one-dimensional oxide  $\text{Sr}_6\text{Co}_5\text{O}_{15}$  within the LDA+U method”, *J. Appl. Phys.* **109** (2011) 07E114.
- 4.-** **A. S. Botana**, P. M. Botta, C. de la Calle, A. Piñeiro, V. Pardo, D. Baldomir and J. A. Alonso, “Non-one-dimensional behavior in charge-ordered structurally quasi-one-dimensional  $\text{Sr}_6\text{Co}_5\text{O}_{15}$ ”, *Phys. Rev. B*, **83** (2011) 184420.
- 5.-** **Antia S. Botana**, V. Pardo, D. Baldomir, A. V. Ushakov, and D. I. Khomskii “Electronic structure of  $\text{V}_4\text{O}_7$ : Charge ordering, metal-insulator transition, and magnetism”, *Phys. Rev. B*, **84** (2011) 115138.

- 6.- A. S. Botana**, F. Tran, V. Pardo, D. Baldomir, and P. Blaha “Electronic structure of CrN: A comparison between different exchange correlation potentials”, *Phys. Rev. B*, **85** (2012) 235118 .
- 7.-** Carlos Martínez-Boubeta, **Antia S. Botana**, Víctor Pardo, Daniel Baldomir, Aldrin Antony, Joan Bertomeu, Josep M. Rebled, Lluís López-Conesa, Sonia Estradé, and Francesca Peiró “Heteroepitaxial growth of MgO(111) thin films on Al<sub>2</sub>O<sub>3</sub>(0001): Evidence of a wurtzite to rocksalt transformation”, *Phys. Rev. B*, **86** (2012) 041407.
- 8.-** Victor Pardo, **Antia S. Botana**, and Daniel Baldomir “Enhanced thermoelectric response of hole-doped  $La_2NiO_{4+\delta}$  from ab initio calculations”, *Phys. Rev. B*, **86** (2012) 165114.
- 9.- Antia S. Botana** Víctor Pardo, Daniel Baldomir and Peter Blaha “Conducting states caused by a surface electric dipole in CrN(001) very thin films”, *Phys. Rev. B*, **87** (2013) 075114.
- 10.-** Victor Pardo, **Antia S. Botana**, and D. Baldomir “Strain effects to optimize the thermoelectric properties of hole doped  $La_2NiO_{4+\delta}$ ”, *Phys. Rev. B*, **87** (2013) 125148.



## Resumo da presente Tese Doutoral

Na presente tese doutoral recóllese o traballo de investigación realizado por Antía Sánchez Botana durante a súa etapa de posgrao. En liñas xerais o traballo consistiu no estudo das propiedades estruturais, electrónicas, magnéticas e termoeléctricas de diferentes sistemas compostos por metais de transición, próximos a unha transición metal-illante.

Unha gran parte do desenvolvemento tecnolóxico nas últimas décadas está vencellado á ciencia de materiais e á física da materia condensada. Particularmente, durante a segunda metade do século XX, fomos testemuñas dunha explosión de novos materiais así como de xeitos de optimizar as súas propiedades. Un dos motores desta revolución tecnolóxica é a capacidade de controlar as propiedades electrónicas dun material a conveniencia. Unha importante clase de materiais noveles son os compostos de metais de transición onde aparecen propiedades destacadas como ferroelectricidade, magnetorresistencia colosal, superconductividade de alta temperatura, transicións metal-illante, etc. A maiores desta heteroxeneidade de fenómenos físicos, este tipo de compostos amosan potencial para exhibir novas propiedades: a mellora das propiedades termoeléctricas mediante nanoestruturación ou toda a serie de novos fenómenos en superficies e interfaces entre óxidos de

metais de transición e a súa posible aplicación na chamada electrónica de óxidos son claros exemplos.

Os compostos de metais de transición son sistemas que presentan fortes correlacións electrónicas e teñen en común a presenza de electróns  $d$ . Posto que os orbitais  $d$  (ao igual que os  $f$ ) son moi localizados, neles cobra importancia a repulsión coulombiana entre electróns. Cando a repulsión coulombiana é grande, un modelo de electróns independentes deixa de ter sentido. Deste xeito, o movemento dun electrón depende da posición do resto nun intento de reducir a repulsión coulombiana que experimenta. Por iso se fala de electróns fortemente correlacionados. O magnetismo en sólidos é, na súa maior medida, a manifestación destas fortes interaccións electrón-electrón.

Deste xeito, en sistemas reais non poden pois ignorarse as interaccións coulombianas entre electróns e o efecto das interaccións de intercambio no seu movemento. As posicións e o movemento dos electróns está correlacionado debido precisamente ás interaccións coulombianas entre eles. Estas correlacións son difíciles de tratar teóricamente pero un método moi útil e que deu ata agora bos resultados é a teoría do funcional da densidade (DFT).

Nesta teoría, a enerxía do estado fundamental dun sistema multielectrónico pode escribirse como un funcional da densidade electrónica  $\rho(\vec{r})$ . A idea básica consiste en pasar dun sistema multielectrónico de electróns interaccionantes a un sistema monolectrónico non interaccionante sometido a un potencial externo efectivo, tendo ámbolos dous a mesma densidade electrónica. Nesta nova formulación, o hamiltoniano contén os seguintes termos: enerxía cinética dos electróns (os núcleos considéranse fixos, na aproximación de Born-Oppenheimer), potencial coulombiano debido ás interaccións electrostáticas electrón-electrón, electrón-núcleo e núcleo-núcleo e un termo chamado potencial de intercambio-correlación ( $V_{xc}$ ) que cuantifica as interaccións e que representa esa parte efectiva ou aproximada do potencial. Deste xeito, en lugar de ter que buscar a complicada función de ondas do sistema (vector dun espazo de Hilbert que depende de  $3N$  variables),



só consideramos a densidade electrónica  $\rho(\vec{r})$  (escalar que só depende da posición) que se convirte na variable fundamental, o que supón unha enorme simplificación. A busca da densidade electrónica que minimize o funcional (principio variacional) condúcenos á ecuación que permite obter a enerxía exacta do estado fundamental do sistema. A implementación desta aproximación realizouse na presente tese mediante o código WIEN2K. As propiedades de transporte calculáronse empregando o código BoltztraP que usa unha aproximación semiclásica baseada na teoría de transporte de Boltzmann empregando a aproximación de tempo de relaxación constante.

A continuación destacaremos os aspectos máis importantes dos materiais estudados.

## B.1 Estrutura electrónica do $V_4O_7$ : orde de carga, transición metal-illante e magnetismo

$V_4O_7$  é un membro da serie homóloga  $V_nO_{2n-1} = V_2O_3 + (n-2)VO_2$ . A súa estrutura consiste en bloques de tipo rutilo ( $VO_2$ ) infinitos en dúas dimensións e con catro octaedros de lonxitude na terceira. Os planos entre bloques teñen a típica estrutura do  $V_2O_3$ . Catro son os V inequivalentes que forman dúas cadeas independentes: V3-V1-V1-V3 e V4-V2-V2-V4. O material amosa unha transición metal-illante a 250 K e tamén unha transición dun estado paramagnético a un estado antiferromagnético a uns 40 K. A contaxe electrónica lévanos a obter unha valencia promedio para os V de 3.5+. Deste xeito, de existir orde de carga, teríamos  $2V^{3+}$  e  $2V^{4+}$  por fórmula unidade. Estudos previos apuntaban a que a fase metálica (alta T) amosaba completa desorde de  $V^{3+}$ ,  $V^{4+}$  mentres que a fase illante amosaba orde de carga estando formada a cadea V3-V1-V1-V3 por  $V^{4+}$  e a cadea V4-V2-V2-V4 por  $V^{3+}$ . A maiores da cuestión da localización electrónica, moitos estudos

amosan que a metade dos  $V^{4+}$  (V1) e todos os  $V^{3+}$  (V2, V4) están apareados formando singletes de espín no estado illante.

De ser así, pódense plantexar certas cuestións. i) Cal é a natureza do apareamento no estado illante? A formación de singletes entre  $V^{4+}$  (catiões  $d^1$ ) é habitual pero non entre  $V^{3+}$  co que a razón da formación destes dímeros é unha pregunta aberta. ii) Cal é o mecanismo de orde magnética por debaixo de 40 K? Se aceptamos as hipóteses previas, todos os  $V^{3+}$  e a metade dos  $V^{4+}$  forman singletes, estando pois fóra do xogo. Só quedan dous V (lonxe ademais un do outro) e con espín 1/2 para dar lugar á resposta magnética do sistema o que en principio resulta difícil de entender.

Para tentar dar resposta a estas e outras cuestións, estudiamos a estrutura electrónica do material  $V_4O_7$ , analizando as diferencias entre a fase de baixa temperatura (con orde de carga, antiferromagnética e illante) e a de alta temperatura (sen orde de carga, paramagnética e metálica).

Os cálculos amosan a existencia de orde de carga na fase de baixa temperatura que, xunto coas distorsións estruturais, abren o gap. A fase de alta temperatura non amosa orde de carga, con todos os V nunha configuración electrónica similar ( $\sim d^{1.5}$ ). Todos os acoplamentos nas cadeas de V na fase de baixa temperatura son antiferromagnéticos, e os acoplamentos entre cadeas son moi débiles (e de distinto signo dependendo do valor empregado para  $U$ ). Os acoplamentos dentro das cadeas na fase de alta temperatura pasan a ser ferromagnéticos como resultado do cambio na distribución electrónica motivado pola falta de orde de carga. Obtivemos os acoplamentos antiferromagnéticos na fase de baixa temperatura que resultan ser fortes nos enlaces curtos  $V^{4+}-V^{4+}$ , unha orde de magnitude maiores que nos  $V^{3+}-V^{3+}$  (e dúas ordes de magnitude maiores que nos enlaces longos  $V^{4+}-V^{4+}$ ). Isto suxire a formación dun singlete entre os vanadios que forman enlace curto nas cadeas  $V^{4+}$ , deixando os dos extremos das cadeas con espíns desapareados. O acoplo nas cadeas  $V^{3+}$  é máis complicado, amosando signos de redución dos momentos magnéticos debido a hibridacións.

A orde orbital obtida dos cálculos de estrutura electrónica ( $V^{4+}$ :  $d_{xy}$  vs.  $V^{3+}$ :  $d_{xz}, d_{yz}$ ) tamén axuda a entender as diferentes distancias de enlace nas dúas cadeas. Na cadea de  $V^{4+}$ , hai un enlace forte entre os dous vanadios do centro da cadea (V1-V1) formando un singlete de espín e un desprazamento de tipo antiferroeléctrico dos  $V^{4+}$  dos extremos (V3). Nas cadeas de  $V^{3+}$ , debido á distinta ocupación orbital, hai unha dimerización pero non o suficientemente forte como para facer dos dímeros  $V^{3+}$ - $V^{3+}$  singletes de espín.

Como resultado, probablemente os  $V^{4+}$  desapareados e todos os  $V^{3+}$  contribúen á orde magnética por debaixo da temperatura de transición o que fai moito máis comprensible a existencia de orde magnética por debaixo de 40 K.

## **B.2 Estrutura electrónica de CrN masivo: unha comparación entre distintos po- tenciais de intercambio correlación**

CrN é un nitruro de metal de transición que amosa unha transición magnetoestrutural arredor dos 280 K dende unha fase paramagnética con estrutura cúbica (alta temperatura) a unha fase antiferromagnética con estrutura ortorrómbica (a baixa temperatura). As súas propiedades electrónicas son motivo de controversia. Experimentalmente, atopáronse todo tipo de comportamentos a través da transición: metal-metal, metal-semiconductor, semiconductor-semiconductor. É particularmente destacable o feito de que a maioría de experimentos que atopan un comportamento metálico na fase de baixa temperatura son desenvolvidos en películas (moitos á súa vez medrados sobre MgO).

Para intentar aclarar algunhas destas controversias, desenvolvemos cálculos de estrutura electrónica en CrN usando diversos potenciais de intercambio-correlación: PBE, LDA+ $U$ , o funcional semilocal desenvolvido por Tran e Blaha baseado nunha modificación do de Becke-Johnson (TB-mBJLDA) e funcionais híbridos.

Para todos eles, os nosos cálculos amosan que ao establecer unha orde magnética en CrN se abre un gap. Podemos concluir que a fase antiferromagnética é sempre illante de acordo cos experimentos en mostras masivas estequiométricas. O comportamento metálico que se atopa en experimentos en películas delgadas ten que ver con efectos causados pola nanoestruturación como poden ser as vacantes, a tensión, efectos de superficie, etc. Nun sistema situado tan preto do límite itinerante, pequenos cambios poden dar lugar a metalicidade e incluso á supresión da transición magnética (que dos resultados dos cálculos parece ser altamente dependente dos detalles estruturais). O comportamento obtido para o poder termoeléctrico confirma que CrN na fase magnética é semiconductor, pero atopándose preto da transición dun comportamento localizado a un comportamento itinerante. A solución que atopamos como estado fundamental, describe con precisión as propiedades de transporte do sistema.

Ademais, os nosos resultados evidencian que o funcional TB-mBJLDA é extremadamente útil para tratar a estrutura electrónica de semicondutores correlacionados dando como resultado os mesmos valores de gap obtidos empregando LDA+ $U$  con  $U = 4$  eV (e próximo ao obtido experimentalmente) para distintas configuracións magnéticas e permitindo unha descripción do sistema libre de parámetros externos. Os funcionais híbridos tamén son quen de describir a estrutura electrónica de CrN, modificando a cantidade de intercambio exacto utilizada nos cálculos. Sen embargo, os resultados son comparables aos obtidos con LDA+ $U$  que permite unha descripción máis intuitiva dende o punto de vista físico e un menor esforzo computacional.

### B.3 Formación dun dipolo eléctrico na superficie de películas delgadas de CrN (001)

Empregando o método LDA+ $U$  co valor óptimo de  $U$  obtido para o material masivo, estudamos películas delgadas de CrN de distintos grosores para ver se era posible establecer a orixe do comportamento metálico atopado en experimentos en películas na fase de baixa temperatura. Deste xeito, aínda que vimos como no material masivo, o establecemento dunha orde antiferromagnética sempre abría un gap, comprobamos que en películas, o gap se pecha e aparecen estados de superficie conductores conforme o grosor do película aumenta. Deste xeito en películas con estrutura cúbica obtemos solucións metálicas para un grosor de 10 capas mentres que na simetría ortorrómbica xa con 6 se cerra o gap e aparecen estados conductores. A aparición de estados metálicos está conectada coas relaxacións estruturais na superficie, estando motivada polos distintos desprazamentos de Cr/N, coa consecuente formación dun campo eléctrico local que provoca un corrento nas bandas de entorno a 1 eV (tamén visible nos estados de core). Precisamente por ter o material masivo un gap moi pequeno, os dipolos eléctricos formados na superficie son quen de mover as bandas o suficiente como para dar lugar á metalicidade. As estruturas non relaxadas siguen sendo illantes dado que nese caso non hai polarización eléctrica ao non haber desprazamentos dos ións. Isto suxire que as tensións provocadas polo crecemento en películas así como outros defectos poden modificar drásticamente as propiedades de conducción do CrN, confirmando a nosa hipótese inicial.

## B.4 Estrutura electrónica de multicapas de CrN/MgO

Para analizar cales son os efectos de medrar CrN enriba dun substrato de MgO dende o punto de vista dos cálculos de primeiros principios, decidimos estudar multicapas de CrN/MgO. Dende o punto de vista teórico é o mellor escenario para analizar os efectos dunha drástica redución da dimensionalidade así como a evolución co grosor sen que aparezan estados de superficie conductores que complican o escenario. Deste xeito, desenvolvemos cálculos empregando de novo o método LDA+ $U$  co valor óptimo de  $U$  obtido para o material masivo para multicapas na que o grosor da barreira de MgO se mantivo constante a 5 capas mentres que o grosor dos bloques de CrN se variou dende 3 ata 9 capas. O gap neste caso aumenta conforme CrN está confinado aos grosos máis baixos e como se observou tamén noutros compostos correlacionados con electróns  $3d$ . Isto leva a un aumento do poder termoeléctrico en multilayers respecto do material masivo. Os fenómenos na interfaz entre CrN e MgO leva a un desprazamento das bandas que estabiliza os estados  $d$  do Cr interfacial, do mesmo xeito que se observa tamén nos estados de core. Podemos concluír que este sería pois o sistema apropiado para estudar as propiedades non-metálicas intrínsecas do CrN, que como dixemos anteriormente, se atopa preto dunha transición metal-illante: i) no caso do material masivo as inestequiometrías afectan, dando lugar a todo tipo de interpretacións da estrutura electrónica na literatura; ii) no caso das películas delgadas, os estados de superficie que aparecen debido a que esta superficie é polar complican a situación engadindo ingredientes extra.

## B.5 $\text{Sr}_6\text{Co}_5\text{O}_{15}$ : comportamento nonunidimensional nun óxido cuasiunidimensional con orde de carga

Este material pertence á familia de óxidos cuasiunidimensionais  $A_{n+2}B'B_n\text{O}_{3n+3}$  onde  $A$  é un catión alcalino ou alcalino térreo e  $B$  e  $B'$  corresponden a  $\text{Co}$  en entornos de prisma trigonal ou octaédrico e a cadea unidimensional está representada por  $B'B_n\text{O}_{3n+3}$ . Os membros dos extremos da serie  $\text{BaCoO}_3$  e  $\text{Ca}_3\text{Co}_2\text{O}_6$  foron os máis estudados polas fortes interaccións ferromagnéticas que amosan dentro das cadeas que obedecen a un modelo de tipo Ising e polas mesetas de magnetización observadas nas curvas de magnetización fronte a campo do segundo. Sen embargo, non se ten prestado moita atención aos membros intermedios da serie.

Por iso decidimos facer cálculos *ab initio* no óxido  $\text{Sr}_6\text{Co}_5\text{O}_{15}$ , membro con  $n=4$ . É un semiconductor con estrutura antiferromagnética que amosa algunhas peculiaridades na súa estrutura electrónica que o fan distinto do resto de membros da serie: i) os  $\text{Co}^{3+}$  son non magnéticos e cun entorno octaédrico; ii) os acoplamentos dentro das cadeas non son puramente ferromagnéticos, nas cadeas os acoplamentos son antiferromagnéticos (aínda que débiles); iii) isto, xunto coa existencia de dous  $\text{Co}$  non magnéticos na celda unidade, reducen non só os acoplamentos dentro das cadeas senón tamén entre cadeas; iv) debido a ii) e iii) as propiedades magnéticas do material non poden ser entendidas como cadeas de espíns con orde ferromagnética acopladas antiferromagnéticamente no plano como acontece co resto de membros da serie; v) a orientación preferida dos momentos angulares dos  $\text{Co}$  é non colineal, en contraste co comportamento de tipo Ising atopado nos membros extremos da serie. Ademais, os resultados dos cálculos de propiedades de transporte apoian as conclusións respecto da estrutura electrónica e magnética do material.

Este comportamento anómalo fai que  $\text{Sr}_6\text{Co}_5\text{O}_{15}$  sexa menos cuasiunidimensional do esperado dada a súa estrutura e axuda a entender as intrincadas relacións entre estrutura e propiedades eléctricas e magnéticas en sistemas con electróns fortemente correlacionados.

## B.6 Mellora na resposta termoeléctrica de $\text{La}_2\text{NiO}_{4+\delta}$ mediante dopado con ocos e tensión empregando métodos *ab initio*

Os óxidos de metais de transición, e particularmente as cobaltitas laminares, amosan propiedades prometedoras como materiais termoeléctricos. Dado que que o  $\text{La}_2\text{NiO}_4$  ten importantes similitudes tanto estruturais como de estrutura electrónica con ditas cobaltitas, o noso traballo plantexa a hipótese de que dito niquelato amose unha resposta análoga e por este motivo decidimos estudar a optimización das súas propiedades termoeléctricas, por unha banda mediante dopado con ocos, empregando distintos potenciais de intercambio correlación e engadindo despois tensión usando o potencial TB-mBJLDA do que xa comprobamos a súa eficiencia no estudo do CrN.

Os nosos cálculos *ab initio* neste composto amosan características prometedoras no niquelato  $\text{La}_2\text{NiO}_4$  dopado con ocos como material termoeléctrico. Se a conductividade térmica do material pode ser reducida mediante nanoestruturación (por exemplo, medrándoo en forma de películas delgadas) o sistema podería ter unha resposta termoeléctrica mellorada mediante o apropiado control do contido en osíxeno (parametrizado polo exceso  $\delta$ ). Os nosos cálculos amosan que para baixos niveis de dopaxe se obtén unha rexión cun poder termoeléctrico relativamente elevado empregando unha orde magnética de tipo antiferromagnético. A partir dos nosos resultados, suxerimos a realización dun estudo experimental neste material controlando o contido en osíxeno e facendo



películas delgadas coa apropiada composición de osíxeno. O dopado con ocós aumentará a conductividade, e isto, xunto coa redución da conductividade térmica polo crecemento en películas, farán que mellore a figura de mérito deste niquelato laminar. Unha mellora substancial da resposta termoeléctrica pode obterse medrando  $\text{La}_2\text{NiO}_4$  dopado con ocós baixo tensión. A idea é explorar a rexión cun parámetro de rede máis grande, no entorno do do  $\text{SrTiO}_3$  (3.95–4.05 Å). Os cálculos predín unha boa resposta termoeléctrica (cunha figura de mérito próxima á unidade) nesas condicións de dopaxe e tensión a altas temperaturas. Tralo noso estudo, recentes traballos experimentais veñen de verificar a nosa hipótese.

## B.7 Resumo xeral

Como resumo xeral, observamos que as técnicas *ab initio* permiten describir a física de compostos de metais de transición. Do mesmo xeito, as propiedades electrónicas, magnéticas e termoeléctricas poden ser controladas e optimizadas na busca de novos fenómenos e funcionalidades. Para iso, os experimentos computacionais que se presentan neste traballo de tese supoñen un paso adiante no obxectivo de levar a cabo o deseño computacional de novos materiais adaptados a unha funcionalidade concreta.





## Summary and conclusions

This PhD Thesis work deals with the analysis using first principles calculations of transition metal compounds whose electronic properties reside in the vicinity of a metal-to-insulator transition, the ultimate goal being the computational design of materials with new functionalities based on our calculations and the full understanding of these systems in order to make new predictions.

A large portion of the technological progress over the past decades has been related to Materials Science and Condensed Matter Physics. Particularly, the second half of the 20th century witnessed an explosion of new materials and new ways to tune their properties. A powerful driving force behind the technology revolution we have witnessed in the last decades is the ability to control on demand the electronic properties of a material. The best example are semiconducting field-effect transistors (several hundred million of these devices operate, for instance, in a smartphone). An important class of these novel materials is represented by transition metal compounds where outstanding electronic properties such as ferroelectricity, superconductivity, and colossal magnetoresistance are observed. In addition to this huge heterogeneity of physical phenomena, there is potential for exciting new discoveries in these materials: the enhancement of thermoelectric properties through

nanostructuring or the new phenomena on surfaces and interfaces between complex oxides are clear examples of that and have been explored by a lively scientific community in the last years.

Transition metal compounds show strong electronic correlations, having in common the presence of  $d$  electrons. Due to the fact that  $d$  orbitals (as well as  $f$  orbitals) are very localized, the Coulomb repulsion between electrons becomes important in these systems. When this happens, the behavior of their electrons can no longer be described effectively in terms of non-interacting particles. Like that, the movement of one electron depends on the position of the others, trying to reduce the Coulomb repulsion it experiences. This is the reason why we talk about strongly correlated electrons. Magnetism in solids is mainly due to these strong electron-electron interactions. Hence, in real systems, interactions between electrons cannot be ignored: the position and movement of the electrons are correlated. The treatment of these correlations is difficult from a theoretical point of view, but a method that has been shown to give good results is the so-called Density Functional Theory (DFT).

Within DFT, the ground state energy of a multielectronic system can be written as a functional of the electron density  $\rho(\vec{r})$ . DFT addresses the many-electron problem using the electron density (a scalar quantity in the real, 3-dimensional coordinate space) instead of the wave function (a vector of an  $N$ -dimensional Hilbert space) as central quantity, the basic idea consisting on moving from an interacting multielectronic system to a non-interacting monoelectronic one where the electrons are moving in an external potential, with both systems having the same electron density, the basic variable in DFT. All the DFT-based calculations in this Thesis have been performed using the WIEN2k code.

We will summarize below the most important results in the materials studied throughout this Thesis obtained using DFT-based calculations.

## C.1 Electronic structure of $V_4O_7$ : Charge ordering, metal-insulator transition, - and magnetism

$V_4O_7$  is a member of the homologous series  $V_nO_{2n-1} = V_2O_3 + (n-2)VO_2$  ( $3 \leq n \leq 9$ ), known as Magnéli phase compounds. Its crystal structure consists of rutile-like blocks that are infinite in two-dimensions and four  $VO_6$  octahedra wide in the third. The shear planes between the rutile blocks have the typical local structure for  $V_2O_3$ . The V sites are split into two groups: V3 and V4, which are at the shear plane ( $V_2O_3$ -like), and V1 and V2, at the center of the rutile blocks ( $VO_2$ -like). The cations form two independent chains V3-V1-V1-V3 and V4-V2-V2-V4 running parallel to the pseudorutile  $c$ -axis.  $V_4O_7$  shows a MIT at 250 K ( $T_c$ ) and it also exhibits a paramagnetic to antiferromagnetic (AFM) transition at  $T_N \sim 40$  K. A simple electron count in  $V_4O_7$  gives an average valence  $V^{3.5+}$  for the metal cations. Hence,  $2V^{3+}(d^2)$  and  $2V^{4+}(d^1)$  per formula unit could be expected if charge order would occur. Different previous works showed that the metallic state was characterized by an almost complete disorder of the  $V^{3+}$  and  $V^{4+}$  cations whereas the insulating state showed a high degree of ordering with the V3-V1-V1-V3 chain being formed by  $V^{4+}$  ions and the V4-V2-V2-V4 by  $V^{3+}$  ones. In addition to electron localization, most works point out that half of the  $V^{4+}$  and all  $V^{3+}$  cations are paired, forming short V-V bonds along their corresponding chains in the insulating state.

Several questions arise when looking at these results. i) The first is, what is the nature of V pairing in the insulating phase? The formation of spin singlets between  $V^{4+}$  cations ( $d^1$ ) is quite common but this is not exactly so between  $V^{3+}$  cations ( $d^2$ ). Hence, this was an open question for us. ii) What is the character and the mechanism of magnetic ordering in  $V_4O_7$  below  $T_N = 40$  K? If we accept the previous hypothesis, the paired  $V^{4+}$  ions (V1-V1) are in a singlet state and are inactive

magnetically. If  $V^{3+}$  pairs would also be singlet, then only 1/4 of all the  $V$ 's, the unpaired  $V^{4+}$  in V3 position, would be magnetic. But then it would be difficult to understand why such a “dilute” magnetic system, with magnetic ions with small spin  $S= 1/2$  and located far from each other, would give a reasonably high value of the Néel temperature of  $\sim 40$  K.

On an attempt to answer these questions, we have studied the electronic structure of  $V_4O_7$  analyzing the differences between the low-temperature (charge ordered, antiferromagnetically ordered and insulating) and the high-temperature (charge disordered, paramagnetic and metallic) phases.

Calculations show the strong CO in the low-temperature phase that, together with structural distortions, lead to a gap opening. The high-temperature structure is charge disordered, with all  $V$  atoms in a similar  $\sim d^{1.5}$  electronic configuration. All the in-chain magnetic couplings in the low-temperature phase are AFM, and the inter-chain couplings are very weak (and of different signs depending on the  $U$ -value). Magnetic coupling changes to FM in the high-temperature phase as a result of the change in electron distribution caused by charge disorder. The AFM couplings in the low-temperature phase are obtained, being very strong in the  $V^{4+}$ - $V^{4+}$  short bonds, one order of magnitude stronger than the short  $V^{3+}$ - $V^{3+}$  magnetic couplings (and two orders of magnitude stronger than in the  $V^{4+}$ - $V^{4+}$  long bonds). This suggests the formation of a spin-singlet between the “middle”  $V$ 's within the  $V^{4+}$  chains, leaving V3 atoms with unpaired spins. The couplings in the  $V^{3+}$  chains are more complicated, showing signs of slight moment reduction due to hybridizations.

The orbital order obtained in our electronic structure calculations ( $V^{4+}$ :  $d_{xy}$  vs.  $V^{3+}$ :  $d_{xz}, d_{yz}$ ) also helps to understand the different bond distance alternations that occur in the two different types of  $V$  chains: in the  $V^{4+}$  chains there is a strong metal-metal bond between the “middle” V1 ions forming spin singlets, and an (anti)ferroelectric-type displacement of the “edge”  $V^{4+}$  ions at the shear planes. On

the other hand, the  $V^{3+}$  chains, due to different orbital occupation, form two one-dimensional-like bands due to bridging with oxygens, that affects the type of coupling along these chains and leads, in particular, to a dimerization of  $V^{3+}$  chains, which, however, is not strong enough to make the short  $V^{3+}$ - $V^{3+}$  dimers spin singlets.

As a result, most probably both the unpaired “edge”  $V^{4+}$  and all  $V^{3+}$  ions contribute to magnetic ordering below  $T_N$ , the detailed type of which is yet unknown.

## C.2 Electronic structure of bulk CrN: A comparison between different exchange correlation potentials

CrN is a transition metal nitride that has attracted considerable attention due to its interesting physical properties. It shows a MPT as a function of temperature from an orthorhombic antiferromagnetic (AFM) phase to a cubic paramagnetic (PM) one at a Néel temperature  $T_N \sim 273$ - $286$  K. CrN also exhibits high thermal stability, corrosion resistance, and excellent mechanical properties that have recently been shown to be susceptible to improvements if somehow one can force the system to remain in the harder AFM configuration. All this combined with the ease of film deposition and promising thermoelectric properties make this compound a good source of different physical properties. In spite of its simple structure and the amount of work accumulated over the years, it is still a ground for contention among different pictures, both of its conduction and electronic properties.

The main focus of controversy has been the understanding of CrN electrical behavior. At least three different points of view can be found to describe the nature of the MPT: metal-metal, metal-semiconductor and semiconductor-semiconductor. We should point out that most of the experiments that find a metallic behavior in the low-temperature phase are mainly performed in thin films.

To shed light on the existing controversies about CrN, we have performed electronic structure calculations using a diverse set of exchange-correlation potentials: PBE, LDA+ $U$ , the semilocal functional developed by Tran and Blaha based on a modification of the Becke-Johnson potential, and hybrid functionals both in screened (YS-PBE0) and unscreened (PBE0) modes.

In any case, our calculations show that the onset of magnetism in CrN should be accompanied of a gap opening. We can conclude that the AFM phase is always insulating in agreement with experiments in stoichiometric bulk samples. The different metallic behavior found in various thin films most likely has to do with nanostructuring that could include vacancies, strain, surface effects, etc. In a system situated so close to the itinerant boundary, small changes can yield metallicity and even the suppression of the magnetic transition (which we have seen from our calculations it is strongly dependent on the structural details). The behavior obtained for the thermoelectric power confirms that stoichiometric CrN in the magnetic phase is semiconducting, but close to the transition from localized to itinerant behavior. The solution we found as ground state can describe accurately the transport properties of the system.

In addition, our results give further evidence that the TB-mBJLDA functional is very useful for treating the electronic structure of correlated semiconductors giving almost the same band gaps as obtained from LDA+ $U$  with  $U = 4$  eV (close to the one determined experimentally) for different magnetic configurations allowing a parameter-free description of the system. Hybrid functionals are also well capable of describing the electronic structure of CrN by tuning the amount of Hartree-Fock exact exchange. However, results and tunability are comparable with LDA+ $U$ , that allows an easier physical description of the tuning parameter  $U$ , and is computationally less demanding.



### C.3 Surface electric dipole formation in CrN (001) very thin films

Using the LDA+ $U$  method with the optimal  $U$  value obtained for bulk CrN ( $U = 4$  eV), we have studied the electronic and magnetic properties of free-standing CrN films of different thicknesses grown along the  $z$ -axis in order to elucidate the origin of the metallic behavior found experimentally in the low-temperature phase, to determine whether it can be intrinsic or not, and also what the effects of the material being so close to a metal-insulator transition are when it is nanostructured in the form of thin films. Our main goal was to analyze the changes in electronic structure with respect to the material as a bulk, determine the relaxed equilibrium structures and the appearance of new electronic states and its origin as a consequence of nanostructuring.

Like that, we could see that although in the bulk the onset of anti-ferromagnetic order always opens a gap, for thin films with increasing thickness the gap closes and conducting states appear. The appearance of metallic states is connected with a structural relaxation at the surface where Cr(N) atoms buckle inside(outside) forming an effective dipole moment. With CrN being a low-gap system, the electric dipoles at the surface caused by the Cr atoms displacing inwards shift the bands around the Fermi level significantly enough (around 1 eV) to drive the thin films towards metallicity. These conducting surface states become further stabilized by structural relaxations, that tend to favor a gap closure and hence a metallic solution for the system. Partial charges analysis confirms these conducting states live very close to the surface and do not contribute to the overall conductivity. The non-relaxed cases remain gapped because the atomic relaxations that lead to such a local electric polarization are suppressed. This suggests that local strains and other defects can drastically modify the conduction properties of CrN as it is observed experimentally, confirming our initial hypothesis.

## C.4 Electronic structure of CrN/MgO multilayers

To check what the effects of CrN grown on top of a MgO substrate are from first principles electronic structure calculations we decided to study the electronic and magnetic properties of CrN/MgO multilayers. From a theory standpoint it is the best scenario to analyze the effect of a drastic dimensionality reduction and also the evolution of the system with thickness without conducting surface states appearing, that complicate the picture and prevent the study of quantum confinement effects alone. With this goal in mind, we performed calculations within the LDA+ $U$  method again with the optimal  $U$  value obtained for bulk CrN ( $U = 4$  eV) in CrN/MgO multilayers, varying the thickness of the CrN block. The band gap increases as CrN is confined to the smallest thicknesses, as has been observed in other correlated  $3d$  electron systems. This leads to an increase in the calculated thermopower. The interface between the nitride and the band insulating oxide leads to a band shift that stabilizes the interfacial Cr- $d$  bands, as observed in the DOS and core-level energies. This would be the appropriate system to study the intrinsic non-metallic properties of CrN, that in the past has been observed to occur close to a metal-insulator transition: i) in the bulk non-stoichiometries always blur the picture, allowing for a wide range of interpretations of its electronic structure to appear in the literature, ii) in the case of thin films, surface states due to the surface polarity complicate the understanding of its electronic properties. None of that would be present in this multilayered system.

## C.5 $\text{Sr}_6\text{Co}_5\text{O}_{15}$ : non-one-dimensional behavior of a charge ordered structurally quasi-one-dimensional oxide

$\text{Sr}_6\text{Co}_5\text{O}_{15}$  is a member of the homologous series  $A_{n+2}B'B_n\text{O}_{3n+3}$  (A alkaline or alkaline earth cations, B' and B commonly corresponding to Co cations in a trigonal prismatic and octahedral position, respectively, and  $n \in [1, \infty)$ ). In particular, both the end members of the series ( $\text{Ca}_3\text{Co}_2\text{O}_6$  ( $n=1$ ) and  $\text{BaCoO}_3$  ( $n=\infty$ )) have focused much attention for the past years. However, there are fewer works on the magnetic or electronic structure properties for the compounds with  $2 \leq n \leq \infty$ .

This led us to analyze the electronic structure and special magnetic properties of the  $n=4$  member of the series. From our results, the material is a semiconducting antiferromagnet that shows some peculiar electronic structure properties that make it different from the other members of the series: i) Both the  $\text{Co}^{3+}$  atoms are non-magnetic and located in octahedra. ii) The in-chain couplings are not purely FM, AFM couplings (though weak) occur within the chains. iii) This, together with the existence of two non-magnetic Co atoms in the unit cell, reduce not only the in-chain but also the inter-chain magnetic couplings. iv) Due to ii) and iii) the magnetic properties of the material can no longer be understood as FM spin chains coupled AFM in-plane as occurs in other members of the series. v) The preferred orientation of the orbital angular momenta is non-collinear, in contrast to the strong Ising-type behavior found in  $\text{Ca}_3\text{Co}_2\text{O}_6$  and  $\text{BaCoO}_3$ . In addition, transport properties calculations support our understanding of its electronic structure and magnetic properties.

This anomalous behavior makes  $\text{Sr}_6\text{Co}_5\text{O}_{15}$  less quasi-one-dimensional than expected due to its structure and helps understand the intricate structure-property relations in strongly correlated electron systems.

## C.6 Enhanced thermoelectric response of $\text{La}_2\text{NiO}_{4+\delta}$ through hole doping and strain by *ab initio* calculations

Transition metal oxides, and particularly misfit layered cobaltates are promising as thermoelectric materials because of their chemical stability and possible usage in high-temperature devices. We considered that a possible candidate family that could present a similar thermoelectric response is a particular kind of layered nickelate: hole-doped  $\text{La}_2\text{NiO}_4$ . For this reason, we performed DFT and transport properties calculations in this material, first just through hole doping using a set of different exchange-correlation potentials and then adding strain, within the TB-mBJLDA potential which has proven very useful for treating this type of systems from a purely *ab initio* standpoint.

Our *ab initio* calculations for the compound indicate some promising features of hole-doped  $\text{La}_2\text{NiO}_4$  as a possible oxide thermoelectric compound. Our calculations show that a region with relatively large Seebeck coefficient exists in this compound at small doping levels, within the realistic AFM description. Hole doping will increase the conductivity, as the thin-film geometry does, which together with the reduction in thermal conductivity could leave room for an improvement of the thermoelectric figure of merit of this layered nickelate.

When applying strain, the recipe for improving the thermoelectric efficiency of  $\text{La}_2\text{NiO}_{4+\delta}$ , according to our calculations, would be the growth in thin films with oxygen excess on the order of  $\delta \sim 0.10$ , grown on top of a substrate that provides some tensile strain (grown on  $\text{SrTiO}_3$  or  $\text{MgAl}_2\text{O}_4$ , and studied at high temperatures, where the most plausible applications of this oxide and the larger figure of merit will occur. Very recently, experiments have been performed and confirmed our predictions. They show that indeed tensile strain leads to an enhancement

of the thermopower but not only that, this enhancement is independent of variations of the resistivity so it is possible to decouple the often inter-related transport coefficients by controlling the epitaxial growth.

## C.7 Conclusions

All in all, we have analyzed the structural, magnetic, electronic and thermoelectric properties of several transition metal compounds. Their study gives us a broad picture of how *ab initio* techniques can be applied to correlated electron systems, how one can design new ways to tune them computationally and what new properties can be predicted for this interesting class of materials. We can conclude that *ab initio* techniques correctly describe the physical properties of these systems and that many of the electronic properties can be manipulated giving rise to new functionalities. We have identified new computational schemes that work better in describing these systems and found the way to understand their electronic structure through the understanding of their thermopower.





## Bibliography

- [1] C. H. Ahn, J. M. Triscone, and J. Mannhart, *Nature* **424**, 1015 (2003).
- [2] E. Schroedinger, *Am. Physik* **79**, 361 (1926).
- [3] P. Hohenberg and W. Kohn, *Phys. Rev.* **136**, B864 (1964).
- [4] W. Kohn and L. J. Sham, *Phys. Rev.* **140**, A1133 (1965).
- [5] W. Kohn, *Electronic structure of matter-wave functions and density functionals* (Nobel Lecture, 1999).
- [6] T. Kimura, T. Goto, H. Shintani, K. Ishizaka, T. Arima, and Y. Tokura, *Nature* **426**, 55 (2002).
- [7] J. G. Bednorz and K. A. Muller, *Z. Phys. B* **64**, 189 (1986).
- [8] S. Jin, T. H. Tiefel, M. McCormack, R. A. Fastnacht, R. Ramesh, and L. Chen, *Science* **264**, 413 (1994).
- [9] G. J. Snyder and E. S. Toberer, *Nat. Mat.* **7**, 105 (2008).
- [10] J. B. Goodenough, vol. 98 (Springer, Berlin, 2001).

- 
- [11] M. Imada, A. Fujimori, and Y. Tokura, *Rev. Mod. Phys.* **70**, 1039 (1998).
- [12] I. Loa, P. Adler, A. Grzechnik, K. Syassen, U. Schwarz, M. Hanfland, G. K. Rozenberg, P. Gorodetsky, and M. P. Pasternak, *Phys. Rev. Lett.* **87**, 125501 (2001).
- [13] S. Blanco-Canosa, F. Rivadulla, V. Pardo, D. Baldomir, J. S. Zhou, M. García-Hernández, M. A. López-Quintela, J. Rivas, and J. B. Goodenough, *Phys. Rev. Lett.* **99**, 187201 (2007).
- [14] A. Kismaharadja, J. S. Brooks, A. Kiswandhi, K. Matsubayashi, R. Yamanaka, Y. Uwatoko, J. Whalen, T. Siegrist, and H. D. Zhou, *Phys. Rev. B* **106**, 056602 (2011).
- [15] F. J. Morin, *Phys. Rev. Lett.* **3**, 34 (1959).
- [16] J. B. Torrance, P. Lacorre, A. I. Nazzal, E. J. Ansaldo, and C. Niedermayer, *Phys. Rev. B* **45**, 8209 (1992).
- [17] D. H. Kim, D. W. Kim, B. S. Kang, T. W. Noh, D. R. Lee, K. B. Lee, and S. J. Lee, *Solid State Commun.* **114**, 473 (2000).
- [18] Y. Kobayashi, S. Taniguchi, M. Kasai, M. Sato, T. Nishioka, and M. Kontani, *J. Phys. Soc. Japan* **65**, 3978 (1996).
- [19] J. B. Goodenough, *Phys. Rev.* **100**, 564 (1955).
- [20] J. Liu, S. Okamoto, M. van Veenendaal, M. Kareev, B. Gray, P. Ryan, J. W. Freeland, and J. Chakhalian, *Phys. Rev. B* **83**, 161102 (2011).
- [21] J. B. Goodenough and F. Rivadulla, *Mod. Phys. Lett. B* **19**, 1057 (2006).
- [22] D. I. Khomskii and T. Mizokawa, *Phys. Rev. Lett.* **94**, 156402 (2005).



- [23] F. Rivadulla, M. B. noble López, C. X. Quintela, A. P. neiro, V. Pardo, D. Baldomir, M. A. López-Quintela, J. Rivas, C. A. Ramos, H. Salva, et al., *Nat. Mater.* **8**, 947 (2009).
- [24] J. Hubbard, *Proc. Roy. Soc. London Ser. A* **276**, 238 (1963).
- [25] J. Hubbard, *Proc. Roy. Soc. London Ser. A* **277**, 237 (1964).
- [26] J. Hubbard, *Proc. Roy. Soc. London Ser. A* **281**, 401 (1964).
- [27] A. Ohtomo and H. Y. Hwang, *Nature* **427**, 423 (2004).
- [28] A. Brinkman, M. Huijben, M. van Zalk, J. Huijben, U. Zeitler, J. C. Maan, W. G. van der Wiel, G. Rijnders, D. H. A. Blank, and H. Hilgenkamp, *Nat. Matter.* **6**, 493 (2007).
- [29] N. Reyren, S. Thiel, A. D. Caviglia, L. F. Kourkoutis, G. Hammerl, C. Richter, C. W. Schneider, T. Kopp, A.-S. Raetschi, D. Jaccard, et al., *Science* **317**, 1196 (2007).
- [30] A. F. Santander-Syro, O. Copie, T. Kondo, F. Fortuna, S. Pailhes, R. Weht, X. G. Qiu, F. Bertran, A. Nicolaou, A. Taleb-Ibrahimi, et al., *Nature* **469**, 189 (2011).
- [31] R. Pentcheva and W. E. Pickett, *Phys. Rev. B* **78**, 205106 (2008).
- [32] C. He, T. D. Sanders, M. T. Gray, F. J. Wong, V. V. Mehta, and Y. Suzuki, *Phys. Rev. B* **86**, 081401(R) (2012).
- [33] U. Lüders, W. C. Sheets, A. David, W. Prellier, and R. Fresard, *Phys. Rev. B* **80**, 241102(R) (2009).
- [34] P. Boullay, A. David, W. C. Sheets, U. Lüders, W. Prellier, H. Tan, J. Verbeeck, G. Van Tendeloo, C. Gatel, G. Vincze, et al., *Phys. Rev. B* **83**, 125403 (2011).
- [35] D. Fuchs, C. Pinta, T. Schwarz, P. Schweiss, P. Nagel, S. Schuppler, R. Schneider, M. Merz, G. Roth, and H. v. Löhneysen, *Phys. Rev. B* **75**, 144402 (2007).

- [36] H. Hsu, P. Blaha, and R. M. Wentzcovitch, *Phys. Rev. B* **85**, 140404 (2012).
- [37] F. Rivadulla, Z. Bi, E. Bauer, B. Rivas-Murias, J. M. Vila-Fungueiriño, and Q. Jia, *Chem. Mater.* **25**, 55 (2013).
- [38] V. Pardo and W. E. Pickett, *Phys. Rev. Lett.* **102**, 166803 (2009).
- [39] V. Pardo and W. E. Pickett, *Phys. Rev. B* **81**, 035111 (2010).
- [40] V. Pardo and W. E. Pickett, *Phys. Rev. B* **81**, 245117 (2010).
- [41] K. Yoshimatsu, T. Okabe, H. Kumigashira, S. Okamoto, S. Aizaki, A. Fujimori, and M. Oshima, *Phys. Rev. Lett.* **104**, 147601 (2010).
- [42] I. Terasaki, Y. Sasago, and K. Uchinokura, *Phys. Rev. B* **56**, R12685 (1997).
- [43] D. J. Singh and D. Kasinathan, *Journal of Electronic Materials* **36**, 736 (2007).
- [44] G. D. Mahan and J. O. Sofo, *Proceedings of the National Academy of Sciences* **93**, 7436 (1996).
- [45] J. Zhou, R. Yang, G. Chen, and M. S. Dresselhaus, *Phys. Rev. Lett.* **107**, 226601 (2011).
- [46] M. Dresselhaus, G. Chen, M. Y. Tang, R. G. Yang, H. Lee, D. Wang, Z. F. Ren, J. P. Fleurial, and P. Gogna, *Advanced Materials* **19**, 1043 (2007).
- [47] L. D. Hicks and M. Dresselhaus, *Phys. Rev. B* **47**, 12727 (1993).
- [48] L. H. Thomas, *Proc. Cambridge Phil. Soc.* **23**, 542 (1927).
- [49] V. Fock, *Z. Physik* **61**, 126 (1930).
- [50] J. C. Slater, *Phys. Rev.* **35**, 210 (1930).

- [51] R. G. Parr and W. Yang, *Density-functional theory of atoms and molecules* (Oxford University Press, New York, 1989).
- [52] R. O. Jones and O. Gunnarsson, *Rev. Mod. Phys.* **61**, 689 (1989).
- [53] J. P. Perdew, K. Burke, and M. Ernzerhof, *Phys. Rev. Lett.* **77**, 3865 (1996).
- [54] J. P. Perdew and Y. Wang, *Phys. Rev. B* **45**, 13244 (1992).
- [55] Z. Wu and R. E. Cohen, *Phys. Rev. B* **73**, 235116 (2006).
- [56] F. Tran and P. Blaha, *Phys. Rev. Lett.* **102**, 226401 (2009).
- [57] D. J. Singh, *Phys. Rev. B* **82**, 205102 (2010).
- [58] D. Koller, F. Tran, and P. Blaha, *Phys. Rev. B* **83**, 195134 (2011).
- [59] V. Anisimov, F. Aryasetiawan, and A. Lichtenstein, *J. Phys. Condens. Matter* **9**, 767 (1997).
- [60] A. Seidl, A. Görling, P. Vogl, J. A. Majewski, and M. Levy, *Phys. Rev. B* **53**, 3764 (1996).
- [61] A. D. Becke and E. R. Johnson, *J. Chem. Phys.* **124**, 221101 (2006).
- [62] J. C. Slater, *Phys. Rev.* **51**, 846 (1937).
- [63] O. K. Andersen, *Phys. Rev. B* **12**, 3060 (1975).
- [64] D. D. Koelling and G. O. Arbman, *J. Phys. F: Met. Phys.* **5**, 2041 (1975).
- [65] E. Sjöstedt, L. Nördstrom, and D. J. Singh, *Solid State Commun.* **114**, 15 (2000).
- [66] G. K. H. Madsen, P. Blaha, K. Schwarz, E. Sjöstedt, and L. Nördstrom, *Phys. Rev. B* **64**, 195134 (2001).
- [67] K. Schwarz and P. Blaha, *Comp. Mat. Sci.* **28**, 259 (2003).

- [68] P. Blaha, K. Schwarz, G. K. H. Madsen, D. Kvasnicka, and J. Luitz, *WIEN2k, An Augmented Plane Wave Plus Local Orbitals Program for Calculating Crystal Properties*. ISBN 3-9501031-1-2, Vienna University of Technology, Austria (2001).
- [69] J. P. Perdew, S. Kurth, J. Zupan, and P. Blaha, *Phys. Rev. Lett.* **82**, 2544 (1999).
- [70] J. Tao, J. P. Perdew, V. Starovenov, and G. Scuseria, *Phys. Rev. Lett.* **91**, 146401 (2003).
- [71] F. Tran and P. Blaha, *Phys. Rev. B* **83**, 235118 (2011).
- [72] A. Lichtenstein, V. Anisimov, and J. Zaanen, *Phys. Rev. B* **52**, R5467 (1995).
- [73] E. R. Ylvisaker, W. E. Pickett, and K. Koepernik, *Phys. Rev. B* **79**, 035103 (2009).
- [74] T. J. Scheidemantel, C. Ambrosch-Draxl, T. Thonhauser, J. V. Badding, and J. O. Sofo, *Phys. Rev. B* **68**, 125210 (2003).
- [75] G. K. H. Madsen and D. J. Singh, *Comp. Phys. Commun.* **175**, 67 (2006).
- [76] D. B. McWhan, M. Marezio, J. P. Remeika, and P. D. Dernier, *Phys. Rev. B* **10**, 490 (1974).
- [77] J. L. Hodeau and M. Marezio, *J. Solid State Chem.* **23**, 253 (1978).
- [78] P. Dernier, *J. Phys. Chem. Solids* **31**, 2569 (1970).
- [79] J. B. Goodenough, *J. Solid State Chem.* **3**, 490 (1971).
- [80] R. M. Wentzcovitch, W. W. Chulz, and P. B. Allen, *Phys. Rev. Lett.* **72**, 3389 (1994).
- [81] M. S. Laad, L. Craco, and E. Mueller-Hartmann, *Europhys. Lett.* **69**, 984 (2005).

- [82] S. Biermann, A. Poteryaev, A. I. Lichtenstein, and A. Georges, *Phys. Rev. Lett.* **94**, 026404 (2005).
- [83] S. Kachi, *A.I.P. Conf. Proc.* **10**, 714 (1973).
- [84] M. Marezio, D. B. McWhan, P. D. Dernier, and J. P. Remeika, *Phys. Rev. Lett.* **28**, 1390 (1972).
- [85] A. C. Gossard, J. P. Remeika, T. M. Rice, H. Yasuoka, K. Kosuge, and S. Kachi, *Phys. Rev. B* **9**, 1230 (1974).
- [86] Y. Ueda, Y. Kitaoka, H. Yasuoka, K. Kosuge, and S. Kachi, *J. Phys. Soc. Jpn.* **47**, 333 (1979).
- [87] A. Heidemann, K. Kosuge, and S. Kachi, *Phys. Stat. Sol. (a)* **35**, 481 (1976).
- [88] M. Marezio, D. B. McWhan, J. P. Remeika, and P. D. Dernier, *Phys. Rev. B* **5**, 2541 (1972).
- [89] J. P. Pouget, H. Lanouis, T. M. Rice, P. Dernier, A. Gossard, G. Villeneuve, and P. Hagenmuller, *Phys. Rev. B* **10**, 1801 (1974).
- [90] J. P. Pouget, H. Lanouis, J. P. D'Haenens, P. Merenda, and T. M. Rice, *Phys. Rev. Lett.* **35**, 873 (1975).
- [91] M. W. Haverkort, Z. Hu, A. Tanaka, W. Reichelt, S. V. Streltsov, M. A. Korotin, V. I. Anisimov, H. H. Hsieh, H. J. Lin, C. T. Chen, et al., *Phys. Rev. Lett.* **95**, 196404 (2005).
- [92] V. Pardo, S. Blanco-Canosa, F. Rivadulla, D. I. Khomskii, D. Baldomir, H. Wu, and J. Rivas, *Phys. Rev. Lett.* **101**, 256403 (2008).
- [93] C. Kuntscher, K. Rabia, M. K. Forthaus, M. M. Abd-Elmeguid, F. Rivadulla, Y. Kato, and C. D. Batista, *Phys. Rev. B* **86**, 020405 (2012).
- [94] A. S. Botana, V. Pardo, D. Baldomir, A. V. Ushakov, and D. I. Khomskii, *Phys. Rev. B* **84**, 115138 (2011).

- [95] A. Kokalj, *J. Mol. Graphics Modell.* **17**, 176 (1999).
- [96] H. Wu, C. F. Chang, O. Schumann, Z. Hu, J. C. Cezar, T. Burnus, N. Hollmann, N. B. Brookes, A. Tanaka, M. Braden, et al., *Phys. Rev. B* **84**, 155126 (2011).
- [97] V. Pardo and W. E. Pickett, *Phys. Rev. B* **81**, 035111 (2010).
- [98] A. C. Komarek, M. Isobe, J. Hemberger, D. Meier, T. Lorenz, D. Trots, A. Cervellino, M. T. Fernández-Díaz, Y. Ueda, and M. Braden, *Phys. Rev. Lett* **107**, 027201 (2011).
- [99] R. Niewa and F. J. DiSalvo, *Chem. Mater.* **10**, 2733 (1998).
- [100] B. R. Zhao, L. Chen, H. L. Luo, M. D. Jack, and D. P. Mullin, *Phys. Rev. B* **29**, 6198 (1984).
- [101] S. P. Chockalingam, M. Chand, A. Kamlapure, J. Jesudasan, A. Mishra, V. Tripathi, and P. Raychaudhuri, *Phys. Rev. B* **79**, 094509 (2009).
- [102] A. Lascialfari, A. Rigamonti, E. Bernardi, M. Corti, A. Gauzzi, and J. C. Villegier, *Phys. Rev. B* **80**, 104505 (2009).
- [103] T. I. Baturina, A. Y. Mironov, V. M. Vinokur, M. R. Baklanov, and C. Strunk, *Phys. Rev. Lett.* **99**, 257003 (2007).
- [104] L. M. Corliss, N. Elliott, and J. M. Hastings, *Phys. Rev.* **117**, 929 (1960).
- [105] A. Filippetti, W. E. Pickett, and B. M. Klein, *Phys. Rev. B* **59**, 7043 (1999).
- [106] A. Filippetti and N. A. Hill, *Phys. Rev. Lett.* **85**, 5166 (2000).
- [107] D. Gall, C.-S. Shin, R. T. Haasch, I. Petrov, and J. E. Greene, *J. Appl. Phys.* **91**, 5882 (2002).
- [108] K. Inumaru, K. Koyama, N. Imo-oka, and S. Yamanaka, *Phys. Rev. B* **75**, 054416 (2007).

- [109] X. Y. Zhang, J. S. Chawla, R. P. Deng, and D. Gall, *Phys. Rev. B* **84**, 073101 (2011).
- [110] C. X. Quintela, F. Rivadulla, and J. Rivas, *Appl. Phys. Lett.* **94**, 152103 (2009).
- [111] C. X. Quintela, F. Rivadulla, and J. Rivas, *Phys. Rev. B* **82**, 245201 (2010).
- [112] P. A. Anderson, R. J. Kinsey, S. M. Durbin, A. Markwitz, V. J. Kennedy, A. Asadov, W. Gao, and R. J. Reeves, *J. Appl. Phys.* **98**, 043903 (2005).
- [113] P. A. Bhoje, A. Chainani, M. Taguchi, T. Takeuchi, R. Eguchi, M. Matsunami, K. Ishizaka, Y. Takata, M. Oura, Y. Senba, et al., *Phys. Rev. Lett.* **104**, 236404 (2010).
- [114] C. Constantin, M. B. Haider, D. Ingram, and A. R. Smith, *Appl. Phys. Lett.* **85**, 6371 (2004).
- [115] D. Gall, C.-S. Shin, T. Spila, M. Odén, M. J. H. Senna, J. E. Greene, and I. Petrov, *J. Appl. Phys.* **91**, 3589 (2002).
- [116] X. Y. Zhang, J. S. Chawla, B. M. Howe, and D. Gall, *Phys. Rev. B* **83**, 165205 (2011).
- [117] Y. Tsuchiya, K. Kosuge, Y. Ikeda, T. Shigematsu, S. Yamaguchi, and N. Nakayama, *Mater. Trans., JIM* **37**, 121 (1996).
- [118] J. D. Browne, P. R. Liddell, R. Street, and T. Mills, *Phys. Status Solidi A* **1**, 715 (1970).
- [119] P. S. Herle, M. S. Hedge, N. Y. Vasathacharya, S. Philip, M. V. R. Rao, and T. Sripathi, *J. Solid State Chem.* **134**, 120 (1997).
- [120] X. Y. Zhang and D. Gall, *Phys. Rev. B* **82**, 045116 (2010).
- [121] X. F. Duan, W. B. Mi, Z. B. Guo, and H. L. Bai, *J. Appl. Phys.* **113**, 023701 (2013).

- [122] A. Herwadkar and W. R. L. Lambrecht, *Phys. Rev. B* **79**, 035125 (2009).
- [123] A. S. Botana, F. Tran, V. Pardo, D. Baldomir, and P. Blaha, *Phys. Rev. B* **85**, 235118 (2012).
- [124] A. D. Becke, *J. Chem. Phys.* **98**, 1372 (1993).
- [125] J. Muscat, A. Wander, and N. M. Harrison, *Chem. Phys. Lett.* **342**, 397 (2001).
- [126] I. de P. R. Moreira, F. Illas, and R. L. Martin, *Phys. Rev. B* **65**, 155102 (2002).
- [127] K. N. Kudin, G. E. Scuseria, and R. L. Martin, *Phys. Rev. Lett.* **89**, 266402 (2002).
- [128] M. Ernzerhof and G. E. Scuseria, *J. Chem. Phys.* **110**, 5029 (1999).
- [129] C. Adamo and V. Barone, *J. Chem. Phys.* **110**, 6158 (1999).
- [130] D. M. Bylander and L. Kleinman, *Phys. Rev. B* **41**, 7868 (1990).
- [131] J. Heyd, G. E. Scuseria, and M. Ernzerhof, *J. Chem. Phys.* **118**, 8207 (2003), **124**, 219906 (2006).
- [132] J. Heyd and G. E. Scuseria, *J. Chem. Phys.* **120**, 7274 (2004).
- [133] R. M. Ibberson and R. Cywinski, *Physica B* **180-181**, 329 (1992).
- [134] J. Zaanen, G. A. Sawatzky, and J. W. Allen, *Phys. Rev. Lett.* **55**, 418 (1985).
- [135] J. Sugiyama, H. Nozaki, J. H. Brewer, E. J. Ansaldo, T. Takami, H. Ikuta, and U. Mizutani, *Phys. Rev. B* **72**, 064418 (2005).
- [136] K. Boulahya, M. Parras, and J. M. González-Calbet, *J. Solid State Chem.* **142**, 419 (1999).



- [137] K. Boulahya, M. Parras, J. M. González-Calbet, and A. Vegas, *J. Solid State Chem.* **151**, 77 (2000).
- [138] A. Maignan, C. Michel, A. C. Masset, B. Raveau, and C. Martin, *Eur. Phys. J. B* **15**, 657 (2000).
- [139] H. Fjellvåg, E. Gulbrandsen, S. Aasland, A. Olsen, and B. C. Hauback, *J. Solid State Chem.* **124**, 190 (1996).
- [140] S. Aasland, H. Fjellvåg, and B. Hauback, *Solid State Commun.* **101**, 187 (1997).
- [141] H. Kageyama, K. Yoshimura, K. Kosuge, M. Azuma, M. Takano, H. Mitamura, and T. Goto, *J. Phys. Soc. Jpn.* **66**, 3996 (1997).
- [142] B. Martínez, V. Laukhin, M. Hernando, J. Fontcuberta, M. Parras, and J. M. González-Calbet, *Phys. Rev. B* **64**, 012417 (2001).
- [143] H. Wu, T. Burnus, Z. Hu, C. Martin, A. Maignan, J. C. Cezar, A. Tanaka, N. B. Brookes, D. I. Khomskii, and L. H. Tjeng, *Phys. Rev. Lett.* **102**, 026404 (2009).
- [144] J.-G. Cheng, J.-S. Zhou, and J. B. Goodenough, *Phys. Rev. B.* **79**, 184414 (2009).
- [145] Y. Kamiya and C. D. Batista, *Phys. Rev. Lett.* **109**, 067204 (2012).
- [146] H. Taguchi, Y. Takeda, F. Kanamaru, M. Shimada, and M. Koizumi, *Acta Crystallogr.* **B33**, 1298 (1977).
- [147] K. Yamaura, H. W. Zandbergen, K. Abe, and R. J. Cava, *J. Solid State Chem.* **146**, 96 (1999).
- [148] V. Pardo, M. Iglesias, D. Baldomir, J. Castro, and J. E. Arias, *Solid State Commun.* **128**, 101 (2003).
- [149] V. Pardo, P. Blaha, M. Iglesias, K. Schwarz, D. Baldomir, and J. E. Arias, *Phys. Rev. B.* **70**, 144422 (2004).

- [150] V. Pardo, J. Rivas, and D. Baldomir, *Appl. Phys. Lett.* **86**, 202507 (2005).
- [151] P. M. Botta, V. Pardo, D. Baldomir, C. de la Calle, J. A. Alonso, and J. Rivas, *Phys. Rev. B.* **74**, 214415 (2006).
- [152] V. Pardo, P. Blaha, K. Schwarz, and D. Baldomir, *Physica B* **378**, 556 (2006).
- [153] V. Pardo, P. Blaha, R. Laskowski, D. Baldomir, J. Castro, K. Schwarz, and J. E. Arias, *Phys. Rev. B* **76**, 165120 (2007).
- [154] H. Nozaki, M. Janoschek, B. Roessli, J. Sugiyama, L. Keller, J. H. Brewer, E. J. Ansaldo, G. D. Morris, T. Takami, and H. Ikuta, *Phys. Rev. B* **76**, 014402 (2007).
- [155] J. Sugiyama, H. Nozaki, Y. Ikedo, K. Mukai, D. Andreica, A. Amato, J. H. Brewer, E. J. Ansaldo, G. D. Morris, T. Takami, et al., *Phys. Rev. Lett.* **96**, 197206 (2006).
- [156] J. Sun, G. Li, Z. Li, L. You, and J. Lin, *Inorg. Chem.* **45**, 8394 (2006).
- [157] M.-H. Whangbo, H.-J. Koo, K.-S. Lee, O. Gourdon, M. Evain, S. Jobic, and R. Brec, *J. Solid State Chem.* **160**, 239 (2001).
- [158] R. Hoffmann, *J. Chem. Phys.* **39**, 1397 (1963).
- [159] K. Iwasaki, M. Shimada, H. Yamane, J. Takahashi, S. Kubota, T. Nagasaki, Y. Arita, J. Yuhara, Y. Nishi, and T. Matsui, *J. Alloy. Compd.* **377**, 272 (2004).
- [160] T. Takami, M. Horibe, M. Itoh, and J. Cheng, *Phys. Rev. B* **82**, 085110 (2010).
- [161] T. Takami, H. Ikuta, and U. Mizutani, *Jpn. J. Appl. Phys* **43**, 8208 (2004).

- [162] A. S. Botana, P. M. Botta, C. de la Calle, A. Pieiro, V. Pardo, D. Baldomir, and J. A. Alonso, *Phys. Rev. B* **83**, 184420 (2011).
- [163] A. S. Botana, P. M. Botta, C. de la Calle, A. P. neiro, V. Pardo, D. Baldomir, J. A. Alonso, and J. Rivas, *J. Appl. Phys.* **109**, 07E114 (2011).
- [164] D. J. Singh, *Planewaves, pseudopotentials and the LAPW method* (Kluwer Academic Publishers, 1994).
- [165] C. de la Calle, J. A. Alonso, and M. T. Fernández-Díaz, *Z. Naturforsch.* **63**, 647 (2008).
- [166] W. T. A. Harrison, S. L. Hegwood, and A. J. Jacobson, *J. Chem. Soc. Chem. Comm.* p. 1953 (1995).
- [167] J. B. Goodenough, *Magnetism and the chemical bond* (Interscience publishers, 1963).
- [168] D. Phelan, D. Louca, K. Kamazawa<sup>1</sup>, S.-H. Lee, S. N. Ancona, S. Rosenkranz, Y. Motome, M. F. Hundley, J. F. Mitchell, and Y. Moritomo, *Phys. Rev. Lett.* **97**, 235501 (2006).
- [169] J. Wu and C. Leighton, *Phys. Rev. B* **67**, 174408 (2003).
- [170] Q. Zhao, J. Darriet, M. H. Whangbo, L. Ye, C. Stackhouse, and H. C. zur Loye, *JACS* **133**, 20981 (2011).
- [171] H. N. Li, Z. Y. Sun, Z. C. Xia, J. W. Huang, L. X. Xiao, L. P. Peng, Y. Y. Wu, G. H. Du, Z. W. Ouyang, L. Li, et al., *Phys. Status Solidi B* **249**, 1072 (2012).
- [172] A. Abragam and B. Bleaney, *Electron paramagnetic resonance of transition ions* (Clarendon Press, Oxford, 1970).
- [173] K. W. H. Stevens, *Proc. R. Soc. Lond. A* **219**, 542 (1953).
- [174] J. B. Goodenough, *Phys. Rev.* **171**, 466 (1968).
- [175] C. Lacroix, *J. Phys. C Solid State* **13**, 5125 (1980).

- [176] W. E. Pickett and H. Eschrig, *J. Phys.: Condens. Matter* **19**, 315203 (2007).
- [177] H. J. Xiang and D. J. Singh, *Phys. Rev. B* **76**, 195111 (2007).
- [178] A. C. Masset, C. Michel, A. Maignan, M. Hervieu, O. Toulemonde, F. Studer, B. Raveau, and J. Hejtmanek, *Phys. Rev. B* **62**, 166 (2000).
- [179] T. Yamamoto, K. Uchinokura, and I. Tsukada, *Phys. Rev. B* **65**, 184434 (2002).
- [180] S. Landron and M. B. Lepetit, *Phys. Rev. B* **74**, 184507 (2006).
- [181] J. B. Goodenough and S. Ramasesha, *Mater. Res. Bull.* **17**, 383 (1982).
- [182] J. Rodríguez-Carvajal, M. T. Fernández-Díaz, and J. L. Martínez, *J. Phys.: Condens. Matter* **3**, 3215 (1991).
- [183] P. Ganguly and C. N. R. Rao, *Mater. Res. Bull.* **8**, 405 (1973).
- [184] V. V. Poltavets, K. A. Loshkin, T. Egami, and M. Greenblatt, *Mat. Res. Bull.* **41**, 955 (2006).
- [185] V. V. Poltavets, K. A. Loshkin, M. Croft, T. K. Mandal, T. Egami, and M. Greenblatt, *Inorg. Chem.* **46**, 10887 (2007).
- [186] V. V. Poltavets, K. A. Loshkin, A. H. Nevidomskyy, M. Croft, T. A. Tyson, J. Hadermann, G. V. Tendeloo, T. Egami, G. Kotliar, N. ApRoberts-Warren, et al., *Phys. Rev. Lett.* **104**, 206403 (2010).
- [187] V. V. Poltavets, M. Greenblatt, G. H. Fecher, and C. Felser, *Phys. Rev. Lett.* **102**, 046405 (2009).
- [188] N. ApRoberts-Warren, A. P. Dioguardi, V. V. Poltavets, M. Greenblatt, P. Klavins, and N. J. Curro, *Phys. Rev. B* **83**, 014402 (2011).

- [189] V. Pardo and W. E. Pickett, *Phys. Rev. Lett.* **105**, 266402 (2010).
- [190] J. G. Cheng, , J. S. Zhou, J. B. Goodenough, H. D. Zhou, K. Matsubayashi, Y. Uwatoko, P. P. Kong, C. Q. Yin, W. G. Yang, et al., *Phys. Rev. Lett.* **108**, 236403 (2012).
- [191] A. Demourgues, P. Dordor, J. P. Doumerc, J. C. Grenier, E. Marquestaut, M. Pouchard, A. Villesuzanne, and A. Wattiaux, *J. Solid State Chem.* **124**, 199 (1996).
- [192] V. V. Vashook, S. P. Tolochko, I. I. Yushkevich, L. V. Makhnach, I. F. Kononyuk, H. Altenburg, J. Hauck, and H. Ullmann, *Solid State Ionics* **110**, 245 (1998).
- [193] M. Burriel, J. Santiso, M. D. Rossell, G. van Tenderloo, A. Figueras, and G. García, *J. Phys. Chem. C* **41**, 955 (2008).
- [194] C. G. S. Pillai and A. M. George, *Int. J.. Thermophysics* **7**, 1091 (1986).
- [195] W. Xie, X. Tang, Q. Zhang, and T. M. Tritt, *Appl. Phys. Lett.* **94**, 102111 (2009).
- [196] V. Pardo, A. S. Botana, and D. Baldomir, *Phys. Rev. B* **86**, 165114 (2012).
- [197] J. Fontcuberta, G. Longworth, and J. B. Goodenough, *Phys. Rev. B* **30**, 6320 (1984).
- [198] P. Gopalan, M. W. McElfresh, Z. Kakol, J. Spalek, and J. M. Honig, *Phys. Rev. B* **45**, 249 (1992).
- [199] W. E. Pickett and D. J. Singh, *J. Magn. Magn. Mater.* **172**, 237 (1997).
- [200] J. M. Bassat, P. Odier, and J. P. Loup, *J. Solid State Chem.* **110**, 124 (1994).
- [201] D. J. Singh, *Phys. Rev. B* **76**, 195111 (2007).

- [202] J. Rodríguez-Carvajal, J. L. Martínez, J. Pannetier, and R. Saez-Puche, *Phys. Rev. B* **38**, 7148 (2010).
- [203] G. H. Lander, P. J. Brown, J. Spalek, and J. M. Honig, *Phys. Rev. B* **40**, 4463 (2010).
- [204] N. Zhou, G. Chen, H. J. Zhang, and C. Zhou, *Phys. B* **404**, 4150 (2009).
- [205] T. Strangfeld, K. Westerholt, and H. Bach, *Phys. C* **183**, 1 (1991).
- [206] S. Nishiyama, D. Sakaguchi, and T. Hattori, *Solid State Commun.* **94**, 279 (1995).
- [207] D. I. Khomskii and G. A. Sawatzky, *Solid State Commun.* **102**, 87 (1997).
- [208] X. Luo, M. B. Sullivan, and S. Y. Quek, *Phys. Rev. B* **86**, 184111 (2012).
- [209] V. Pardo, A. S. Botana, and D. Baldomir, *Phys. Rev. B* **87**, 125148 (2013).
- [210] P. L. Bach, V. Leboran, A. S. Botana, V. Pardo, D. Baldomir, and F. Rivadulla, *arxiv/1211.1615* (2012).
- [211] C. Yu, M. L. Scullin, M. Huijben, R. Ramesh, and A. Majumdar, *Appl. Phys. Lett.* **92**, 191911 (2008).
- [212] F. Rivadulla, private communication (2012).
- [213] A. S. Botana, V. Pardo, D. Baldomir, and P. Blaha, *Phys. Rev. B* **87**, 075114 (2013).
- [214] C. Martínez-Boubeta, A. S. Botana, V. Pardo, D. Baldomir, A. Antony, J. Bertomeu, J. M. Rebled, L. López-Conesa, S. Estradé, and F. Peiró, *Phys. Rev. B* **86**, 041407 (2012).